A SOLID STATE CONTROLLER FOR INDUCTION LOADS

by

George Havas

Submitted in Partial Fulfillment of the Requirements

for the Degree of

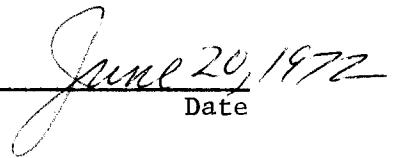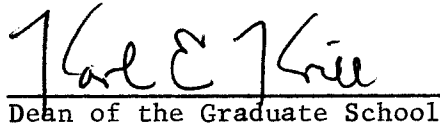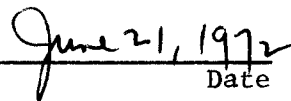Master of Science in Engineering

in the

Electrical Engineering

Program

_____   _____
Adviser   Date

_____   _____
Dean of the Graduate School   Date

YOUNGSTOWN STATE UNIVERSITY

August, 1972

ABSTRACT

A SOLID STATE CONTROLLER FOR INDUCTION LOADS

George Havas

Master of Science in Engineering

Youngstown State University, 1972

This thesis presents the results of an investigation concerning a thyristor controller with an induction heating load. Approximate and exact methods of analysis are utilized to predict system behavior. Unstable regions and an interesting jump phenomenon are predicted and experimentally verified. Extensive use has been made of a digital computer in predicting system performance.

ACKNOWLEDGEMENTS

TABLE OF CONTENTS

LIST OF FIGURES

CHAPTER   I

INTRODUCTION

The phenomenal development in the past few years of the four-layer semiconductor device, the thyristor, more commonly known as an SCR (silicon-controlled rectifier), opened a brand-new dimension in efficient and economical switching and controlling of large blocks of electrical power. SCR's have been used for controlling rotating equipment, as switching devices in frequency converters and in many other industrial and commercial applications.

In this thesis, the use of SCR's in switching and controlling power supplied to large induction heating or melting loads is investigated.

The utilization of SCR's has the following inherent advantages over conventional electromechanical or magnetic means of power control:

1. Higher Efficiency.

2. No moving parts.

3. No component deterioration.

4. Small physical size.

5. Transient-free starting.

6. Half-cycle fault protection.

7. Extremely fast response time.

However, the use of SCR's requires a deeper and better understanding of the complete system so that its performance under various load conditions can be predicted. The prediction of system performance is

not straight-forward due to the non-sinusoidal nature of the SCR
currents during the controlled mode of operation.

In the following chapters, the definition of basic terms,
a method of approximate analysis, the derivation of equations necessary
for exact analysis, digital simulation of the system and the comparison
of predicted performance versus experimental results is given.

In choosing the method of analysis for the digital simulations,
the following factors were of primary concern:

1. Accuracy of calculations.

2. Limited computer working core capacity (8K).

3. Limited computer time available.

In other words, the highest degree of accuracy was desired
with short computational time using a computer (IBM 1130) with
limited working core capacity.

An attempt has been made throughout this study to consider
cases of practical importance and to link the theoretical results
meaningfully to practical considerations.

CHAPTER II

DEFINITION OF TERMS

This chapter introduces the basic controller configuration,
its control scheme and operation and gives a definition of the basic
terms used throughout the following chapters, as well as a short dis-
cussion of the general nature and range of the load.

Basic Controller
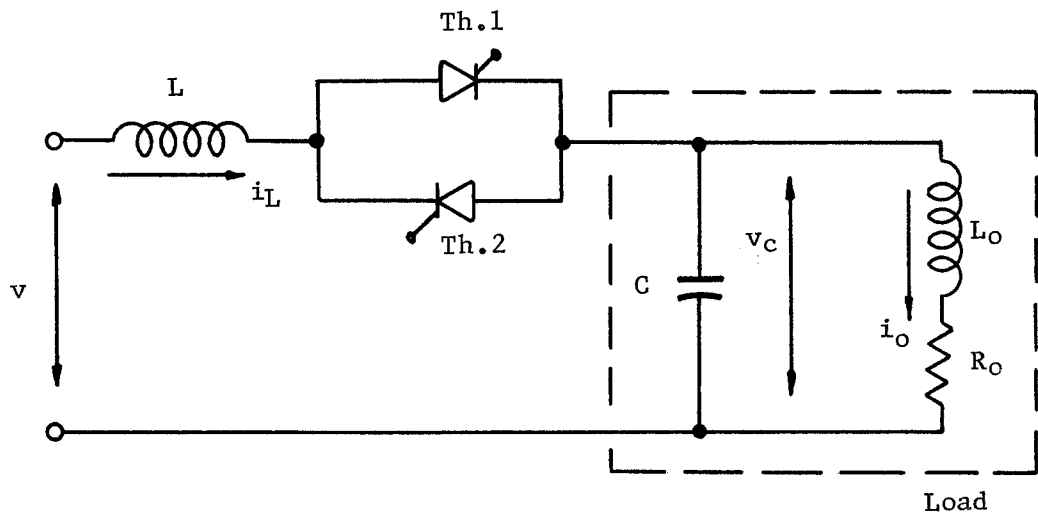
Fig.1   Basic controller schematic

Fig.1 is a schematic diagram of the controller. It consists of
a series inductance L, antiparallel connected thyristor switches Th.1,
Th.2, and a parallel-tuned tank circuit which is a simplified lumped
parameter representation of an induction load with its power factor
correcting capacitances.

Control Scheme

Stepless, continuous control of the power delivered to the load can be obtained by the use of a symmetrical phase control.
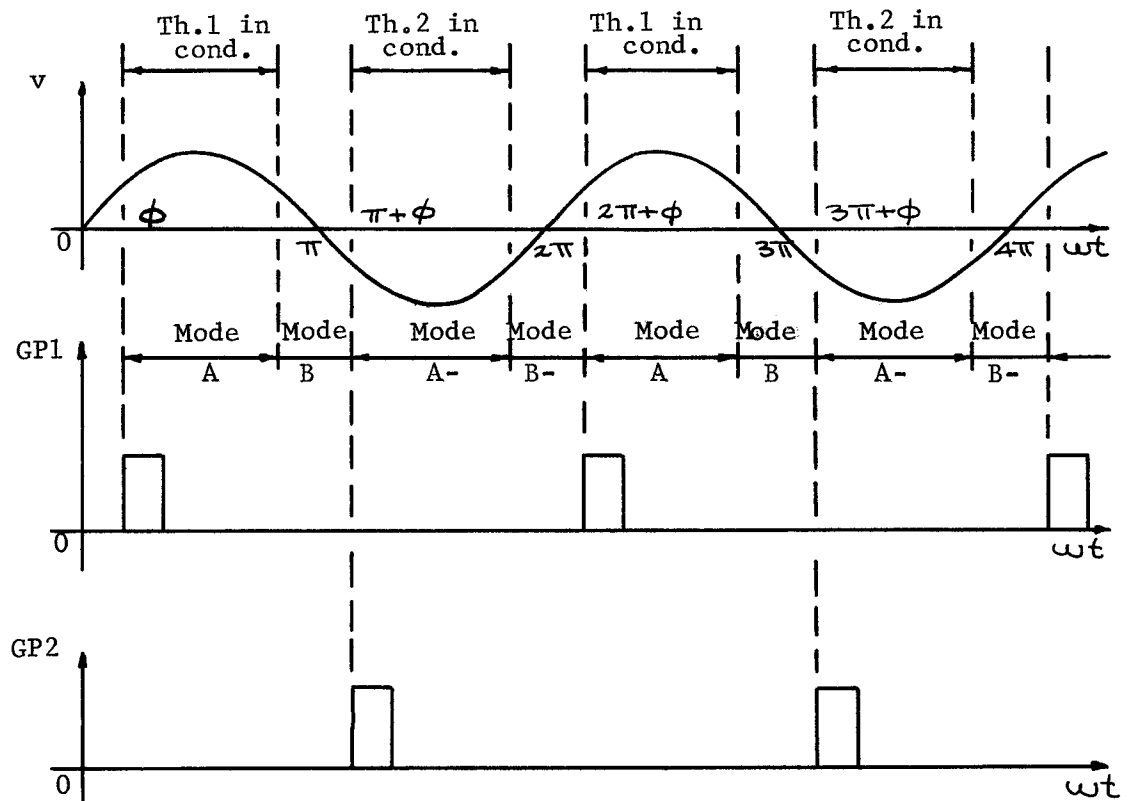
Fig. 2   Modes of operation and symmetrical phase control

Fig.2 illustrates the principle of symmetrical phase control. The input sinusoid v represents the time reference source. Gating pulses GP1 and GP2 are derived and controlled in such a manner that for any integral cycle they have a fixed interval between the zero

crossing of the reference supply and the start of the gate pulses. The interval between the start of each gate pulse and the previous zero crossing of the reference supply is defined as the firing angle ϕ . Symmetrical control of the load voltage, current or power is achieved by continuously varying the firing angle on an integral cycle basis. The symmetrical operation of the controller is extremely important in eliminating direct current and even harmonics from the supply lines.

<div align="center">

Basic Operation
</div>

The steady state operation of the controller can be described as a repetition of two transient modes. Fig.2 illustrates these modes.

Let us assume that Th.1 is connected so that it conducts current during the positive half cycle. Mode A starts when Th.1 is rendered conductive at firing angle ϕ by gate pulse GP1. During this mode, current flows from the supply to the load. When the current through Th.1 goes through zero, Th.1 opens. This is when Mode B begins. During this mode, both Th.1 and Th.2 are open, that is, the load is disconnected from the supply. The load now proceeds to resonate due to the charge on the capacitor and current in the load inductance from the previous mode. Mode B continues until $\omega t = \pi + \phi$, when Th.2 is rendered conductive, repeating Mode A for the negative half-cycle. The steady state operation of the system then consists of the repetition of Modes A and B in the positive and negative half-cycles.

Representation of Load

The true reflected impedance of an induction heating load is a complicated function dependent on the coupling between load and work coil and on the resistivity, permeability and temperature of the load. The frequency of operation and the geometry of the load also contribute to the reflected impedance.

However, if one considers the total net effect of all the factors mentioned above, the induction heating load can be represented by a series RL network where R is the reflected resistance and L is the reflected inductance of the load. Since the typical induction load has a low power factor - typical values are .1 - .3, with occasional values up to .7 - parallel power factor correcting capacitors are used for better supply current versus power utilization. Normally, an induction heating load is corrected to nearly unity power factor. The basic model of the load is shown in Fig.3.
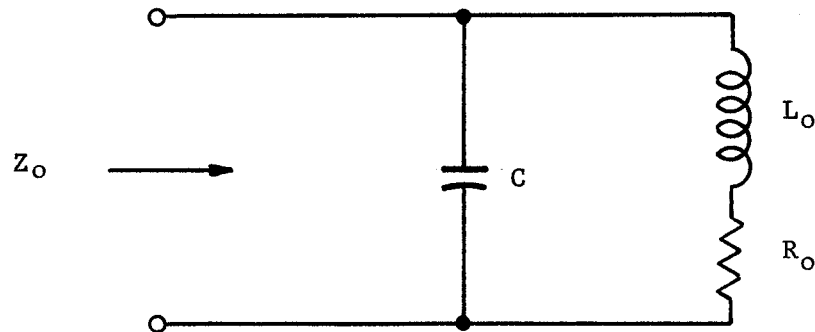
Fig. 3   Basic model of parallel compensated induction load

Definition of Terms

The parallel load as shown in Fig.3 consists of the basic parameters R_O, L_O and C. In the following chapters, the load will be characterized by:

Req - the impedance of the load to fundamental frequency at unity power factor.

Q - the quality factor of the load.

PF - the load power factor.

The equivalent impedance of the load at unity power factor is given by the equation

$$Req = \frac{L_O}{R_O \, C} \tag{1}$$

In general, Req will be normalized to unity.

The quality factor Q is defined by the equation

$$Q = \frac{\omega L_O}{R_O} \tag{2}$$

where $\omega = 2\pi f$ in rad/sec and f is the fundamental supply frequency in Hertz.

In a practical circuit, the load power factor is held close to unity by periodic adjustments of the parallel capacitors. However, due to the rapid changes of the load, the power factor is held within a fixed lead-lag band. To simulate these conditions, the value of the parallel capacitance C is varied, with R_O and L_O held constant until the desired load power factor is obtained. The normalized magnitude of the load impedance at any operating power factor is then given by the equation

where n = 3, 5, 7...
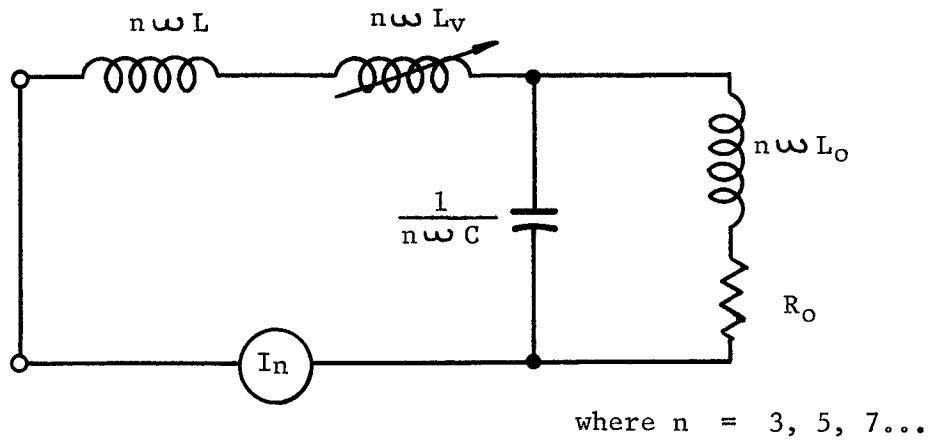
Fig. 5   Harmonic model of controller
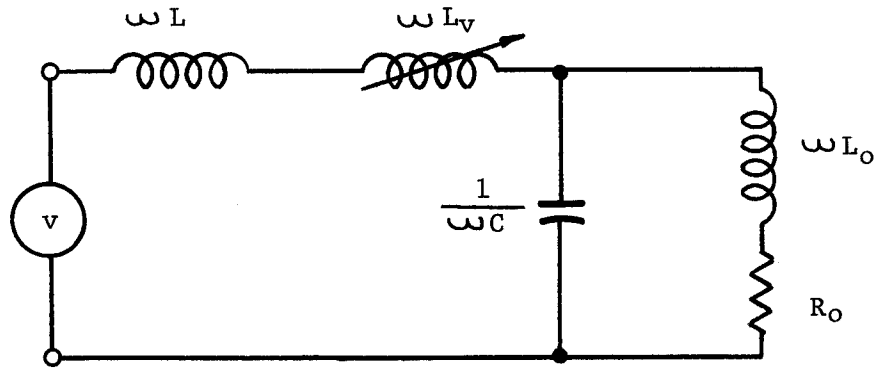
Fig. 6   Fundamental model of controller

A brief numerical example using the harmonic representation of the compensated load illustrates well the shunting effect of the load power factor correcting capacitor. For a load whose $Q = 3$, it can be shown that at the fundamental frequency,

$$R_{o(1)} = \frac{1}{Q^2+1} = \frac{1}{10} = .1 \quad ,$$

$$X_{Lo(1)} = Q\, R_o = \frac{3}{10} = .3 \quad \text{and}$$

$$X_{C(1)} = \frac{1}{Q} = \frac{1}{3} \doteq .33 \quad .$$

At the third harmonic frequency,

$$R_{o(3)} = \frac{1}{10} = .1 \quad ,$$

$$X_{Lo(3)} = \frac{9}{10} = .9 \quad \text{and}$$

$$X_{C(3)} = \frac{1}{9} = .11 \quad .$$

The above simple calculations show that at the third harmonic frequency the capacitance has about one ninth the impedance of the inductive load. It is not difficult to see that for higher harmonics the capacitance acts nearly as a short circuit compared to the inductive load.

Analysis Using Circle Diagrams

Making use of the fundamental model, the controller's behavior under various load conditions can be analyzed with the help of circle diagrams. The following figures show the controller behavior from full conduction to $\phi = 180^\circ$.

14

In Fig. 7,   Req = 1.0 Ohm, PF = 1.0 and X_L = .2 Ohm.

In Fig.8, PF = .9 and in Fig.9, PF = - .9. In all three figures,

the constant supply voltage V is assumed as a reference. As

the variable reactance ωL_v in the equivalent circuit of Fig. 6 is

increased, the locus of the line current phasor I_L describes the

semi-circle a_0 . The projection of I_L on the real axis gives the

average power. The locus of the output voltage phasor V_c describes

the semi-circle b_0. Note that phasor V_c is in phase, leads or lags

phasor I_L , depending on the power factor of the load. The cosine

of the angle between the reference phasor V and the phasor I_L is

the input power factor of the system. The magnitude and phase of the

voltage across the line reactances X_L and ωL_v can be readily

obtained by making use of the fact that the voltage drops across the

load and the line reactances must always add up to the supply voltage.

The behavior of line current, output voltage and power, as well

as the fundamental power factor of the system, can be obtained readily

throughout the whole control range. A verification of the accuracy of

this approximate method of analysis will be presented in Chapter IV

where experimental results will be compared to predicted results, using

the approximate as well as the exact computer method of analysis.
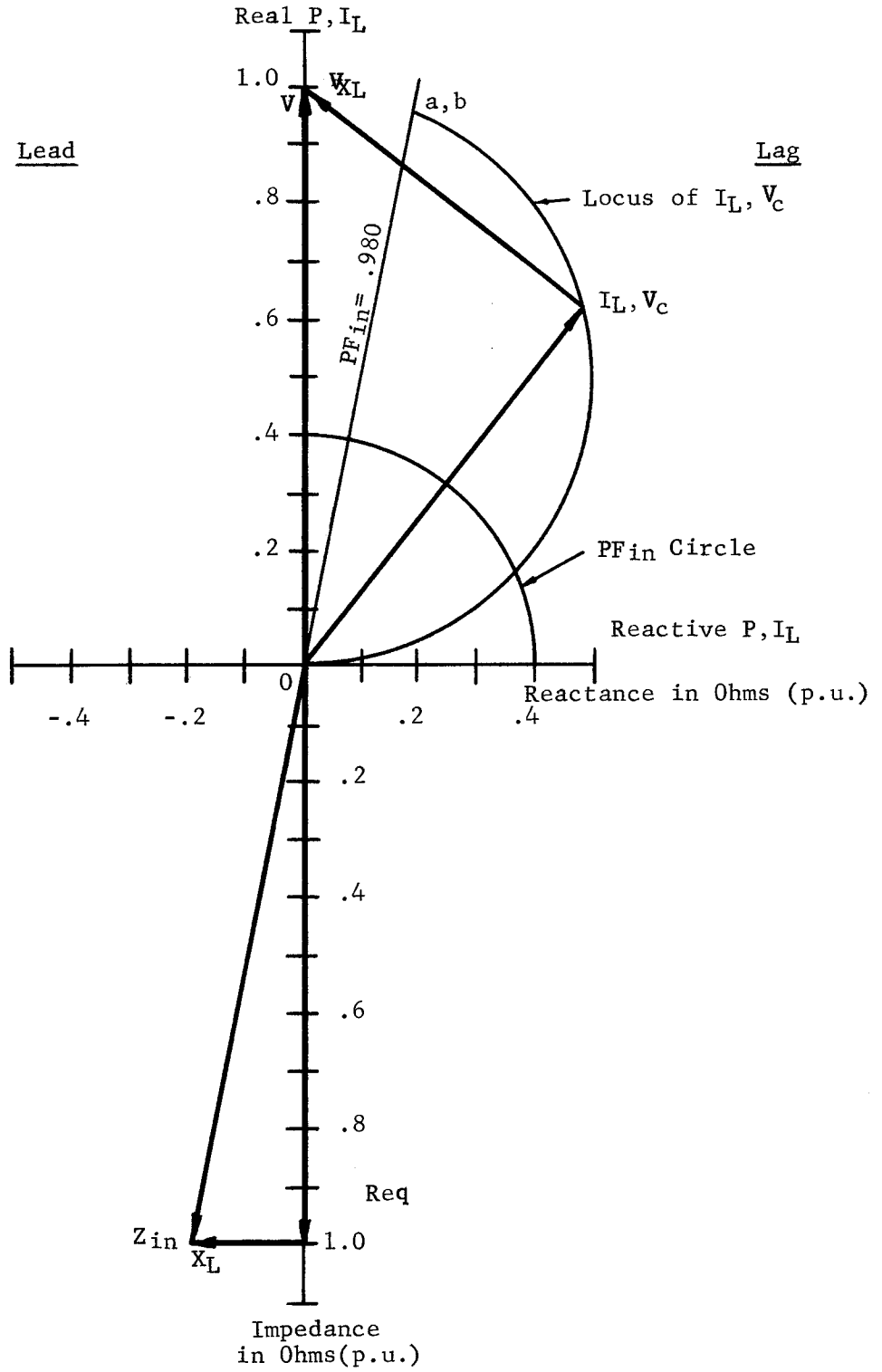
Fig.7   Circle Diagram, $X_L = .2$,   PF = 1.0
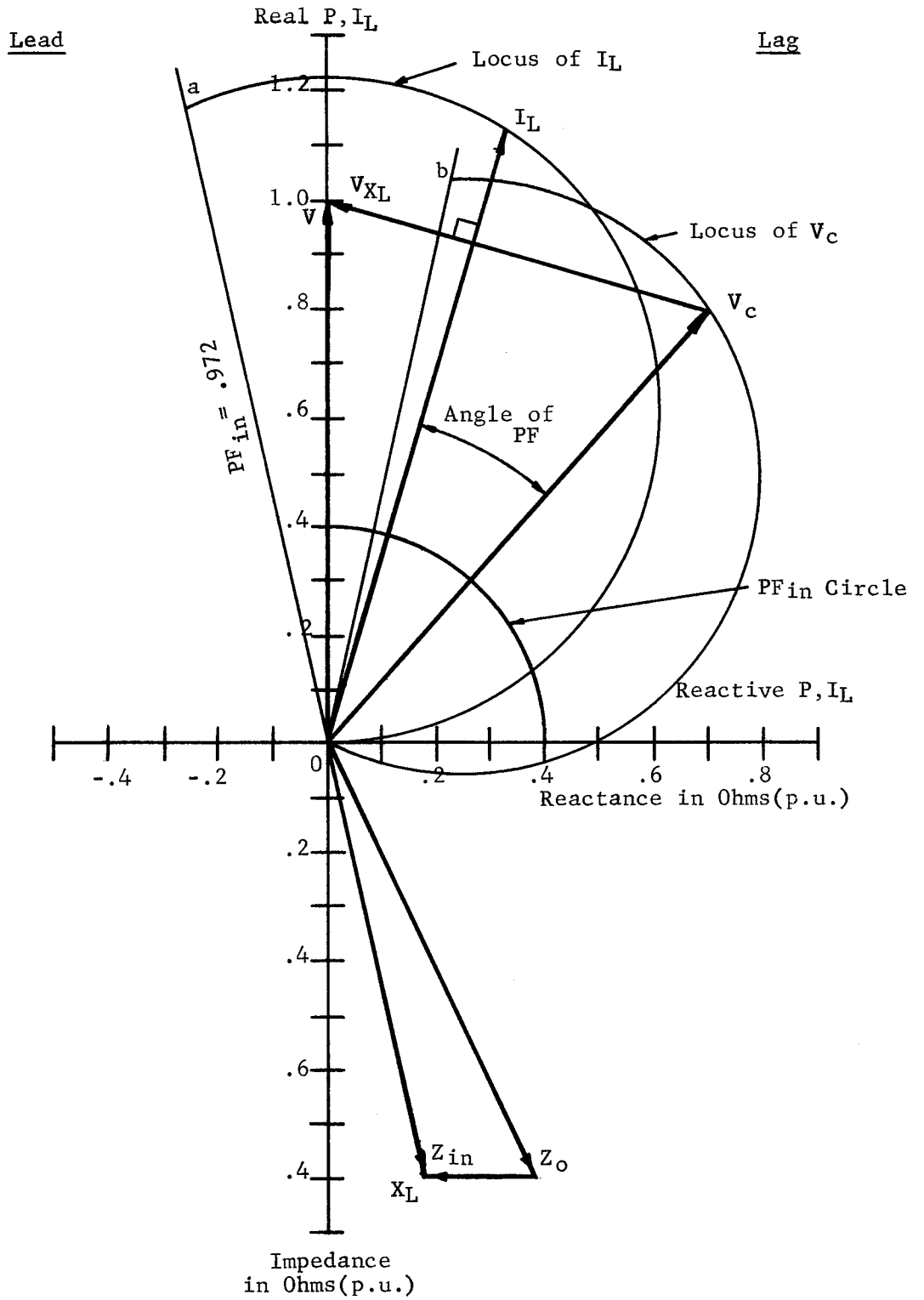
Fig.8   Circle Diagram, $X_L = .2$,   PF = .9
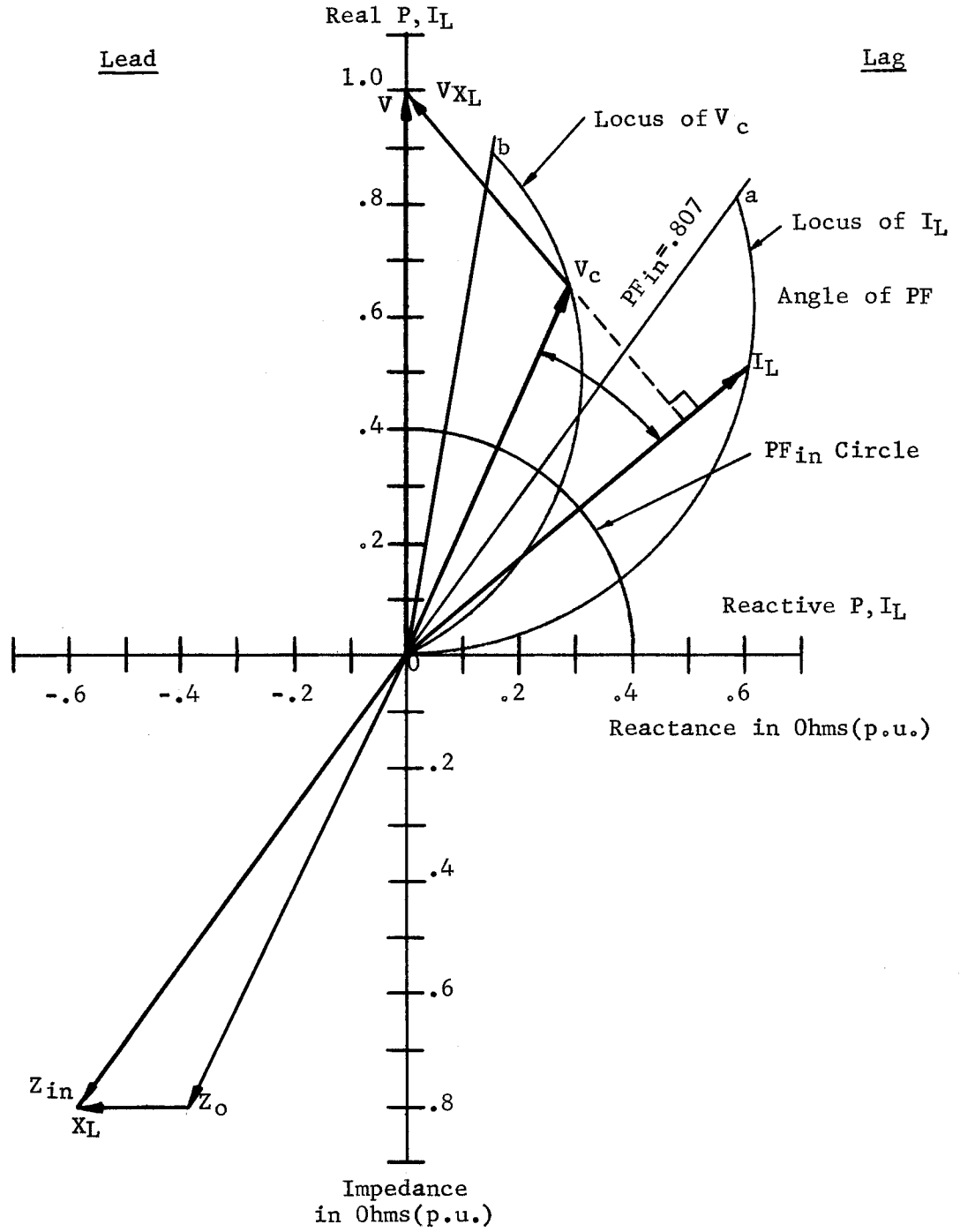
Fig. 9   Circle Diagram, X_L =   .2,   PF = -.9

Conclusions

In this chapter, a steady state analysis of the controller has been developed. Simplifying assumptions were made which allowed the use of circle diagrams. An approximate system performance for load Q's $\gtreqless$ 3 was predicted. Based on this analysis, a Q-independent nature of the system can be predicted for load Q's $\gtreqless$ 3 .

CHAPTER   IV

EXACT ANALYSIS

An exact analysis of the controller system is presented in
this chapter. The analysis which is developed has the advantage that
transient as well as steady state results can be obtained without the
use of an excessive amount of computer time. Furthermore, the following
is presented in this chapter:

(a)   Mathematical derivations.

(b)   The development of equations for the circuit voltages and

      currents.

(c)   Prediction of system performance.

(d)   Experimental verification of theoretical results.

(e)   Comparison of exact and approximate theoretical results.

Discussion

In order to predict the exact steady state and transient per-
formance of the system, to study system behavior under widely varying
load conditions, to observe the relationships between circuit compo-
nents and system performance and to find the criteria for the most
economical and best performing system, an exact analysis must be
undertaken.

When a system's performance must be evaluated for widely vary-
ing conditions, experimental methods of analysis must be ruled out
since they are time consuming and costly. A simulation method employing

a digital computer lends itself particularly well to handling large amounts of data. If a large number of variables are involved, a computer is a necessity.

While the experimental work can not be completely replaced by computer simulation, this simulation, if used judiciously, can be an effective and efficient aid in design work.

Methods of Analysis

There are many mathematical methods available for analyzing dynamic systems. The most commonly used techniques are the numerical and the operational methods. In recent years, the method of state variables, in conjunction with the Laplace transform and its inverse, has gained wide usage.

The state variable method is based on the fact that the output of a system depends entirely on its condition or state in the past (initial conditions) and on its present input (forcing function). The state variable method has a number of advantages over the conventional loop and/or node analysis techniques. One of these is that the state variable method decomposes a complex system into a set of simpler interacting systems which then can be solved one at a time quite readily. Another distinct advantage of the state variable method is that direct information about the past state of the system is immediately obtainable from the state variables.

Each of the above methods requires the development of the system equations. In applying numerical techniques, less analytical work is required but computer time may be excessive. The selection of

appropriate step sizes can have a great bearing on obtaining stable and accurate solutions. The operational methods require a great deal more analytical work but much less computer time is required. Step sizes are of no great significance and a relatively clear picture can be obtained between the relationship of the circuit parameters and the circuit functions.

In this chapter, the state variable method is used in conjunction with Laplace and inverse transformations. This method was chosen because of the following considerations:

    (a)   Suitable for computer-aided analysis.

    (b)   Short computer time required.

    (c)   Solutions as a function of time are exact and are independent of step size.

    (d)   Vital circuit voltages and currents can be obtained directly.

Mathematical Derivations

When using the state variables method, the system state equations must be developed and written in matrix form. Next, the Laplace transform of the matrices is taken and the system is solved for the state variables with all possible initial conditions. Inverse transformation of the system then yields the state variables in the time domain. When the time functions of the state variables (currents, voltages) are obtained, their simulation on a digital computer can proceed directly. In the simulation process, the end conditions of a circuit operating mode are the initial conditions of the next mode of circuit operation. When the initial conditions for the periodically repeated modes attain a

steady state value the circuit is considered in steady state operation.

The complete circuit is shown in Fig.10. In developing the system equations, the following simplifying assumptions are made:

(a) Thyristor switches used in the circuit are ideal switches, that is, they turn on and off instantaneously, have zero imped- ance when conducting current and infinite impedance when block- ing the flow of current.

(b) Losses in circuit elements are negligible compared to the power in the load.
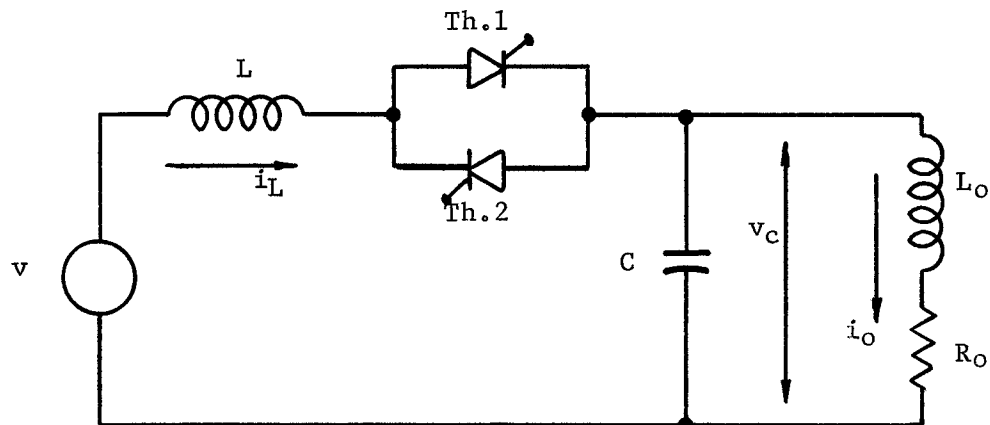
Fig. 10   Complete controller circuit

The complete analysis requires the analysis of two transient modes of circuit operation.

Mode A Operation

Mode A operation is shown in Fig.11.
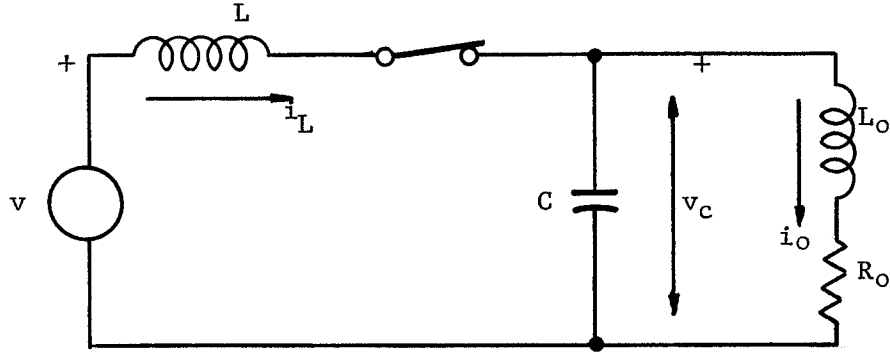
Fig. 11   Equivalent circuit for Mode A operation

The thyristor switch is closed and current flows from the supply to the load. Using Fig.11, the state variable equations are:

$$\frac{d i_L}{dt} = -\frac{v_C}{L} + \frac{v}{L} \tag{6}$$

$$\frac{d v_C}{dt} = \frac{i_L}{C} - \frac{i_o}{C} \tag{7}$$

$$\frac{d i_o}{dt} = \frac{v_C}{L_o} - \frac{i_o R_o}{L_o} \tag{8}$$

Written in matrix form, Equations (6), (7) and (8) are:

$$
\begin{bmatrix} \dfrac{di_L}{dt} \\[3mm] \dfrac{di_o}{dt} \\[3mm] \dfrac{dv_C}{dt} \end{bmatrix}
=
\begin{bmatrix} 0 & 0 & -\dfrac{1}{L} \\[3mm] 0 & -\dfrac{R_o}{L_o} & \dfrac{1}{L_o} \\[3mm] \dfrac{1}{C} & -\dfrac{1}{C} & 0 \end{bmatrix}
\begin{bmatrix} i_L \\[3mm] i_o \\[3mm] v_C \end{bmatrix}
+
\begin{bmatrix} \dfrac{1}{L} \\[3mm] 0 \\[3mm] 0 \end{bmatrix}
\begin{bmatrix} v \end{bmatrix}
\tag{9}
$$

Equation (9) can be written in general matrix form as

$$
\underline{\dot{x}} = \underline{A}\,\underline{x} + \underline{B}\,\underline{r} \tag{10}
$$

The general form of the sinusoidal forcing function v can be written as

$$
v = A \sin(\omega t + \phi) \tag{11}
$$

Expanding equation (11) yields

$$
v = A(\sin \omega t \cos \phi + \cos \omega t \sin \phi) \tag{12}
$$

and the Laplace transform of v is:

$$
\mathcal{L}(v) = \frac{A}{s^2 + \omega^2}(\omega \cos \phi + s \sin \phi) \tag{13}
$$

Taking the Laplace transform of equation (10) and solving for $X(s)$ with all possible initial conditions, we have

$$
\underline{X}(s) = \left[s\underline{I} - \underline{A}\right]^{-1} \underline{x}(0^+) + \left[s\underline{I} - \underline{A}\right]^{-1} \underline{B}(s)\,\underline{R}(s) \tag{14}
$$

Written in terms of the circuit components of Fig.11, equation (14) is:

$$\begin{bmatrix} I_L(s) \\ I_o(s) \\ V_c(s) \end{bmatrix} = \frac{\begin{bmatrix} s^2 + s\frac{R_o}{L_o} + \frac{1}{L_oC} & \frac{1}{LC} & s(-\frac{1}{L}) - \frac{R_o}{LL_o} \\ \frac{1}{L_oC} & s^2 + \frac{1}{LC} & s\frac{1}{L_o} \\ s\frac{1}{C} + \frac{R_o}{L_oC} & s\frac{1}{C} & s^2 + s\frac{R_o}{L_o} \end{bmatrix} \begin{bmatrix} i_L(0^+) \\ i_o(0^+) \\ v_c(0^+) \end{bmatrix}}{\det\begin{bmatrix} s\underline{I} - \underline{A} \end{bmatrix}}$$

$$+ \frac{\begin{bmatrix} s^2 + s\frac{R_o}{L_o} + \frac{1}{L_oC} & \frac{1}{LC} & s(-\frac{1}{L}) - \frac{R_o}{LL_o} \\ \frac{1}{L_oC} & s^2 + \frac{1}{LC} & s\frac{1}{L_o} \\ s\frac{1}{C} + \frac{R_o}{L_oC} & s\frac{1}{C} & s^2 + s\frac{R_o}{L_o} \end{bmatrix} \begin{bmatrix} \frac{1}{L} \\ 0 \\ 0 \end{bmatrix}}{\det\begin{bmatrix} s\underline{I} - \underline{A} \end{bmatrix}}$$

$$\times \left[\frac{A}{s^2 + \omega^2}(\omega\cos\phi + s\sin\phi) \right] \quad , \tag{15}$$

where $\det\begin{bmatrix} s\underline{I} - \underline{A} \end{bmatrix}$ is the determinant of the matrix $\begin{bmatrix} s\underline{I} - \underline{A} \end{bmatrix}$ and is given by

$$\det\begin{bmatrix} s\underline{I} - \underline{A} \end{bmatrix} = s^3 + s^2\frac{R_o}{L_o} + s\left(\frac{1}{LC} + \frac{1}{L_oC}\right) + \frac{R_o}{LL_oC} \tag{16}$$

The roots of equation (16) are the roots of the characteristic equation of the system. They may be either all real or one may be real while the other two are complex conjugate pairs. In what follows, the latter case is assumed since in all practical induction loads the load circuit is of the underdamped oscillatory type.

The first part of matrix equation (15) is only a function of the initial conditions and the second part is a function of the forcing function or input only. This shows clearly how the outputs or state variables of a given system are strictly a function of the state in the past (initial conditions),or part one of equation (15), and of the present

input (forcing function), or part two of equation (15).

Once the roots of det $\begin{bmatrix} s\underline{I} - \underline{A} \end{bmatrix} = 0$ are found, the exact expressions for the state variables as a function of time can be obtained with the aid of the inverse Laplace transformations. The state variables as a function of time can be written as:

$$i_L = AL \; \varepsilon^{-Yt} \sin(Zt + \alpha_1) + \frac{A1 - A2X + A3X^2}{(Y - X)^2 + Z^2} \; \varepsilon^{-Xt}$$

$$+ \frac{B1 - B2X + B3X^2 - B4X^3}{(X^2 + \omega^2)\left[(Y-X)^2 + Z^2\right]} \; \varepsilon^{-Xt}$$

$$+ AB \; \sin(\omega t + \alpha_2) + B \; \varepsilon^{-Yt} \sin(Zt + \beta) \;, \qquad (17)$$

where

$$AL \lfloor \alpha_1 = \frac{A1 - A2(Y - jZ) + A3(Y - jZ)^2}{Z(X - Y + jZ)} \;,$$

$$AB \lfloor \alpha_2 = \frac{B1 + B2(j\omega) + B3(j\omega)^2 + B4(j\omega)^3}{\omega\left[(j\omega + Y)^2 + Z^2\right](j\omega + X)} \;,$$

$$B \lfloor \beta = \frac{B1 - B2(Y - jZ) + B3(Y - jZ)^2 - B4(Y - jZ)^3}{Z\left[(Y - jZ)^2 + \omega^2\right](X - Y + jZ)} \;.$$

$$i_o = CL \; \varepsilon^{-Yt} \sin(Zt + \gamma_1) + \frac{C1 - C2X + C3X^2}{(Y - X)^2 + Z^2} \; \varepsilon^{-Xt}$$

$$+ \frac{D1 - D2X}{(X^2 + \omega^2)\left[(Y - X)^2 + Z^2\right]} \; \varepsilon^{-Xt}$$

$$+ CB \; \sin(\omega t + \gamma_2) + D \; \varepsilon^{-Yt} \sin(Zt + \delta) \;, \qquad (18)$$

where

$$CL \lfloor \gamma_1 + \frac{C1 - C2(Y - jZ) + C3(Y - jZ)^2}{Z(X - Y + jZ)} \;,$$

$$CB \lfloor \gamma_2 = \frac{D1 + D2(j\omega)}{\omega\left[(j\omega + Y)^2 + Z^2\right](j\omega + X)} \;,$$

$$D\underline{/\sigma} = \frac{D1 - D2\ (Y - jZ)}{Z\ \left[(Y - jZ)^2 + \omega^2\right]\ (X - Y + jZ)} \quad .$$

$$v_c = EL\ \varepsilon^{-Yt}\ \sin(Zt + \rho_1) + \frac{E1 - E2X + E3X^2}{(Y - X)^2 + Z^2}\ \varepsilon^{-Xt}$$

$$+ \frac{F1 - F2X + F3X^2}{(X^2 + \omega^2)\ \left[(Y - X)^2 + Z^2\right]}\ \varepsilon^{-Xt}$$

$$+ EB\ \sin(\omega t + \rho_2) + F\ \varepsilon^{-Yt}\ \sin(Zt + \sigma)\ , \tag{19}$$

where

$$EL\underline{/\rho_1} = \frac{E1 - E2\ (Y - jZ) + E3\ (Y - jZ)^2}{Z\ (X - Y + jZ)}$$

$$EB\underline{/\rho_2} = \frac{F1 - F2\ (j\omega) + F3(j\omega)^2}{\left[(j\omega + Y)^2 + Z^2\right]\ (j\omega + X)} \quad ,$$

$$F\underline{/\sigma} = \frac{F1 - F2\ (Y - jZ) + F3\ (Y - jZ)^2}{Z\ \left[(Y - jZ)^2 + \omega^2\right]\ (X - Y + jZ)} \quad .$$

In the above equations, X is the real root of

$\det\left[s\underline{I} - \underline{A}\right] = 0$ and Y and Z are the real and imaginary parts

of the complex conjugate roots of $\det\left[s\underline{I} - \underline{A}\right] = 0$. The subscripted

constants in terms of the circuit constants are:

$$A1 = i_{L(0+)}\ \frac{1}{L_o C} + i_{o(0+)}\ \frac{1}{LC} - v_{c(0+)}\ \frac{R_o}{LL_o}$$

$$A2 = i_{L(0+)}\ \frac{R_o}{L_o} - v_{c(0+)}\ \frac{1}{L}$$

$$A3 = i_{L(0+)}$$

$$B1 = \frac{A\ \omega\ \cos\ \phi}{LL_o C}$$

$$B2 = \frac{A\ \omega\ \cos\ \phi\ R_o}{LL_o} + \frac{A\ \sin\ \phi}{LL_o C}$$

$$B3 = \frac{A\ \omega\ \cos\ \phi}{L} + \frac{A\ \sin\ \phi\ R_o}{LL_o}$$

$$B4 \quad = \quad \frac{A \sin \phi}{L}$$

$$C1 \quad = \quad i_L(0^+) \frac{1}{L_o C} + i_o(0^+) \frac{1}{LC}$$

$$C2 \quad = \quad v_c(0^+) \frac{1}{L_o}$$

$$C3 \quad = \quad i_o(0^+)$$

$$D1 \quad = \quad \frac{A \omega \cos \phi}{L L_o C}$$

$$D2 \quad = \quad \frac{A \omega \sin \phi}{L L_o C}$$

$$E1 \quad = \quad i_L(0^+) \frac{R_o}{L_o C}$$

$$E2 \quad = \quad i_L(0^+) \frac{1}{C} - i_o(0^+) \frac{1}{C} + v_c(0^+) \frac{R_o}{L_o}$$

$$E3 \quad = \quad v_c(0^+)$$

$$F1 \quad = \quad \frac{A \omega \cos \phi \; R_o}{L L_o C}$$

$$F2 \quad = \quad \frac{A \omega \cos \phi \; R_o}{L L_o C} + \frac{A \sin \phi \; R_o}{L L_o C}$$

$$F3 \quad = \quad \frac{A \sin \phi}{LC}$$

where

$A \quad =$ amplitude of supply voltage (Volts)

$f \quad =$ supply frequency (Hertz)

$\omega \quad = \quad 2 \pi f \quad =$ angular frequency of supply voltage (rad/sec)

$\phi \quad =$ phase angle of supply voltage (also firing angle) (degrees)

Equations (17), (18) and (19) completely define the system response for Mode A. All other system voltages and currents can be easily calculated from the above equations. Mode A hence is ready for digital simulation.

Mode B Operation

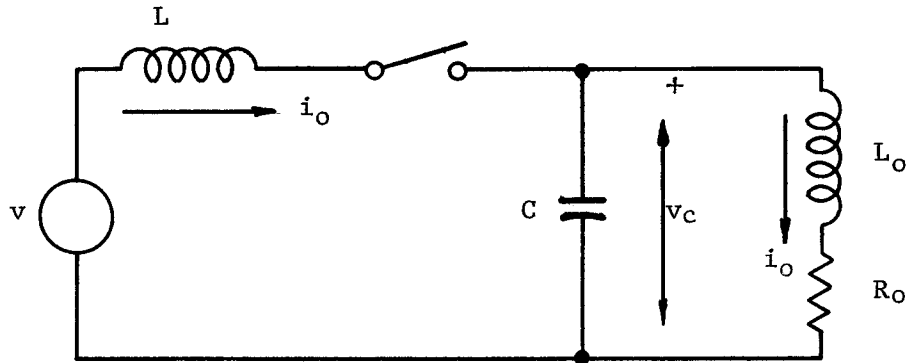Mode B operation is shown in Fig.12.

Fig. 12 Equivalent Circuit for Mode B Operation

The thyristor switch is open. No current flows in the line inductor. The load circuit continues to oscillate due to the initial voltage on the load capacitor and the initial current in the load inductance.

Writing the circuit equations

$$v_c(0+) = \frac{1}{C} \int_0^t i_o dt + L_o \frac{di_o}{dt} + i_o R_o \quad , \quad (20)$$

assuming that the current is a decaying sinusoid,

$$i_o = \varepsilon^{-at} (K1 \cos bt + K2 \sin bt) \quad , \quad (21)$$

where $\quad a = \dfrac{R_O}{2\ L_O}$ $\quad$ and $\quad b = \sqrt{\dfrac{1}{L_O C} - \dfrac{R_O}{4 L_O{}^2}}$, $\quad$ then applying initial

conditions at $\quad t = 0$ which are the final values of Mode $\quad$ A, gives:

$$i_O = i_O(0^+)$$

$$K1 = i_O(0^+)$$

$$\frac{di_O}{dt} = \frac{v_c(0^+) - i_O(0^+)\ R_O}{L_O} \tag{22}$$

$$K2 = \frac{v_c(0^+)}{L_O\ b} - \frac{i_O(0^+)\ a}{b} \tag{23}$$

Substituting $\quad$ K1 $\quad$ and $\quad$ K2 $\quad$ into equation (21), gives:

$$i_O = \varepsilon^{-at} \left[i_O(0^+)\ \cos\ bt + \left(\frac{v_c(0^+)}{L_O\ b} - \frac{i_O(0^+)\ a}{b}\right) \sin\ bt \right] \tag{24}$$

and

$$v_c = v_c(0^+) - L_O\ \frac{di_O}{dt} - i_O\ R_O \ , \tag{25}$$

where $\quad \dfrac{di_O}{dt} \quad$ is given by the equation

$$\frac{di_O}{dt} = -a\ i_O + \varepsilon^{-at} \left[-b\ i_O(0^+)\ \sin\ bt + \left(\frac{v_c(0^+)}{L_O} - \frac{i_O(0^+)\ a}{b}\right) \cos\ bt \right] \tag{26}$$

This concludes the development of the equations for Mode $\quad$ B.

The system equations developed for Modes $\quad$ A $\quad$ and $\quad$ B $\quad$ describe the system response as instantaneous functions of time. Utilizing these equations, a complete digital simulation of the system has been undertaken.

Voltage and Current Expressions in the Circuit

Equations (17), (18) and (19) yield instantaneous values for i_L, i_o and v_c. Utilizing these equations, the remaining circuit voltages and currents can be found readily.

The current i_C in the load capacitor is:

Mode A : $\qquad i_C = i_L - i_o$ $\hfill$ (27)

Mode B : $\qquad i_C = - i_o$ $\hfill$ (28)

The voltage v_L across the series inductor is:

Mode A : $\qquad v_L = v - v_c$ $\hfill$ (29)

Mode B : $\qquad v_L = 0$ $\hfill$ (30)

The voltage v_{Th} across the thyristors is:

Mode A : $\qquad v_{Th} = 0$ $\hfill$ (31)

Mode B : $\qquad v_{Th} = v - v_c$ $\hfill$ (32)

Determination of Rms Circuit Quantities

Once steady state operating conditions are reached in the circuit, the rms circuit voltages and currents are of primary interest. The rms quantities were arrived at in the following manner:

$$I_L = \sqrt{\frac{1}{T} \sum_{n=1}^{n=m} \left(\frac{i_n + i_{n-1}}{2} \right)^2 \Delta t} \quad , \qquad (33)$$

where i_n = instantaneous value of current, t = incremental time and

$T = m \triangle t$ _is the period.

Power and Power Factor

The average power transferred to the load is given by:

$$P = I_o^2 R_o \quad , \tag{34}$$

where I_o is the rms value of i_o.

The input power factor is given by:

$$PF_{in} = \frac{P}{V I_L} \quad . \tag{35}$$

Harmonic Analysis

In order to obtain the harmonic content of the line current, Fourier analysis is utilized.

$$i_L = a_o + \sum_{n=1}^{\infty} (a_n \cos n\omega t + b_n \sin n\omega t) \tag{36}$$

or

$$i_L = \sum_{n=1}^{\infty} C_n \sin (n\omega t + \theta_n) \quad , \tag{37}$$

where

$$a_o = \frac{1}{T} \int_0^T i_L(t) \, dt$$

$$a_n = \frac{2}{T} \int_0^T i_L(t) \cos n\omega t \, dt$$

$$b_n = \frac{2}{T} \int_0^T i_L(t) \sin n\omega t \, dt$$

$$C_n = \sqrt{a_n^2 + b_n^2}$$

$$\theta_n = \tan^{-1} (a_n/b_n)$$

The magnitude of the fundamental component of i_L and its phase angle with respect to the line voltage v is given by :

$$c_1 = \sqrt{a_1{}^2 + b_1{}^2} \tag{38}$$

$$\theta_{ph} = \phi - \tan^{-1}(a_1/b_1) \tag{39}$$

The fundamental input power factor of the system then is given by:

$$PF_{ph} = \cos\theta_{ph} \tag{40}$$

and the fundamental input power by:

$$P_{ph} = \frac{A\ c_1}{2}\cos\theta_{ph} \tag{41}$$

Prediction of System Performance

The choice of system parameters for the results presented in the following sections were based on:

1. Economical considerations for a practical system,

2. Considerations involving a practical load,

3. Practical and theoretical considerations involving system stability.

The following system parameters are used throughout the following sections:

$$X_L = .0714,\ .1,\ .2,\ .286$$

$$Req = 1.0$$

$$PF = -.9,\ 1.0,\ .9$$

$$Q = 1,\ 2,\ 5,\ 10$$

Conduction Angle Versus Firing Angle

The plots of conduction angle versus firing angle for load power factors of -.9 (lagging), 1.0 and .9 (leading), with various values of line inductances are shown in Figs. 13 through 23. The plots are shown in the order of increasing Q's. Examination of the curves permits the following observations to be made:

1. The conduction angle is a non-linear function of the firing angle.

2. For the same firing angle the conduction angle decreases with X_L.

3. For $Q \gtreqless 2$ and $X_L \gtreqless .2$, the system is stable for all firing angles.

4. For $Q \gtreqless 5$, these characteristic curves are nearly independent of the load Q.

5. Stability increases with load Q.

6. The system is more stable for leading power factor loads.

7. Stability increases with X_L .

8. Instabilities occur at low firing angles.

9. For certain conditions, a jump phenomenon can be observed.

10. Under certain conditions, the system does not become unstable but two jumps occur as the firing angle is increased or decreased (see arrows on Figs. 15 and 16).

The system is considered unstable if unsymmetrical currents flow in the supply line despite the symmetrical gating of the thyristors. This causes d.c. and subharmonics to flow in the line, causing the saturation of the supply transformer.
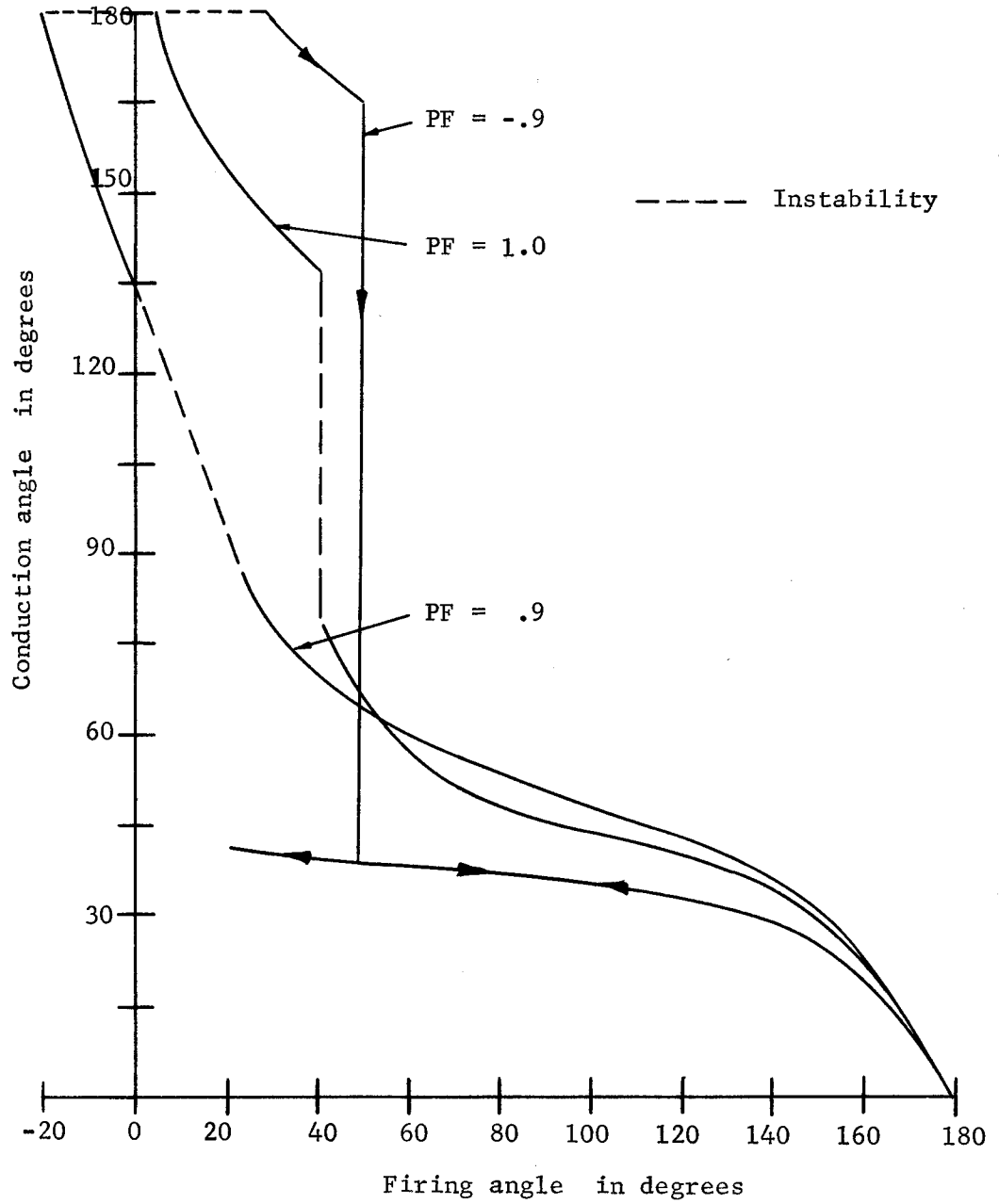
Fig. 13   Conduction angle vs. firing angle
           for Q = 1.0   and X_L = .0714
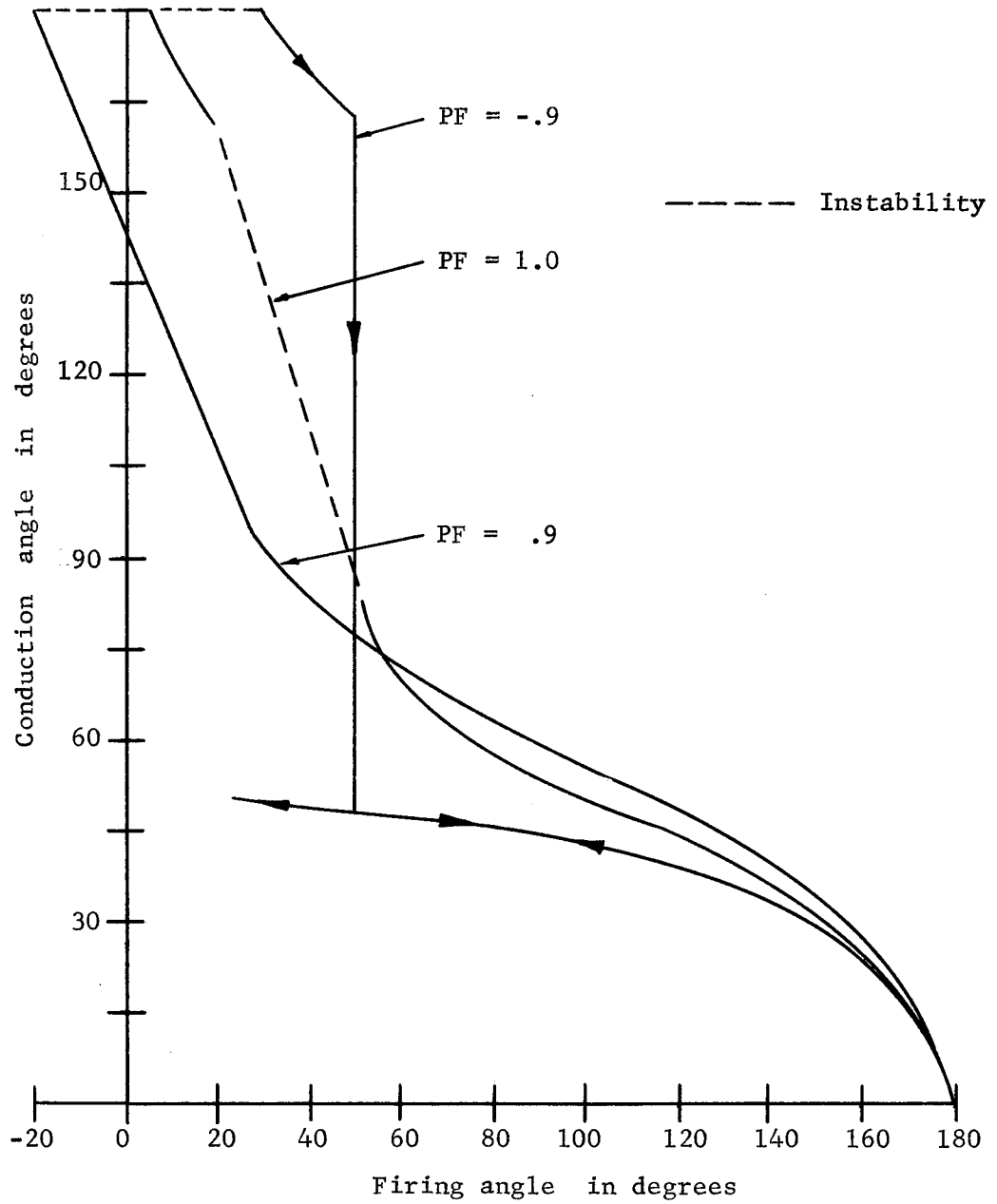
Fig. 14   Conduction angle vs. firing angle
for   Q = 1.0   and X_L = .1
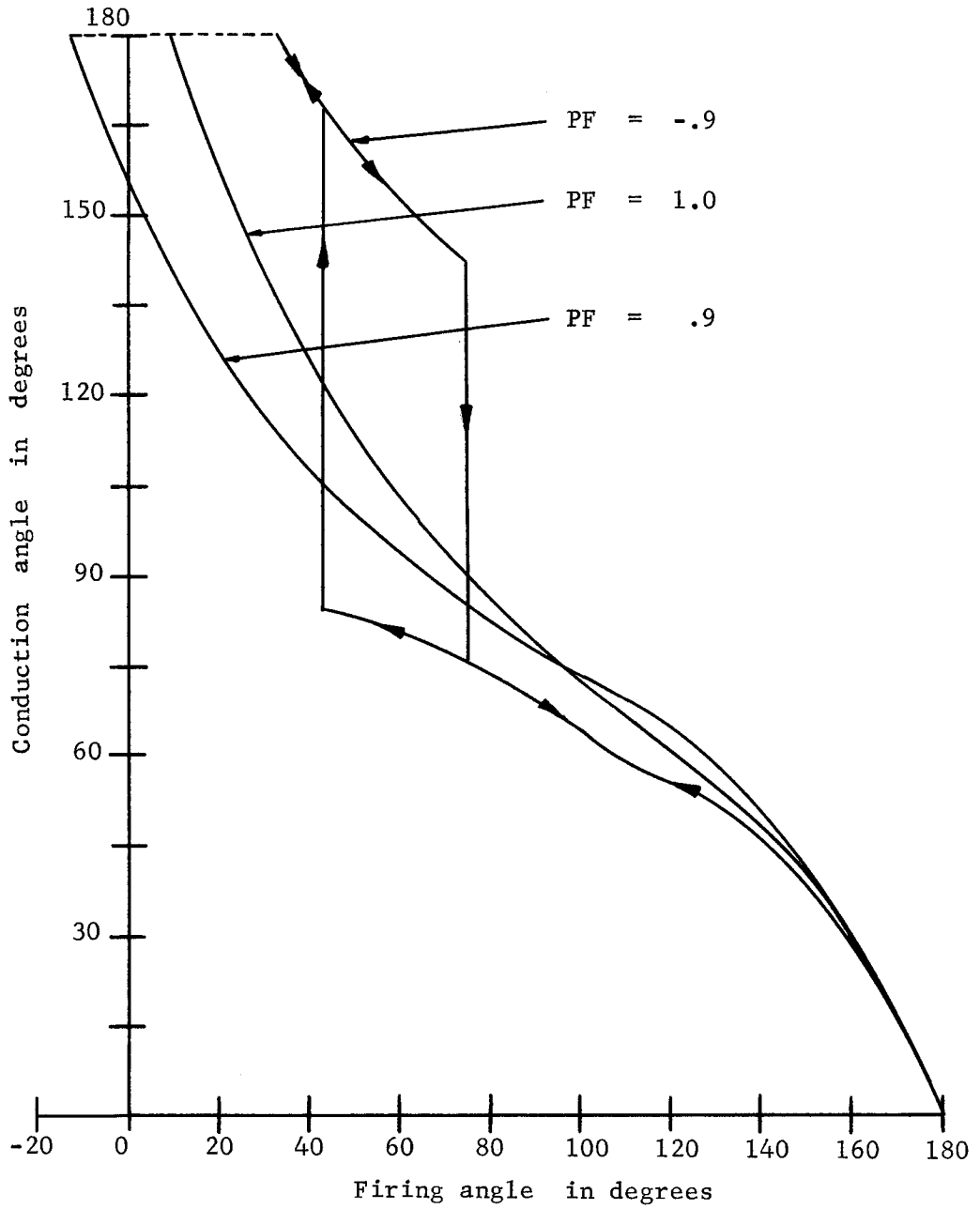
Fig. 15   Conduction angle vs. firing angle
           for Q = 1.0 and X_L = .2
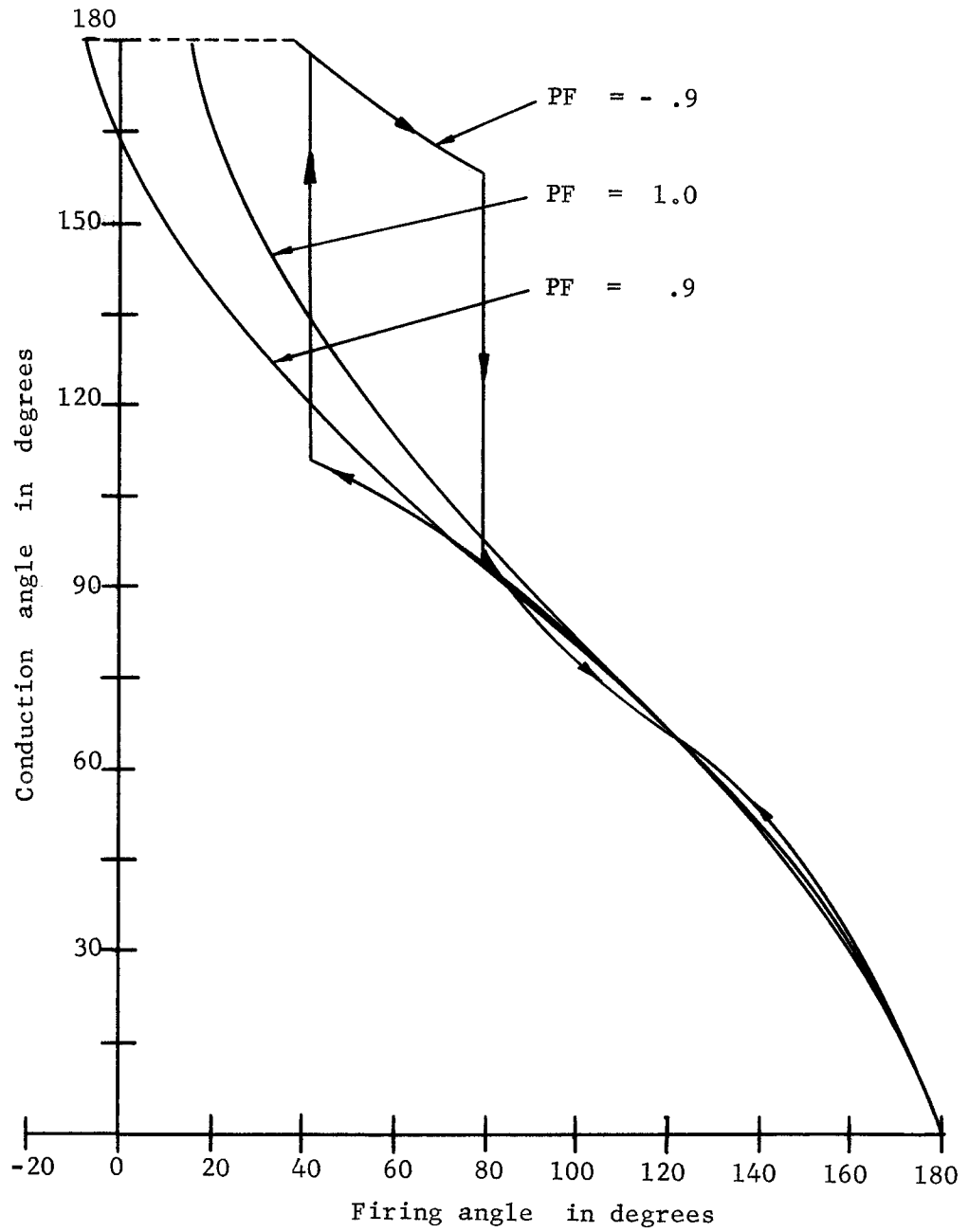
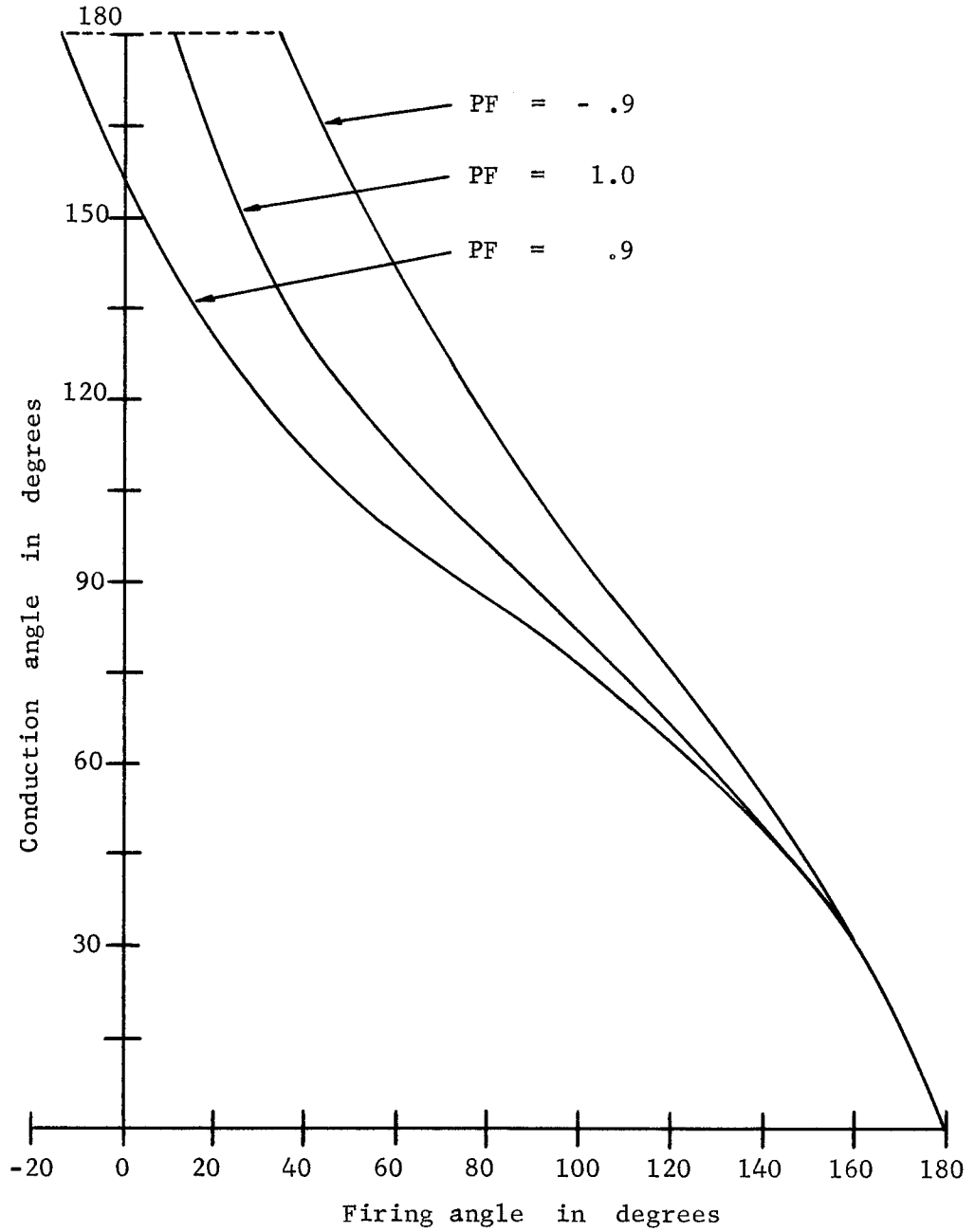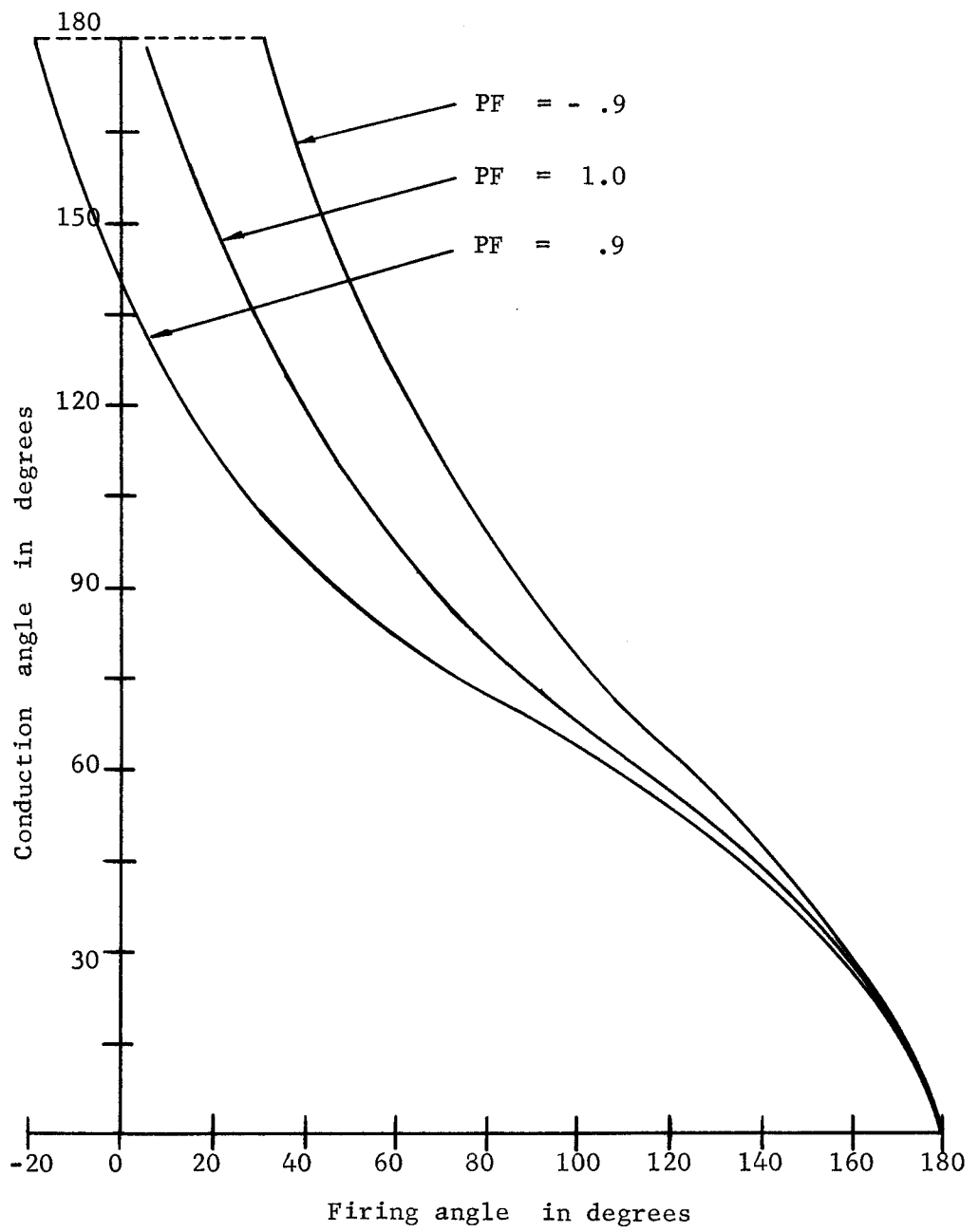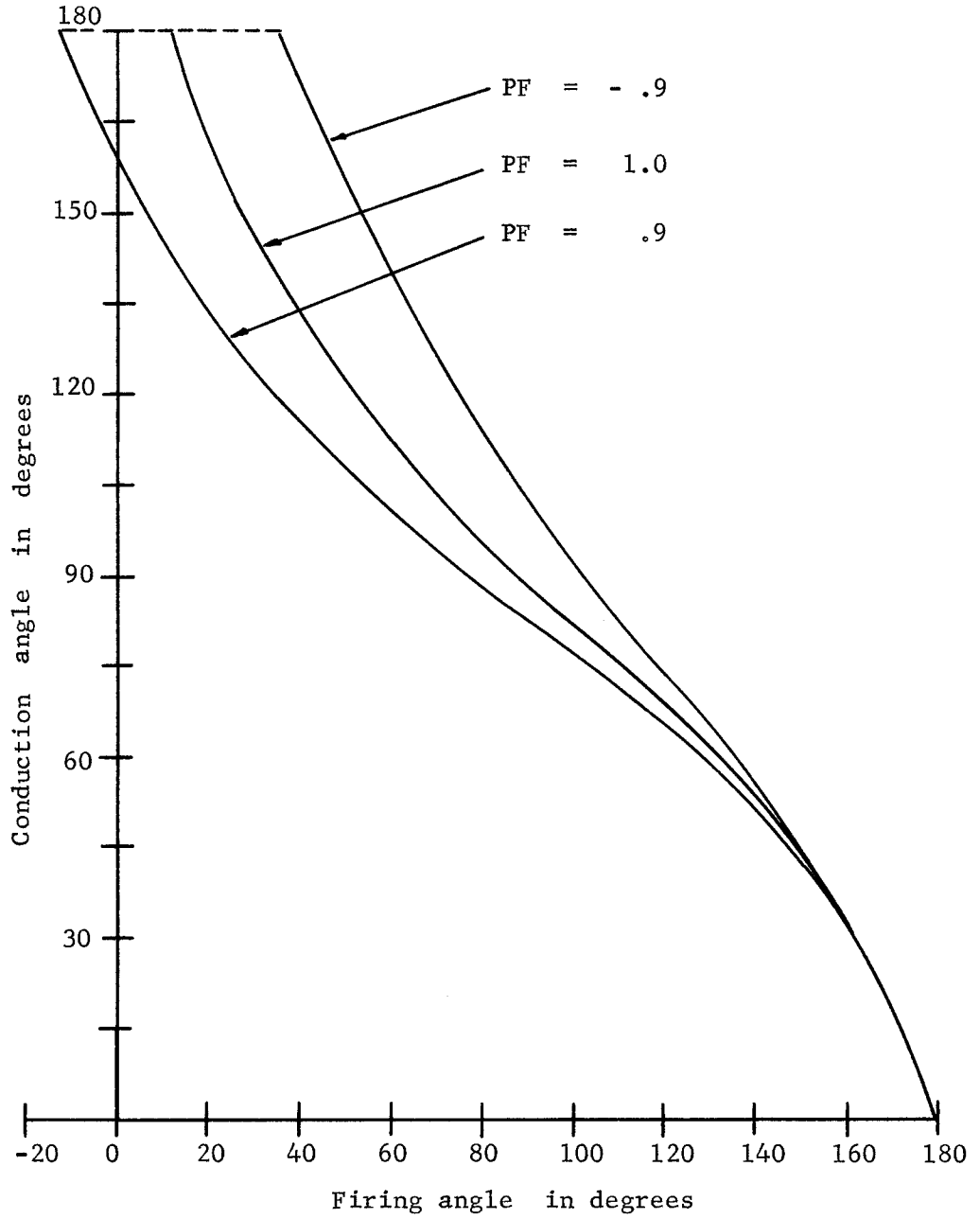Fig. 16   Conduction angle vs. firing angle
for   Q =   1.0   and X_L =   .286
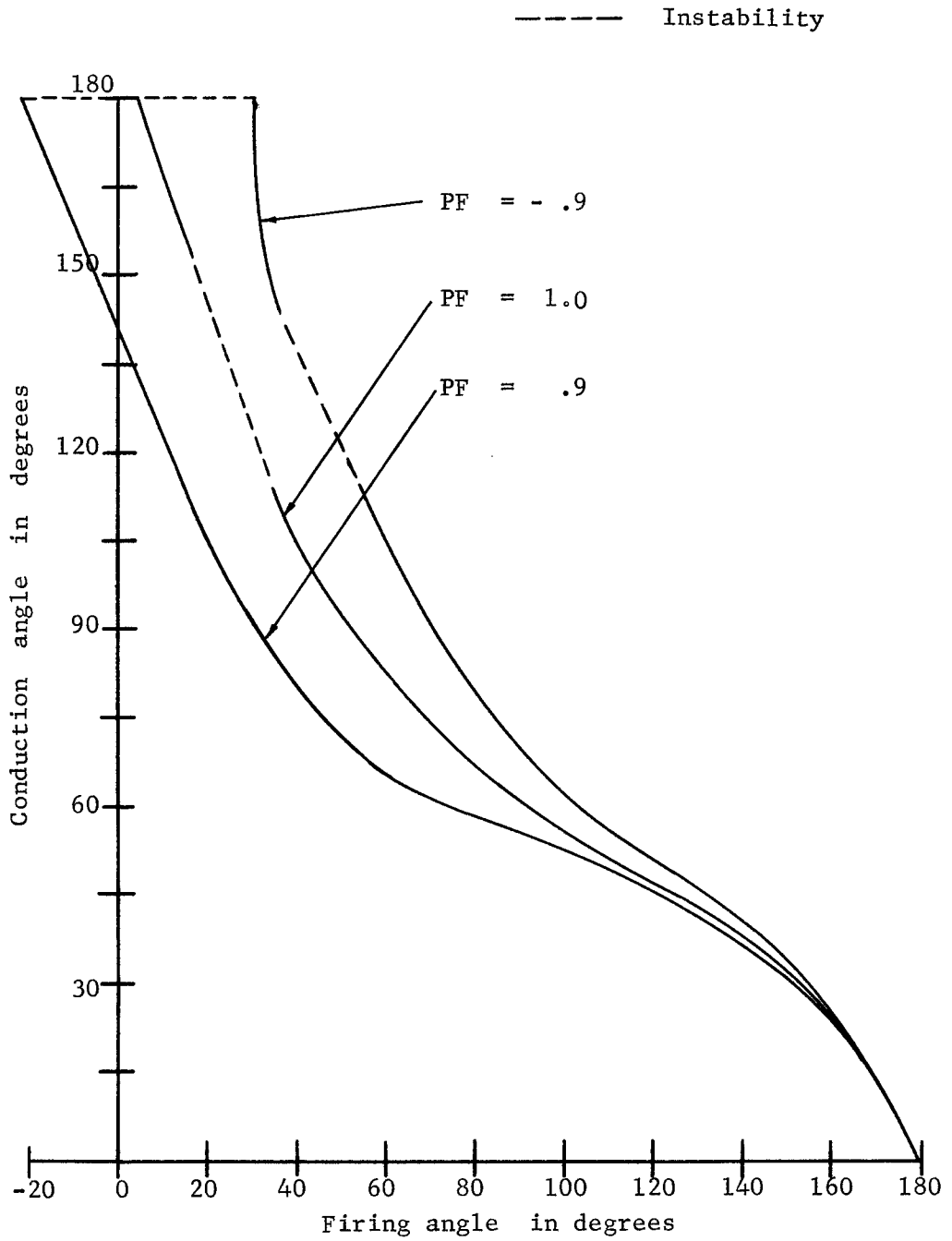
Fig. 17   Conduction angle vs. firing angle
for Q = 2.0 and X_L = .0714
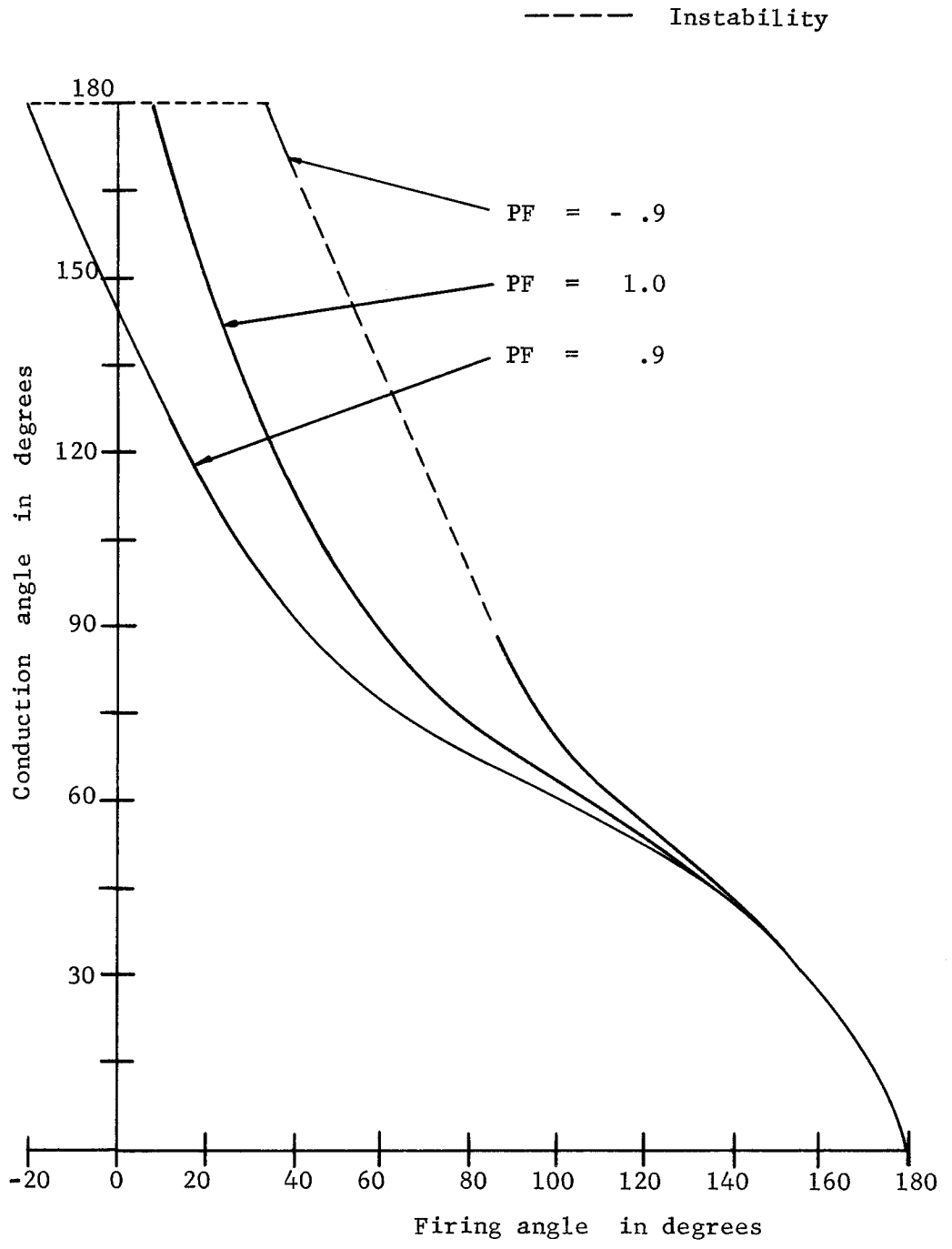
Fig. 18   Conduction angle vs. firing angle
for   Q = 2.0   and X_L =   .1
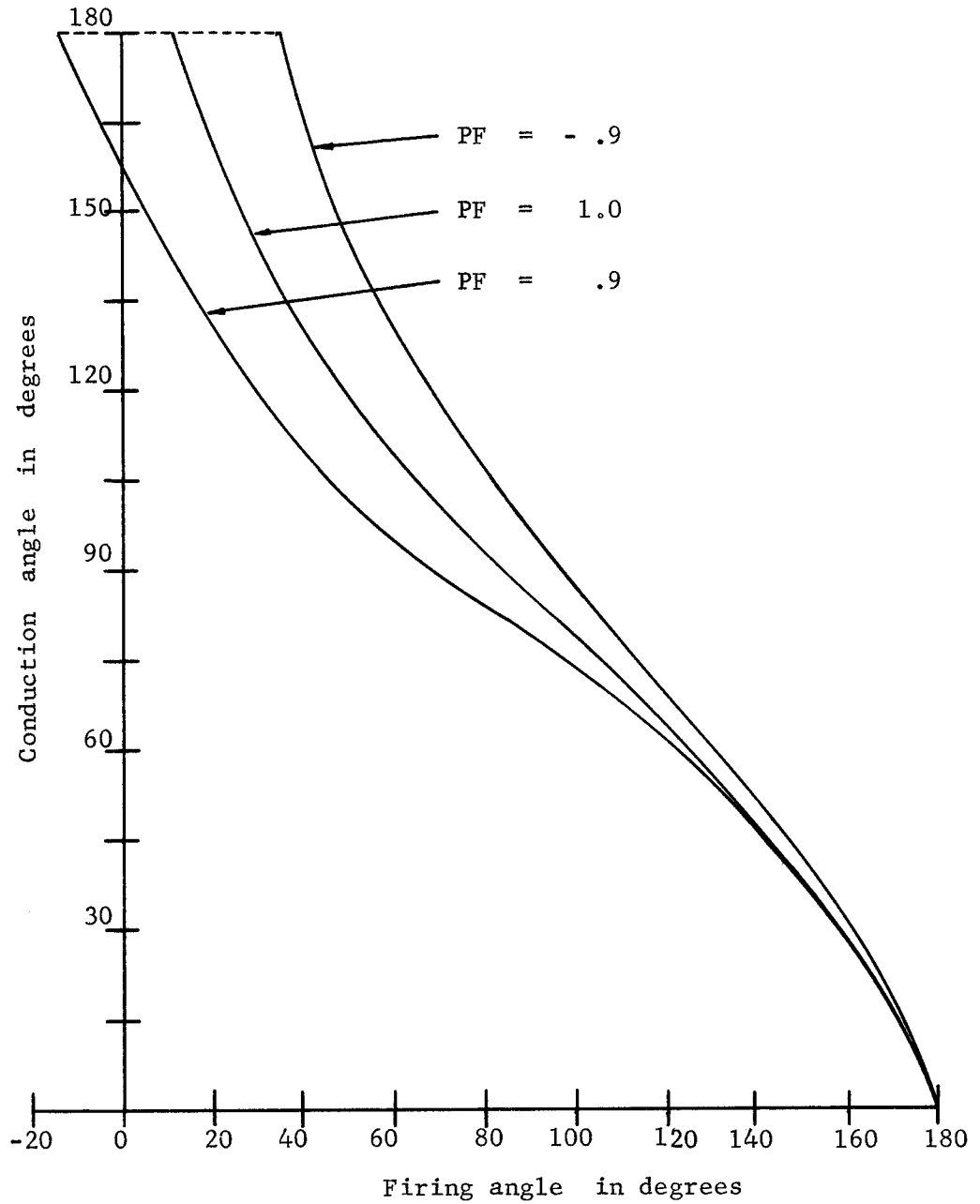
Fig. 19   Conduction angle vs. firing angle
for   Q = 2.0   and X_L =   .2
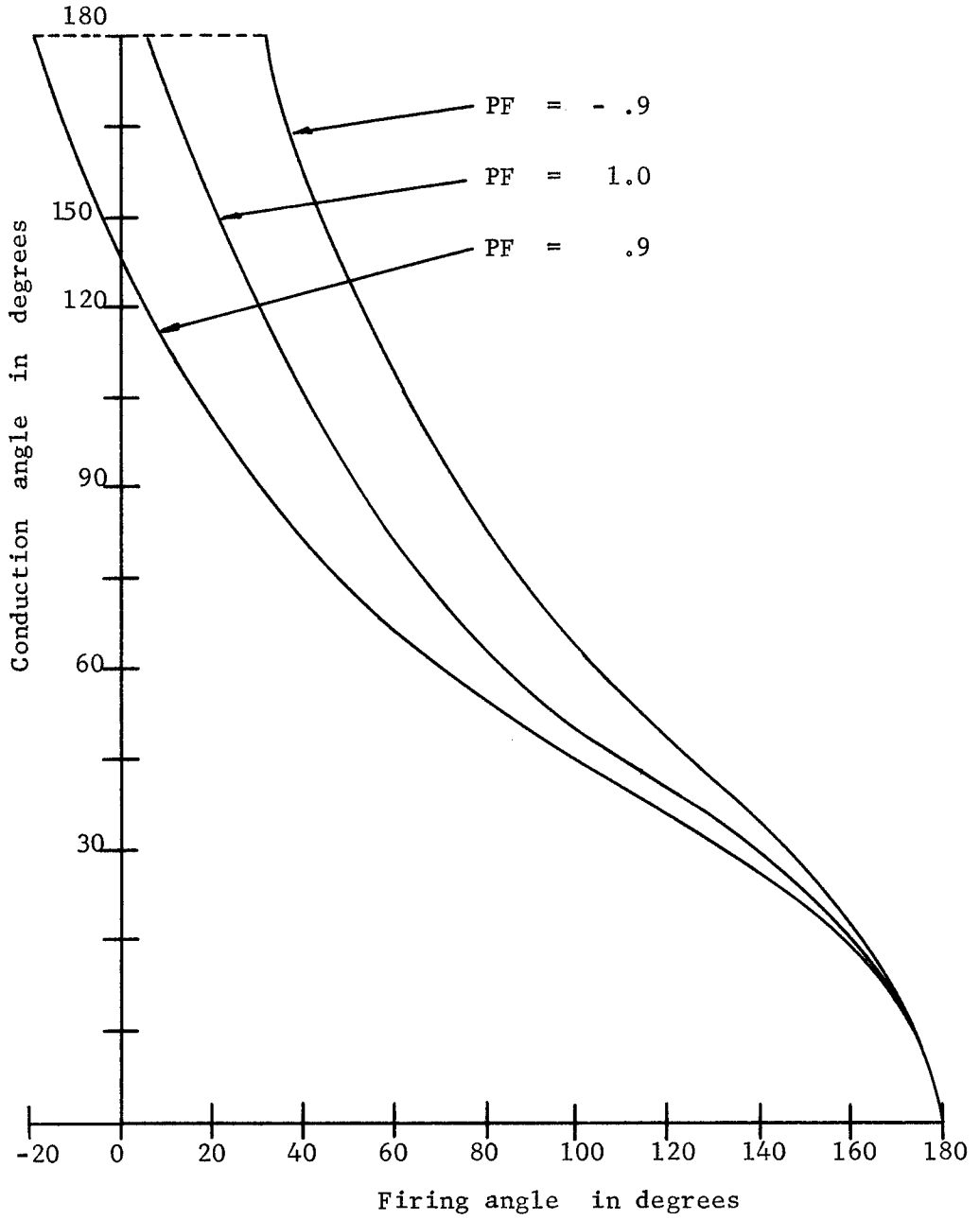
Fig. 20   Conduction angle vs. firing angle
for   Q = 5.0   and X_L =   .1

Fig. 21   Conduction angle vs. firing angle
for   Q = 5.0   and X_L =   .2

Fig. 22   Conduction angle vs. firing angle
for   Q = 10.0   and X_L =   .1

Fig. 23   Conduction angle vs. firing angle
for   Q = 10.0   and X_L =   .2

Power, Input Power Factor,
Rms Line Current and Load Voltage

Figs. 24 through 31 show curves of the average output power P,
input power factor PF_{in}, rms line current I_L and rms output voltage V_c
versus the firing angle ϕ for a load Q = 5.0. Figs. 32 through 39
show the same for a load Q = 10.0.

Examination of the plots permits the following observations to
be made:

1. All curves are a non-linear function of the firing angle.

2. For the same firing angle, all quantities decrease with X_L.

3. For inductive loads, all values decrease uniformly as the firing
   angle is increased.

4. For unity power factor loads, all values decrease in general
   after a slight increase as the firing angle is increased.

5. For leading power factor loads, all values decrease after a
   marked increase as the firing angle is increased.

6. The curves are independent of the value of Q.
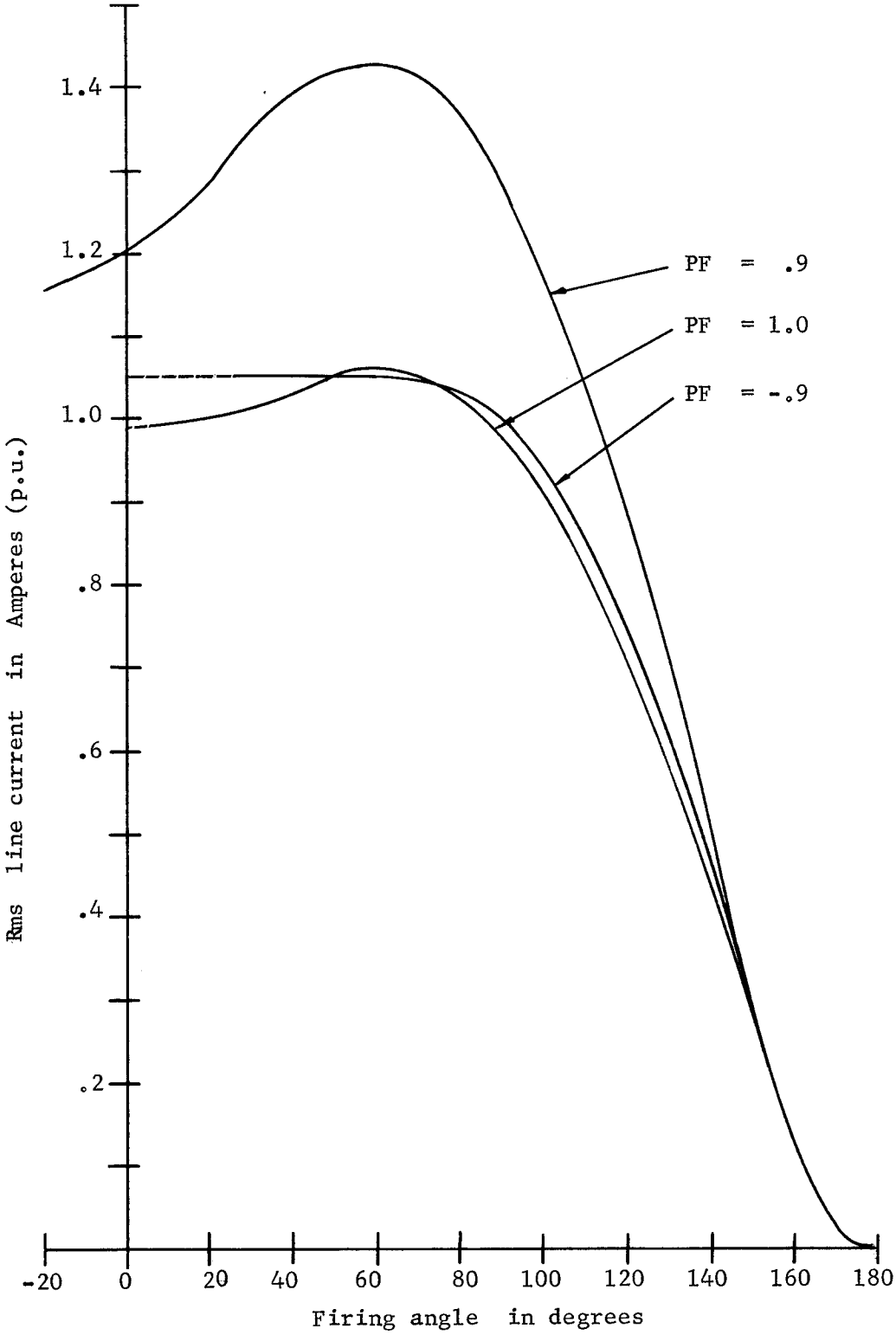
Fig.24   Rms line current vs. firing angle
          for   Q = 5.0   and X_L =   .1
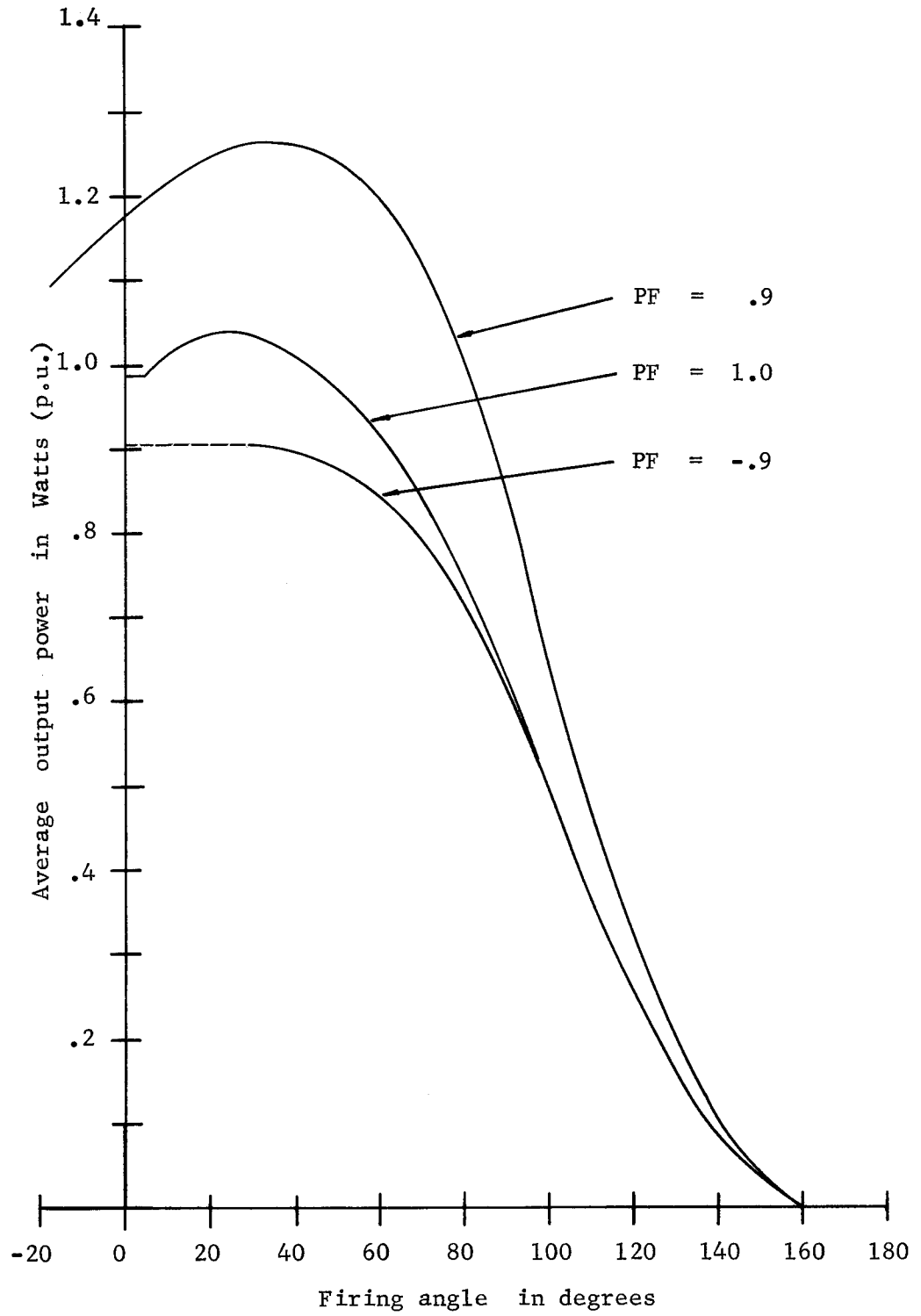
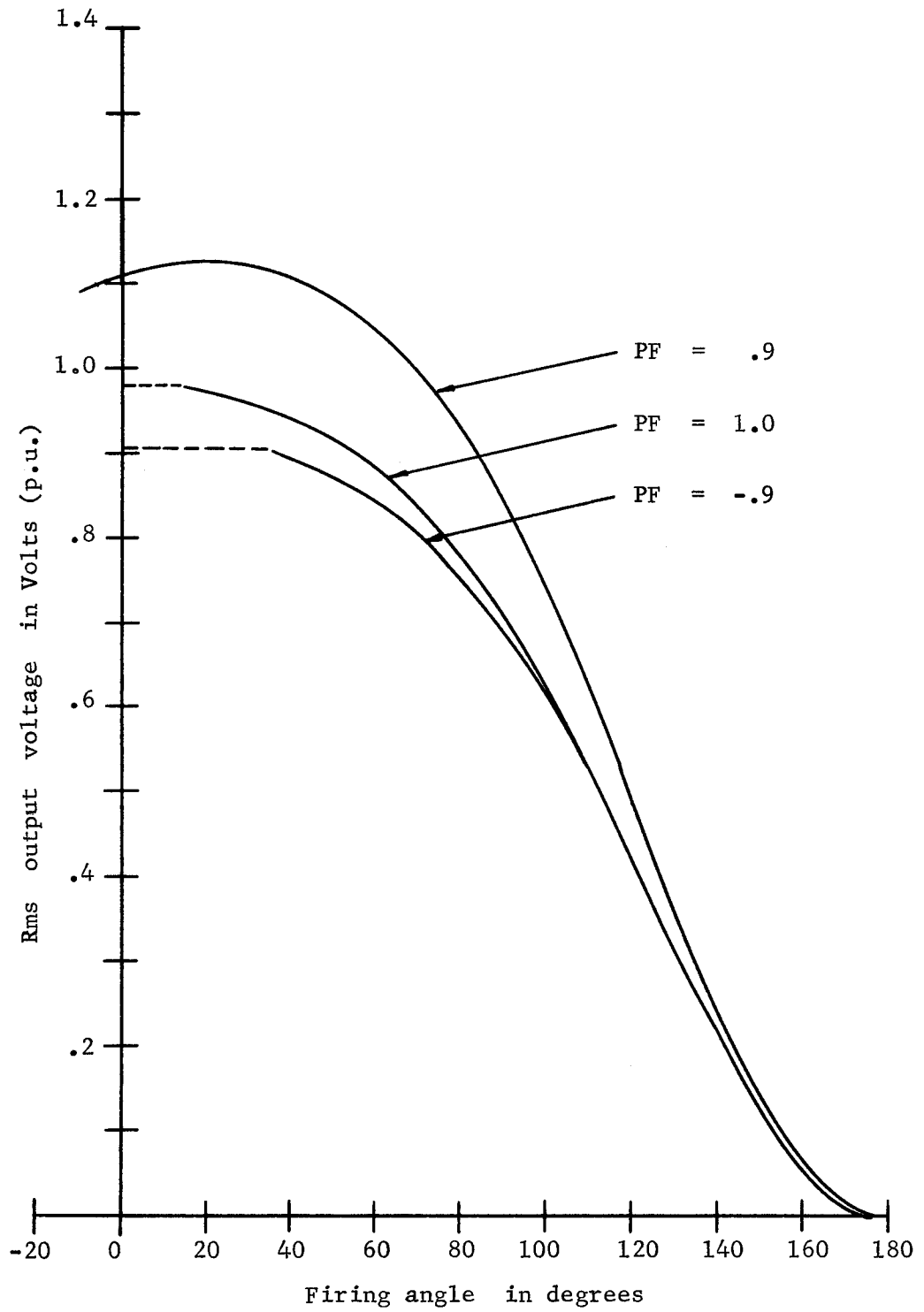Fig. 25   Average output power vs. firing angle
for   Q = 5.0   and X_L =   .1
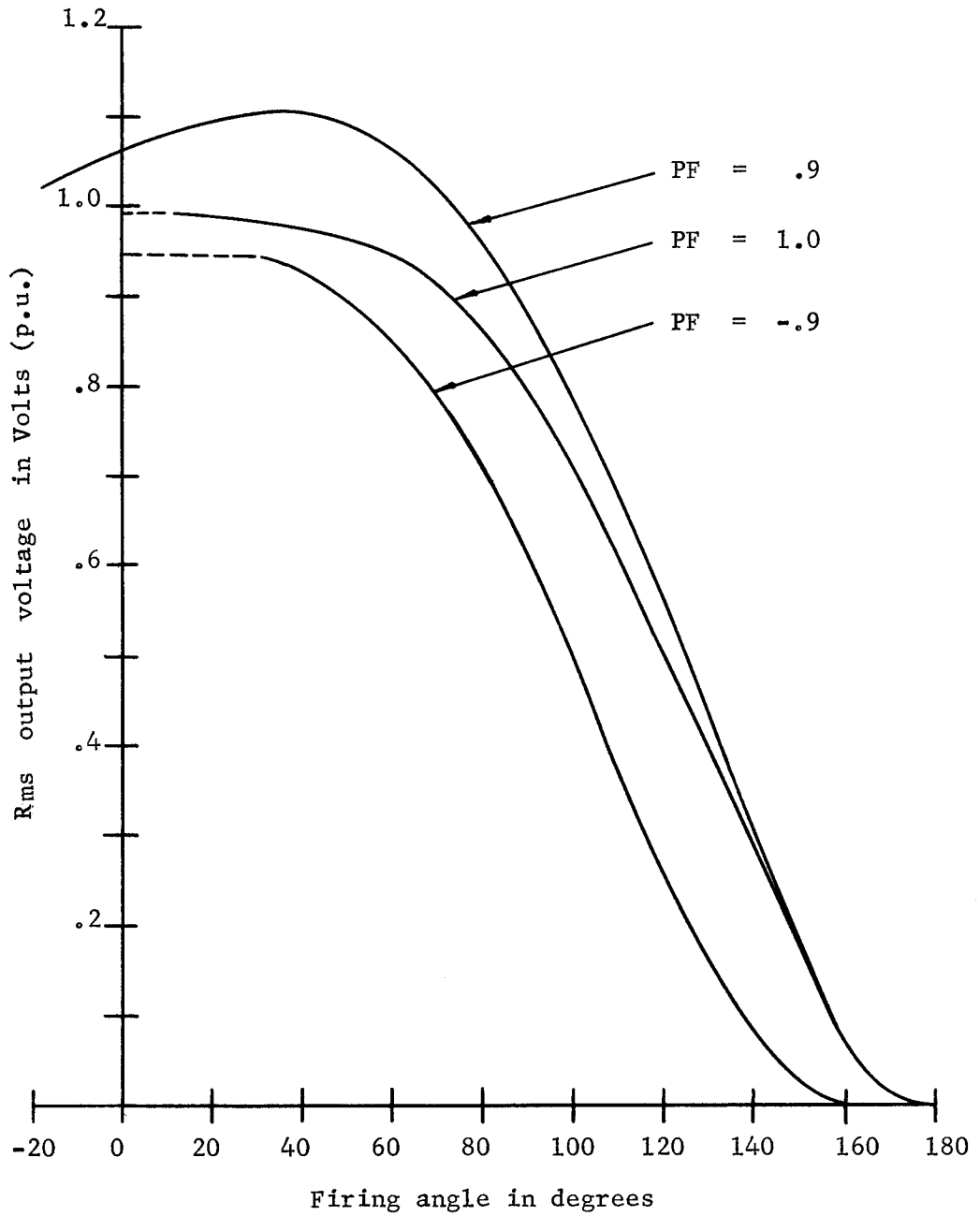
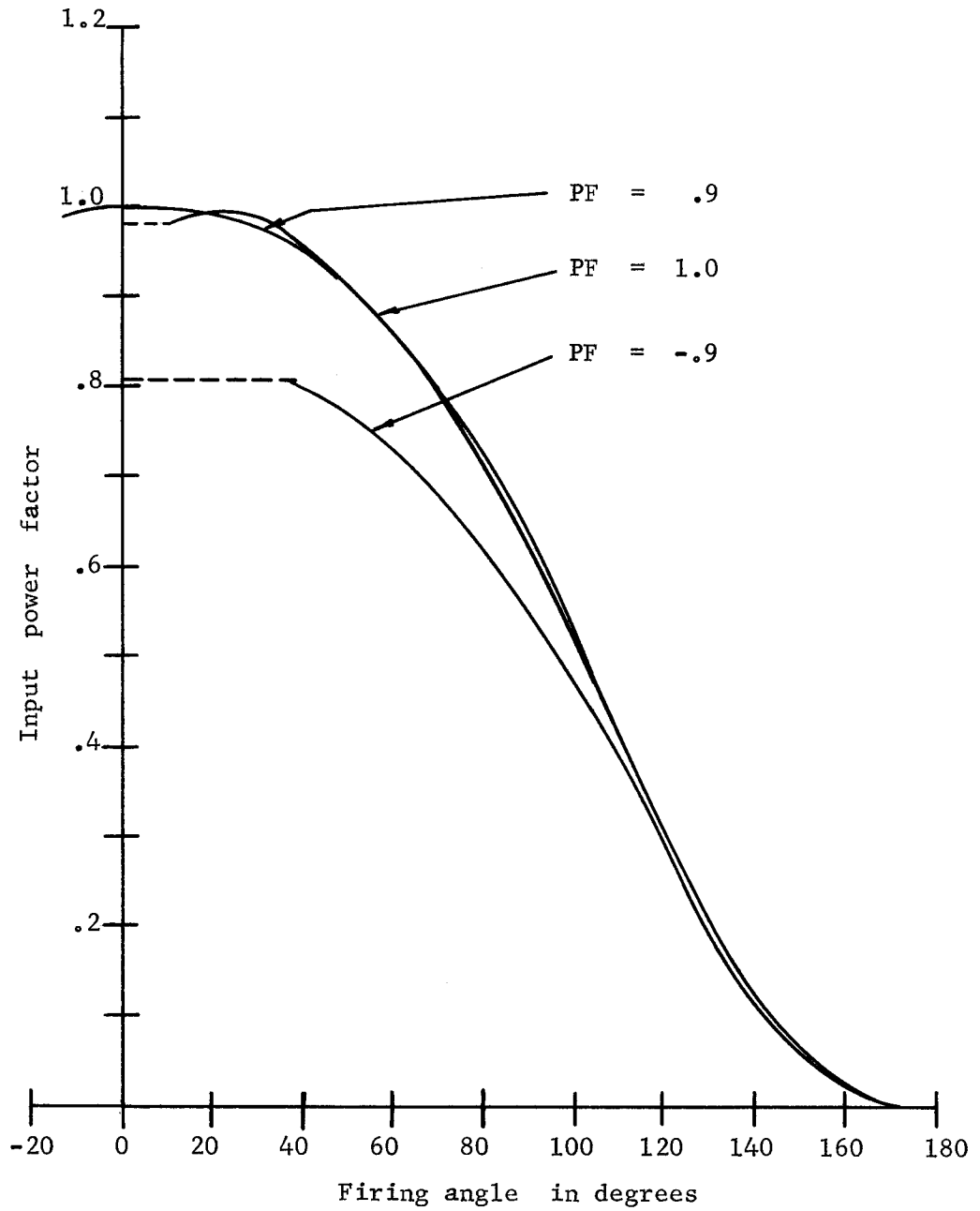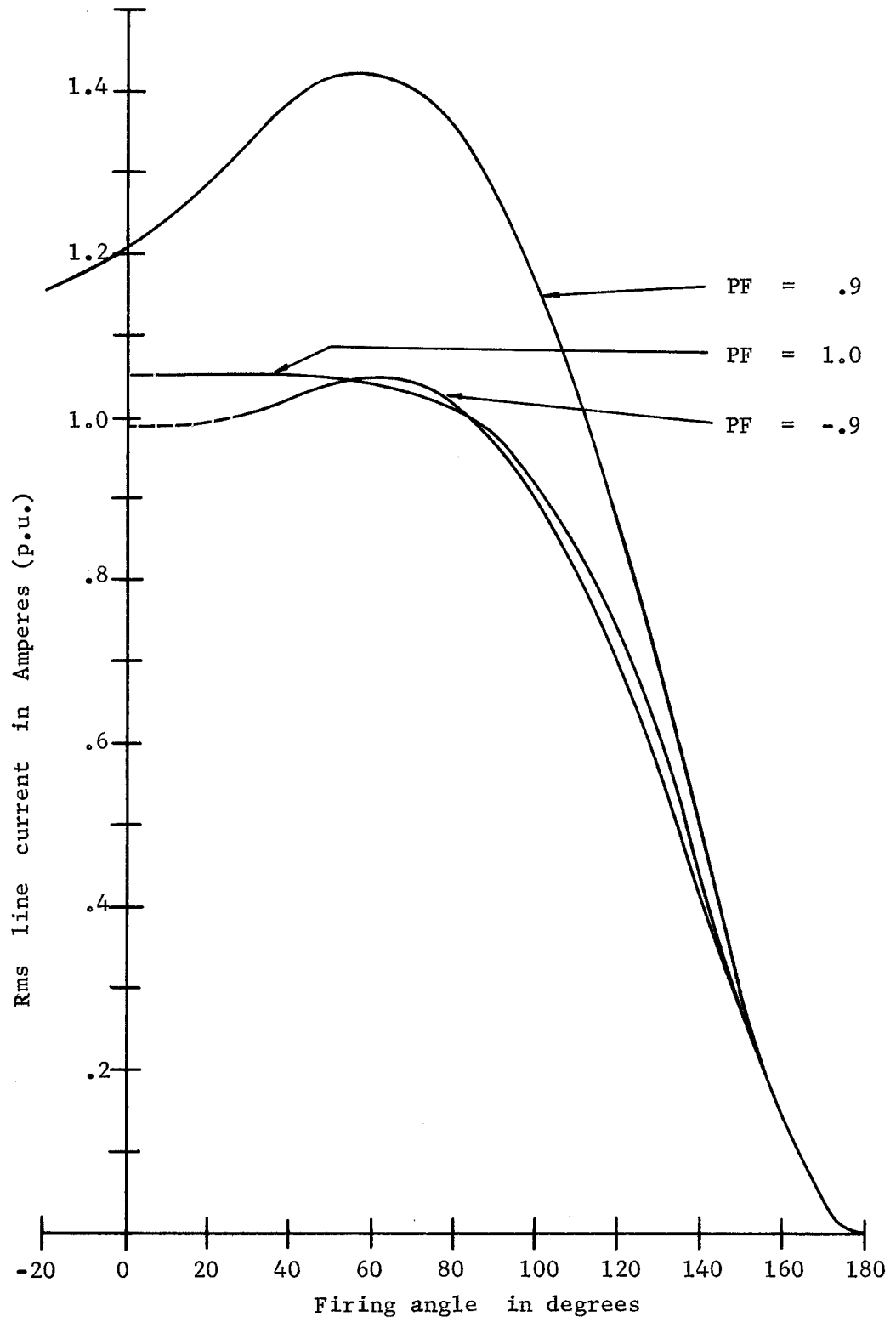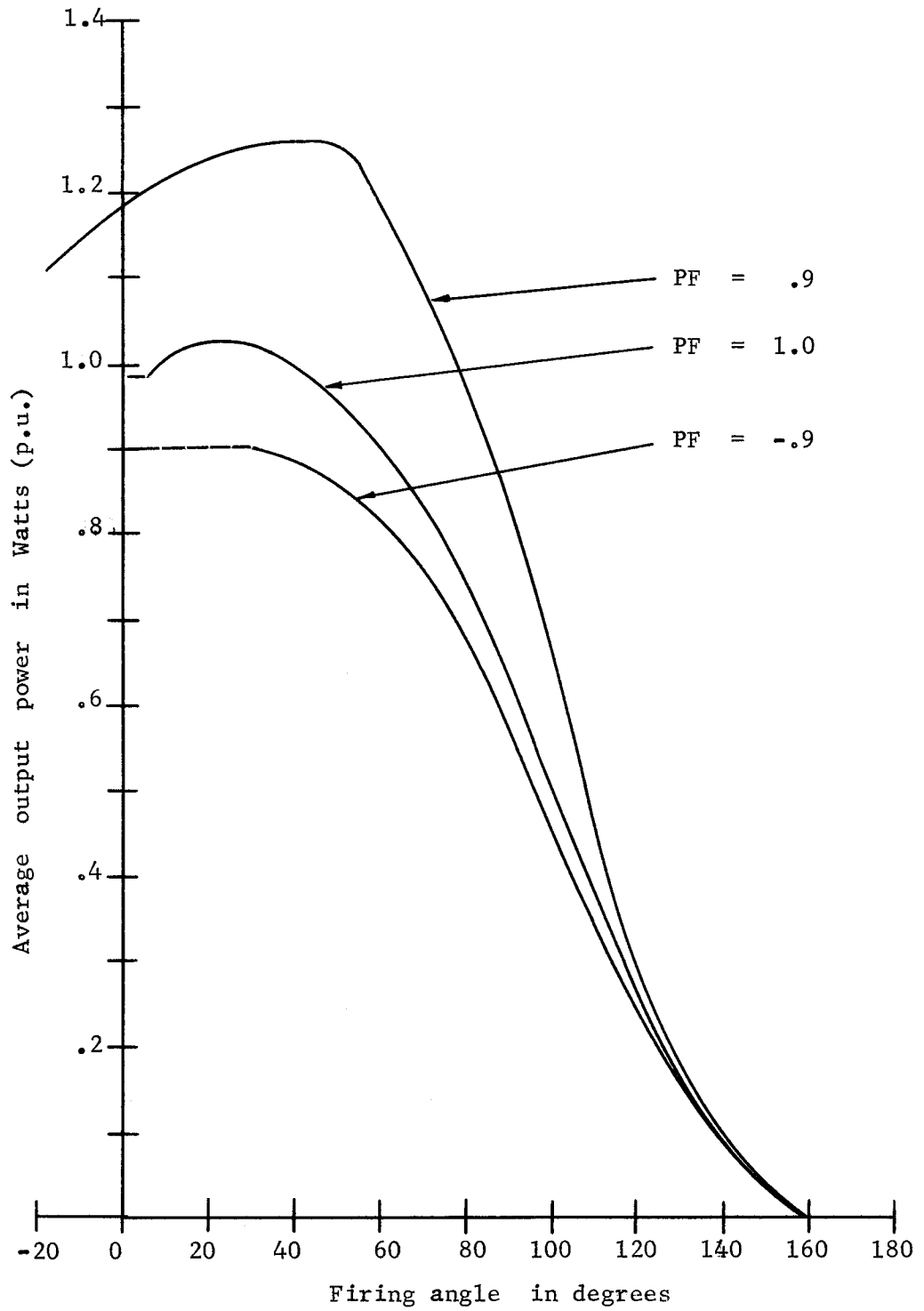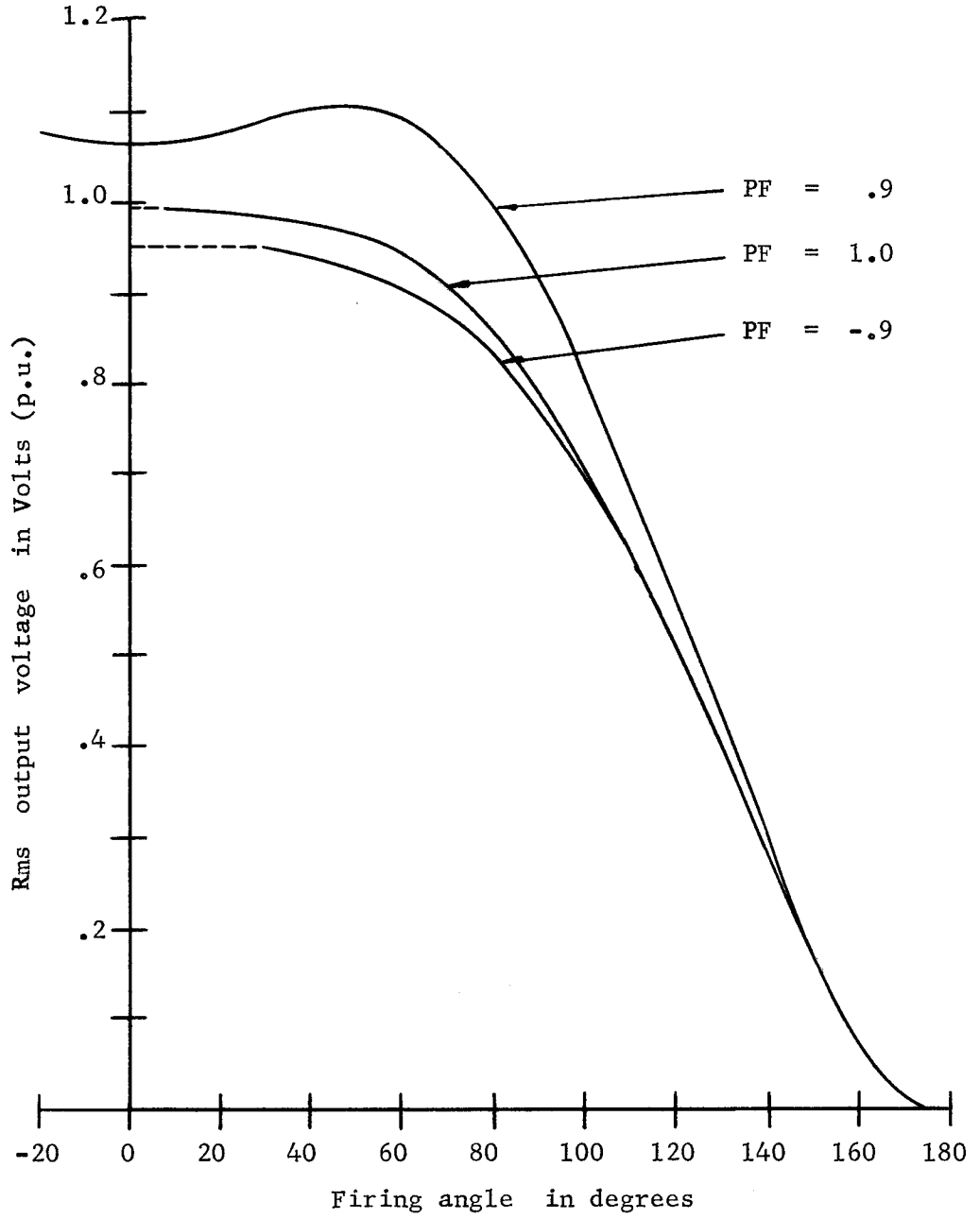Fig. 26   Rms output voltage vs. firing angle
for Q = 5.0   and X_L = .1
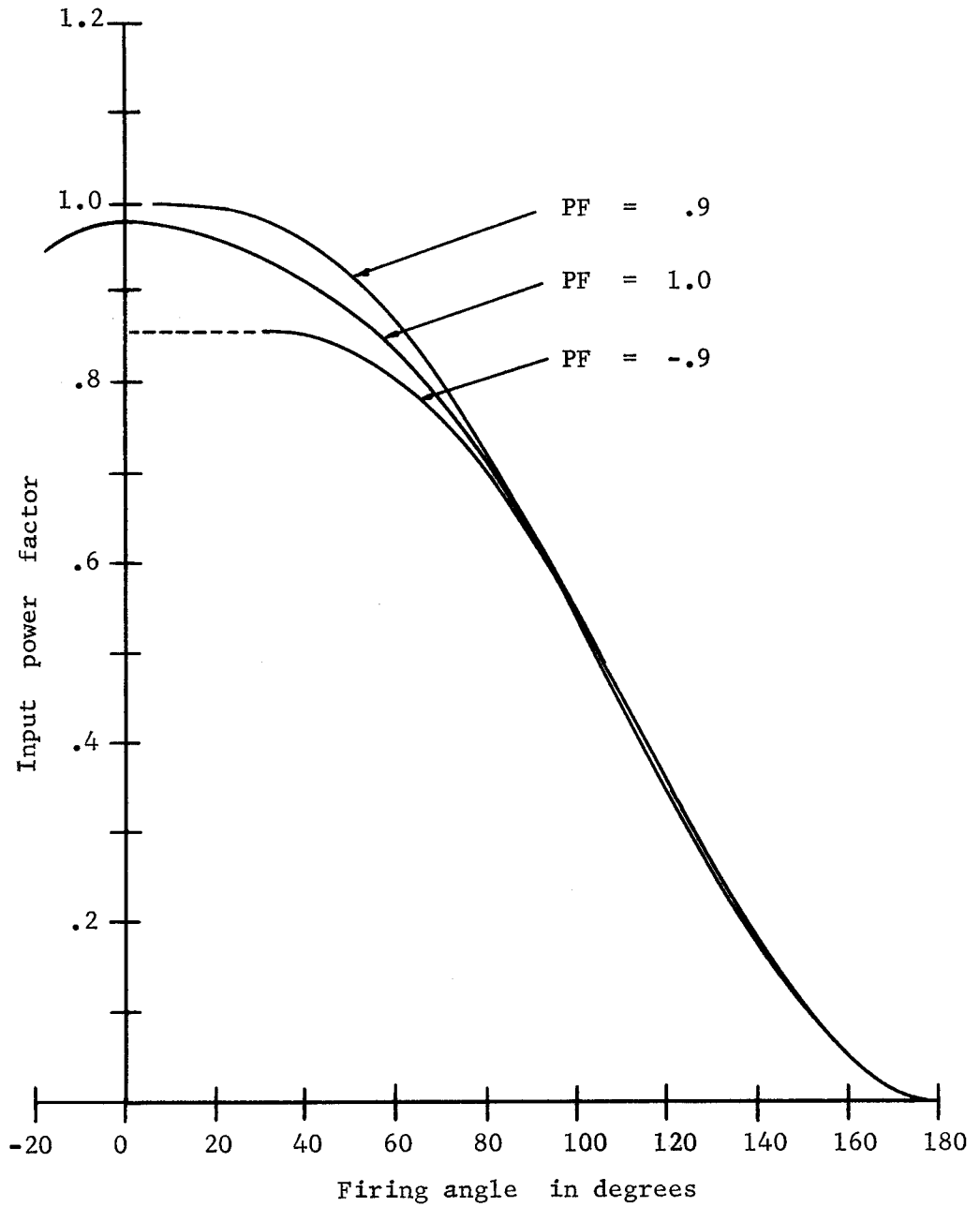
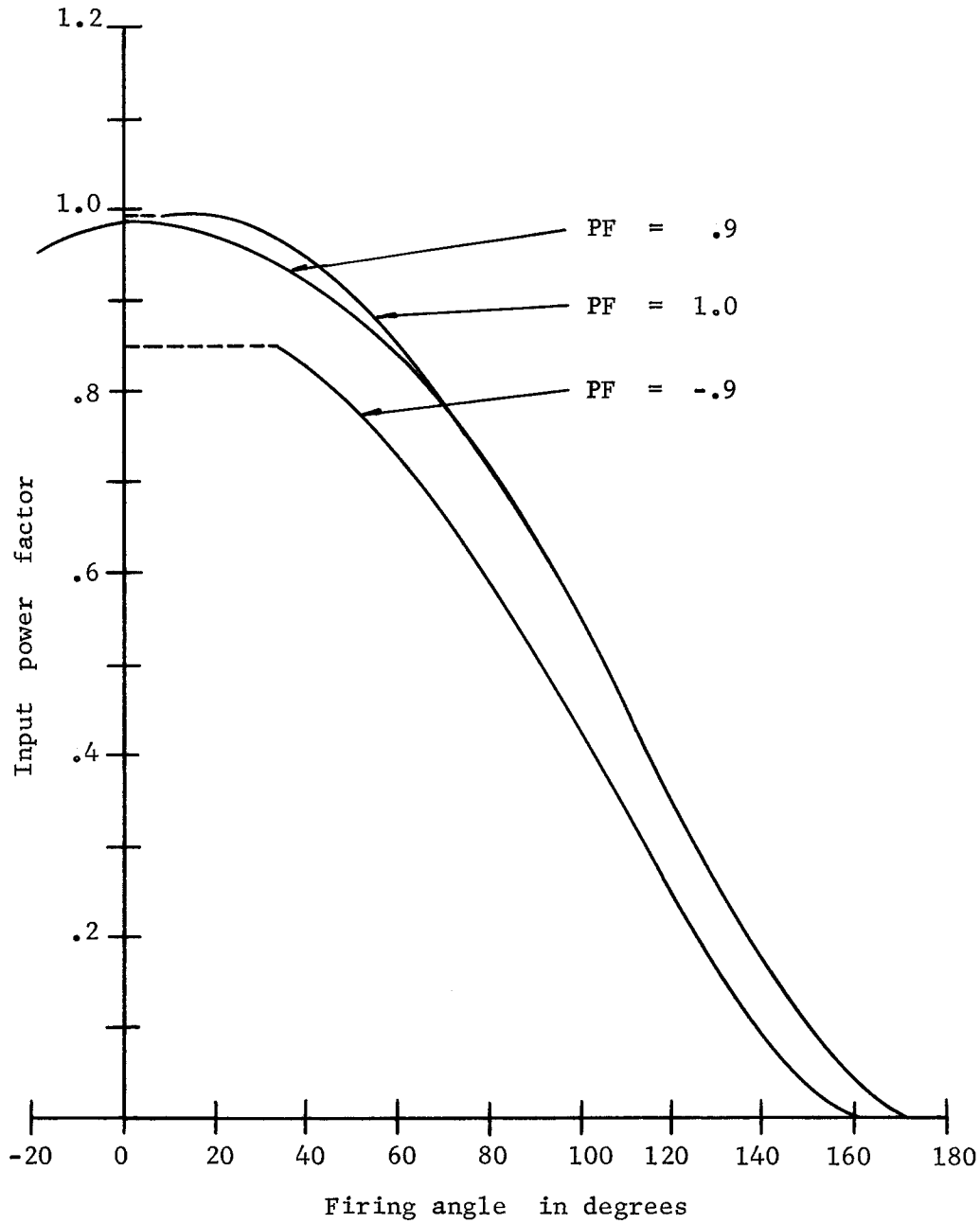Fig. 27   Input power factor vs. firing angle
for   Q = 5.0   and X_L =   .1
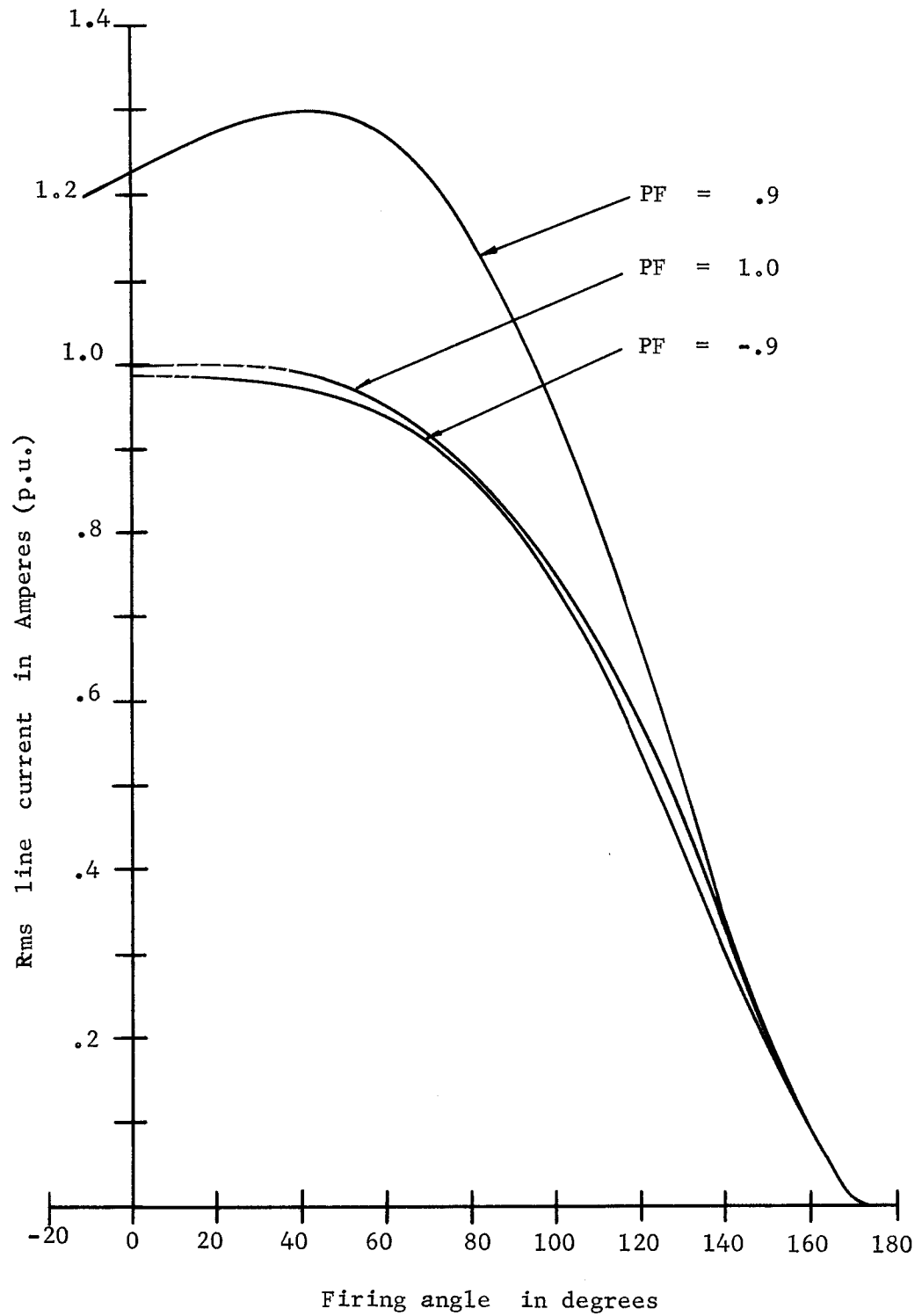
Fig. 28   Rms line current vs. firing angle
for   Q = 5.0   and X_L =   .2
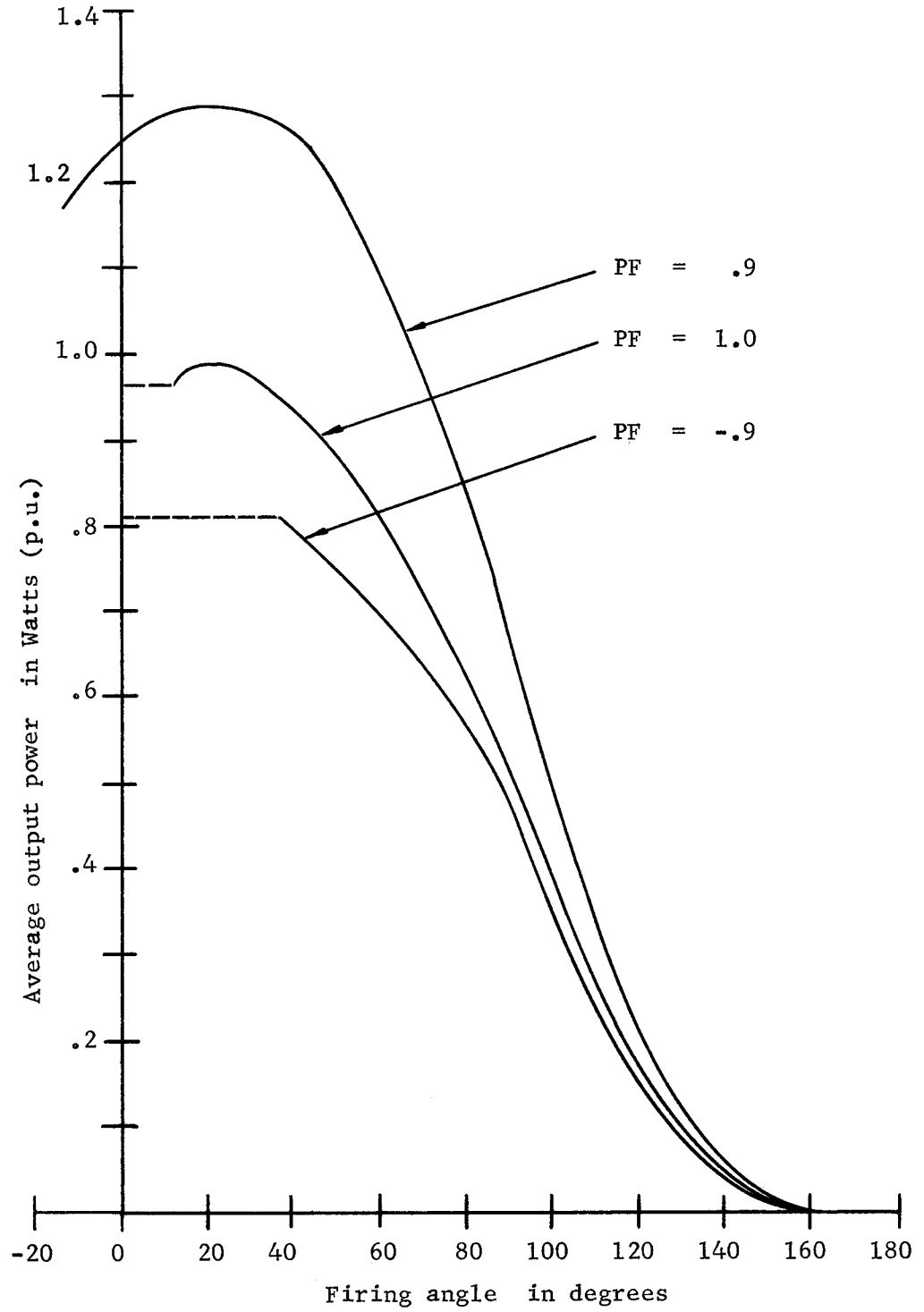
Fig. 29   Average output power vs. firing angle
for Q = 5.0 and X_L = .2

Fig. 30   Rms output voltage vs. firing angle
for $Q = 5.0$ and $X_L = .2$

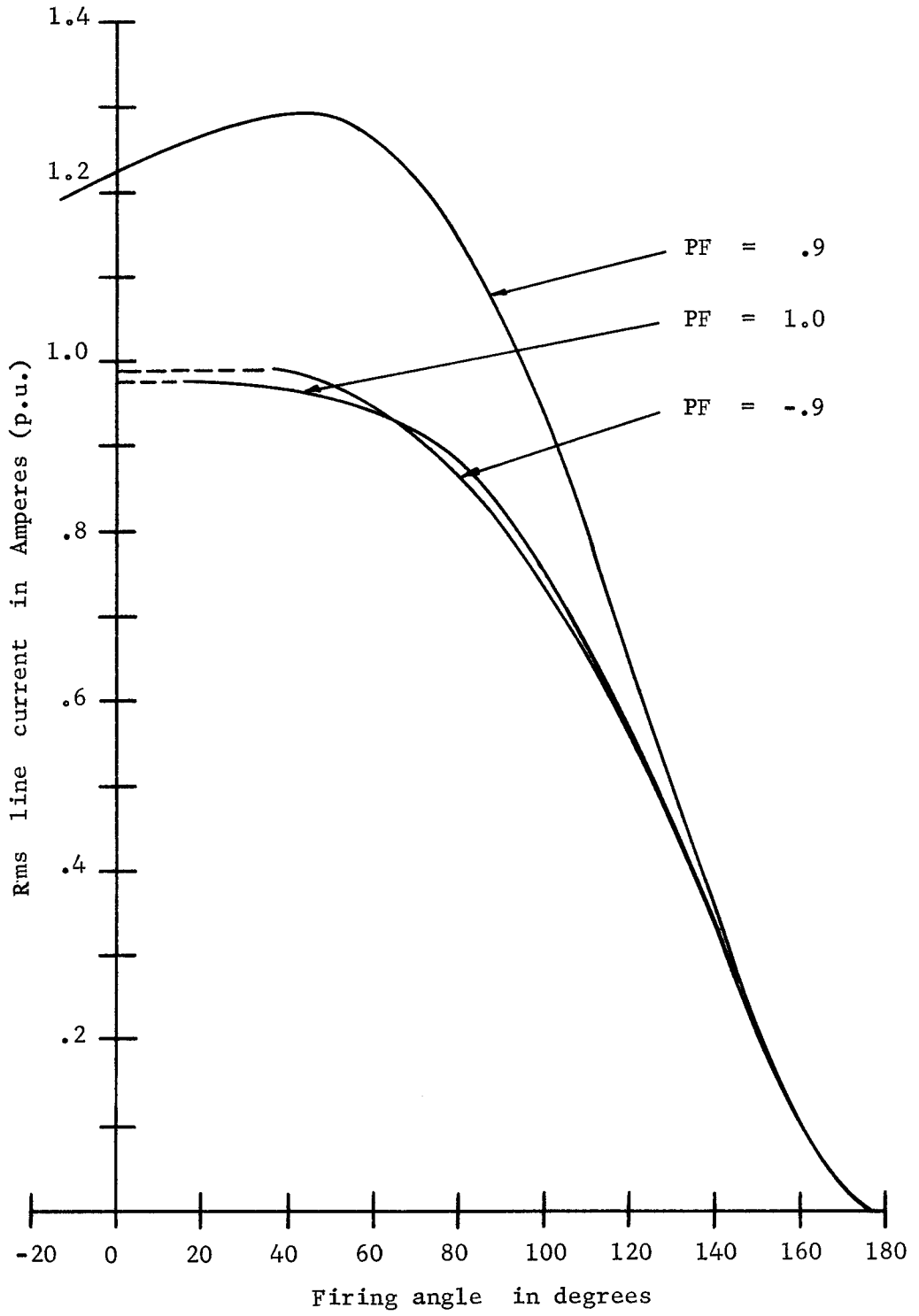Fig. 31   Input power factor vs. firing angle
for   Q = 5.0   and X_L =   .2

Fig. 32   Rms line current vs. firing angle
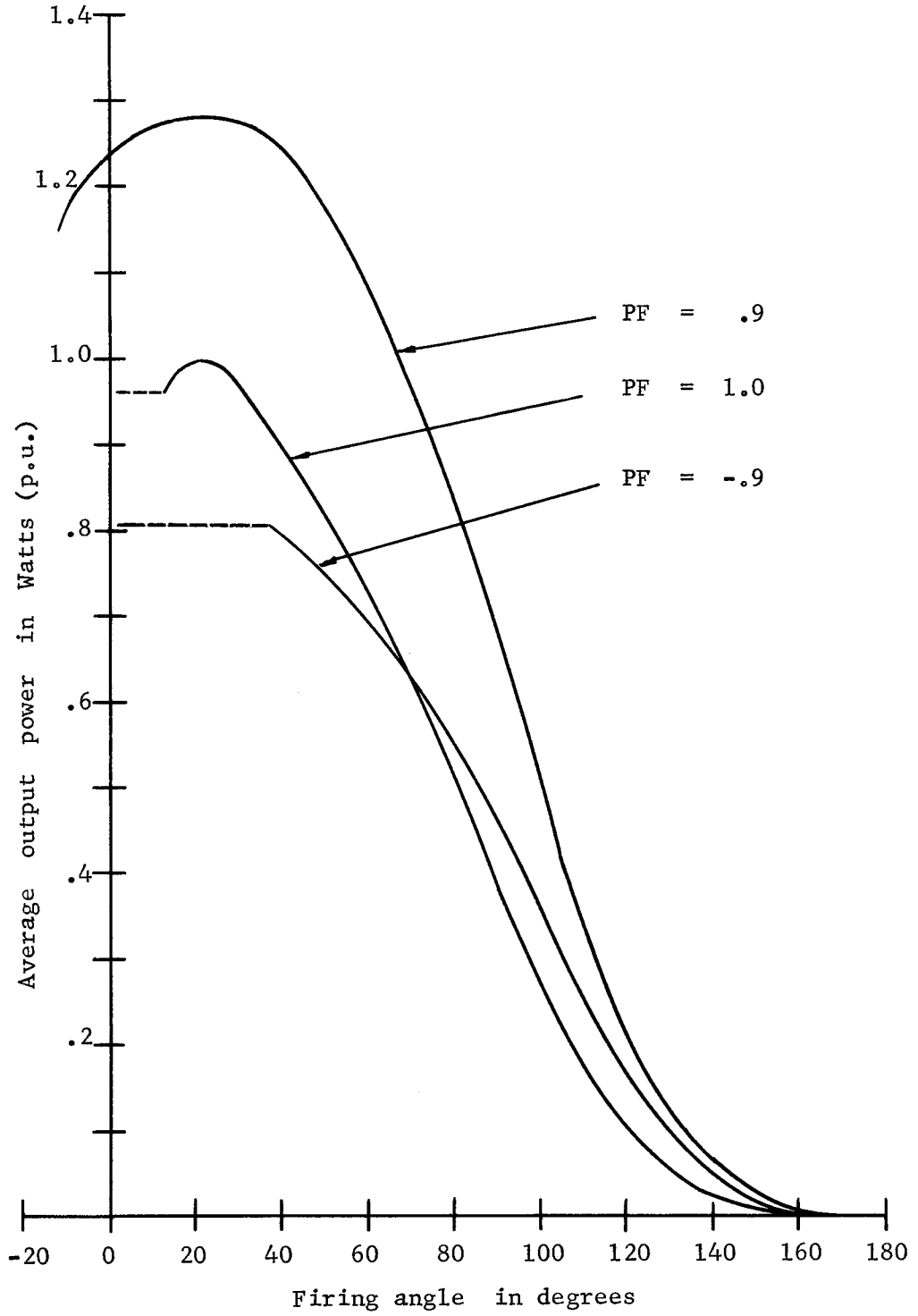for   Q = 10.0   and X_L = .1

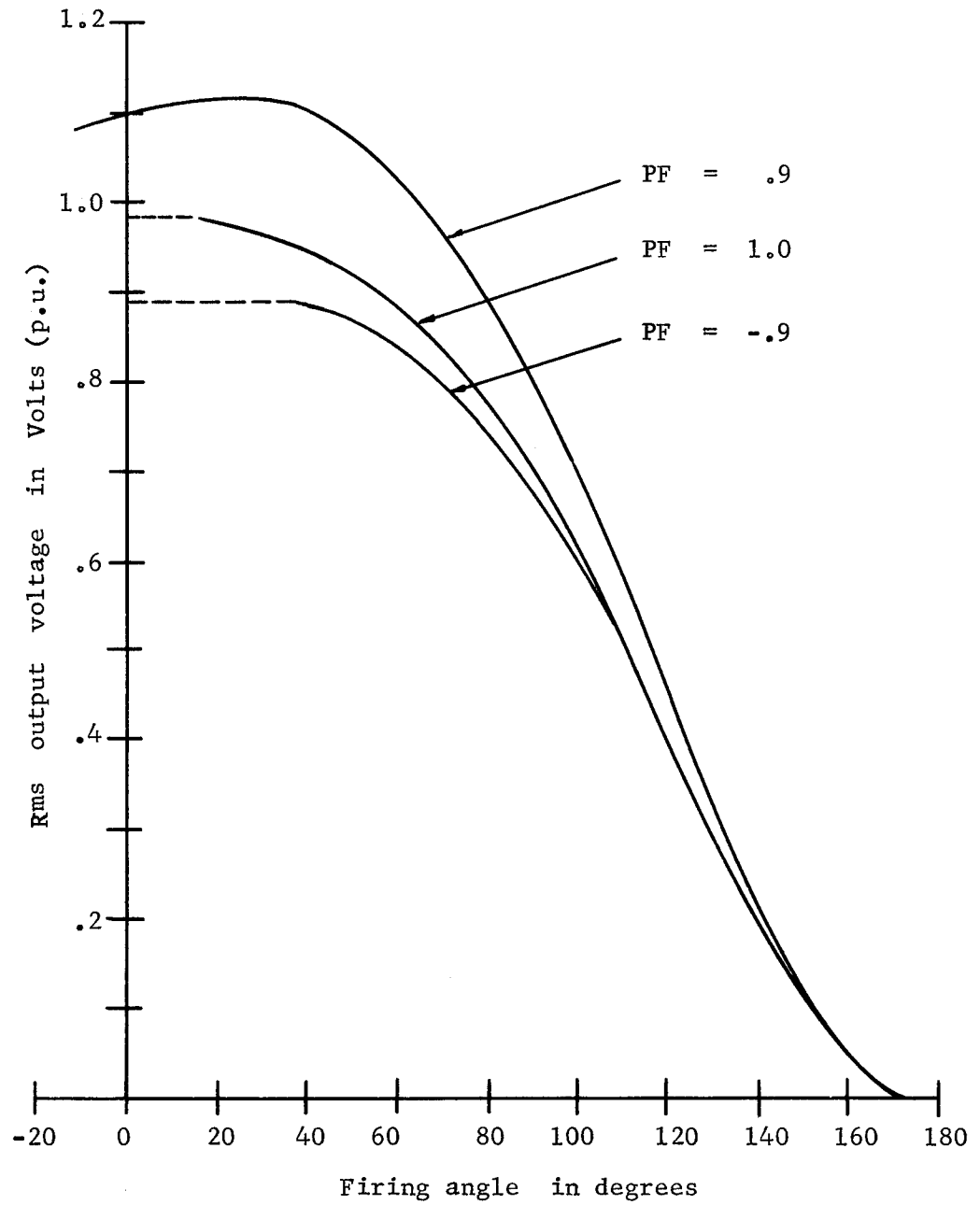Fig. 33 Average output power vs. firing angle
for Q = 10.0 and X_L = .1

Fig. 34   Rms output voltage vs. firing angle
for   Q = 10.0   and X_L =   .1

Fig. 35   Input power factor vs. firing angle
for Q = 10.0 and X_L = .1

Fig. 36   Rms line current vs. firing angle
           for Q = 10.0 and X_L = .2

Fig. 37   Average output power vs. firing angle
for Q = 10.0   and X_L =   .2

Fig. 38   Rms output voltage vs. firing angle
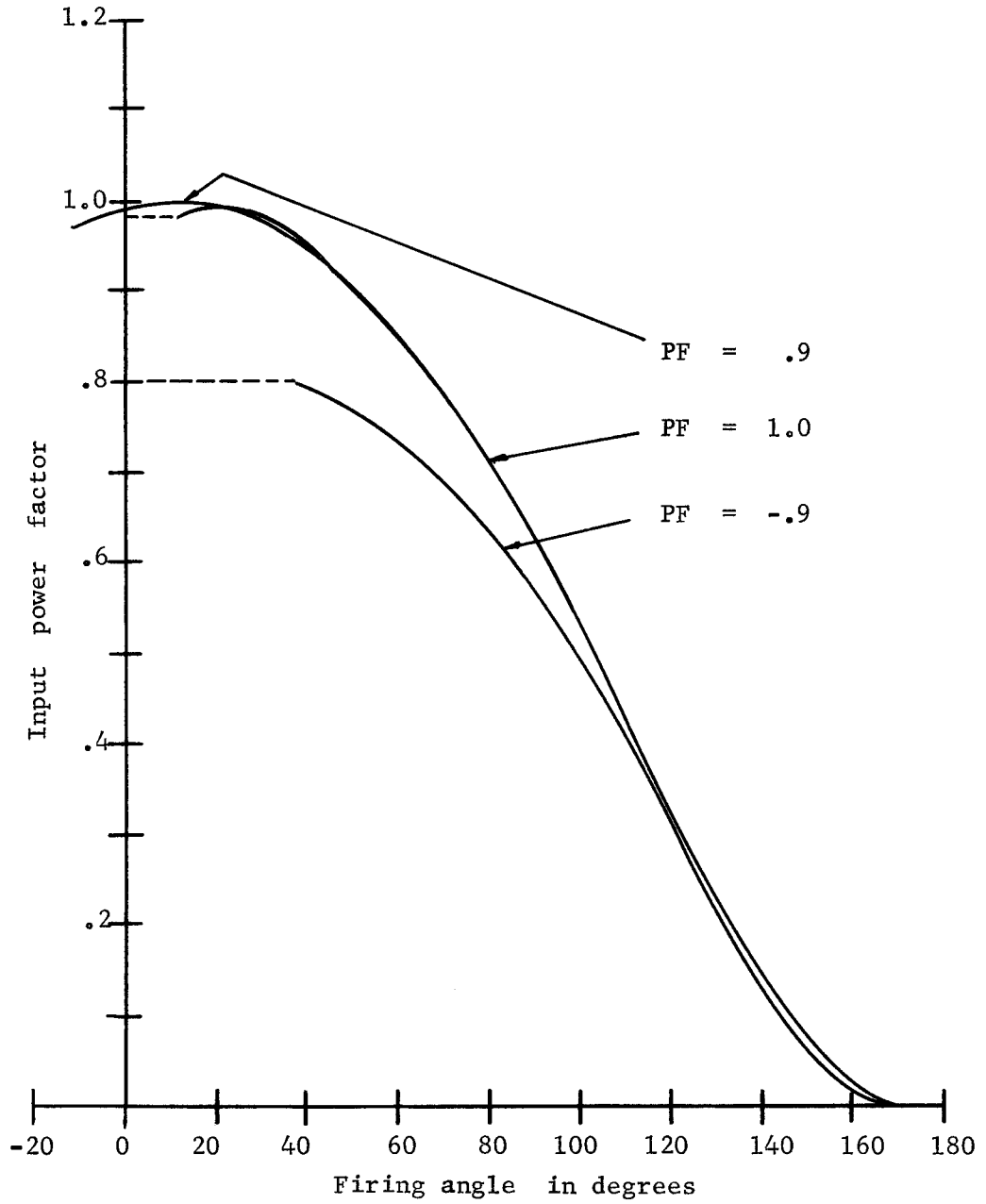for   Q = 10.0   and X_L =   .2

Fig. 39   Input power factor vs. firing angle
for Q = 10.0 and X_L = .2

Line Current Harmonics

Figs. 40 through 47 show the rms harmonic content of the line current i_L as a function of the firing angle. From the above mentioned figures, the following observations can be made:

1. The fundamental component of i_L for lagging and unity power factor loads decreases as the firing angle is increased.

2. The fundamental component of i_L for leading power factor loads increases slightly before decreasing as the firing angle is increased.

3. The maximum rms value of the higher harmonics decreases with X_L.

4. The third harmonic component of i_L is the dominant harmonic in all cases.

5. The leading power factor loads have higher harmonic content.

6. The pulse nature of the line current at high firing angles is implied by the nearly equal magnitudes of the harmonic components.

7. The third, fifth and seventh harmonic components have one, two and three peaks, respectively.

8. The second peak of the fifth and the third peak of the seventh harmonic are the largest for each harmonic.
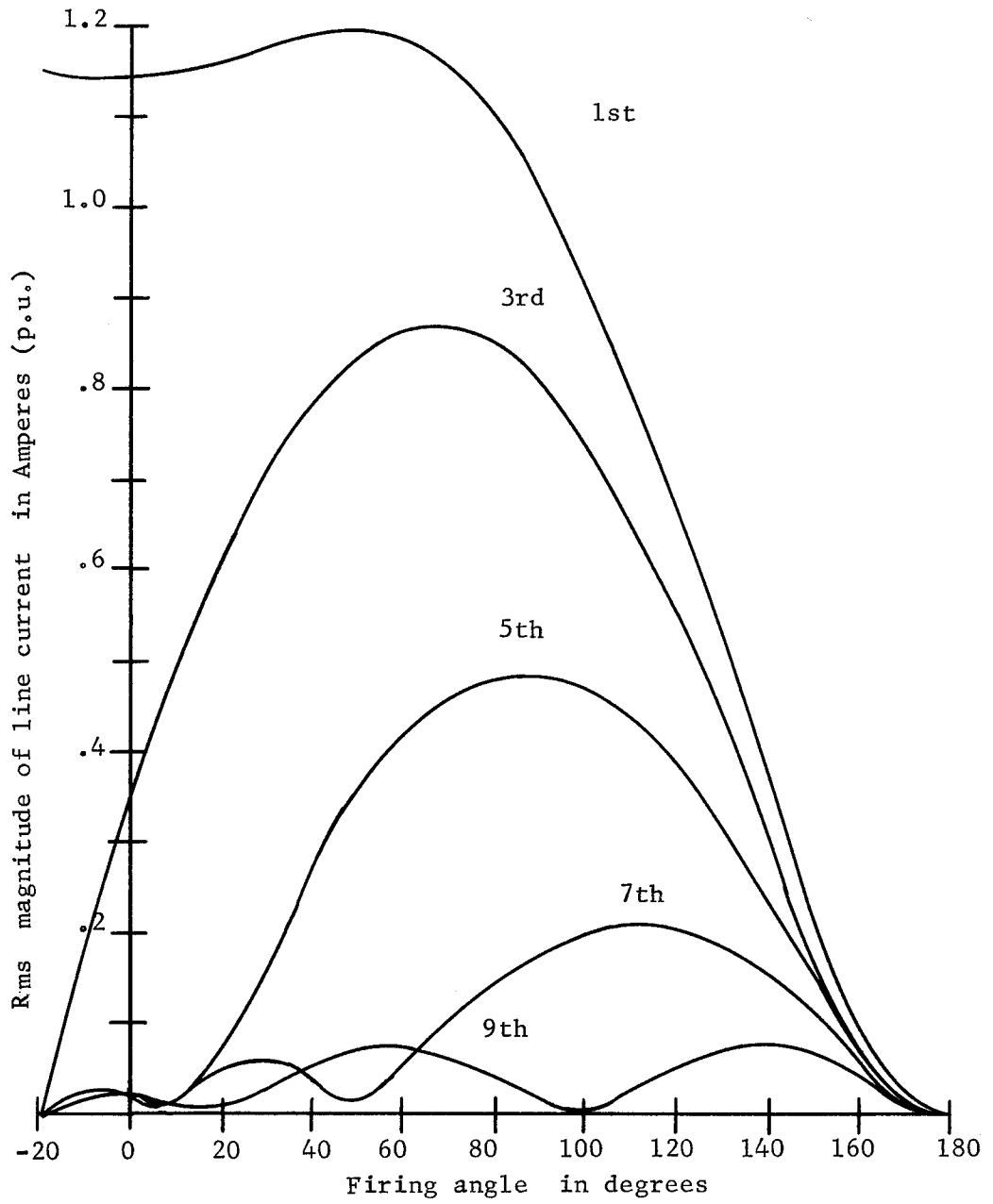
Fig. 40   Line current harmonics vs. firing angle
for   Q = 1.0, X_L = .1   and   PF = .9
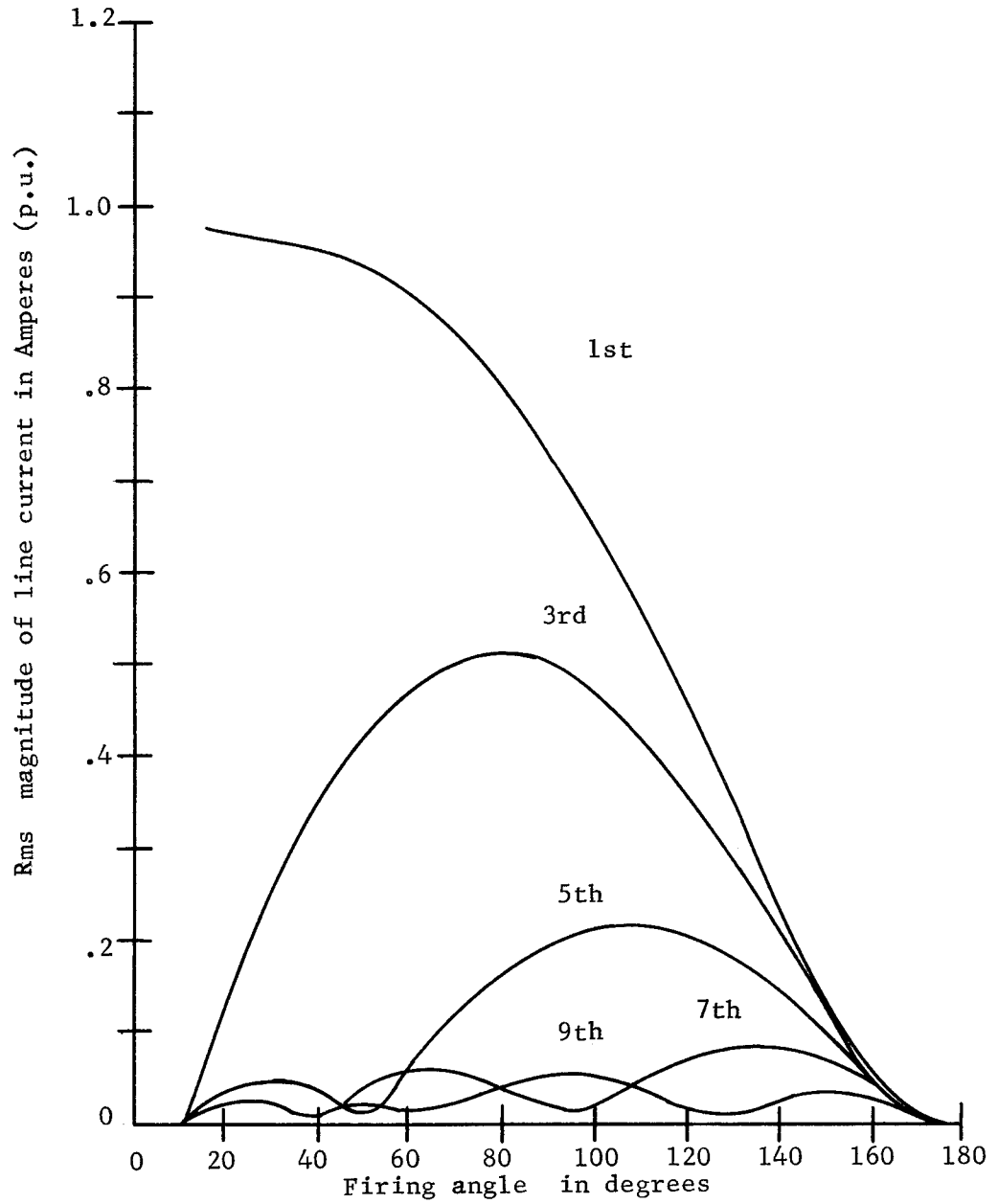
Fig. 41   Line current harmonics vs. firing angle
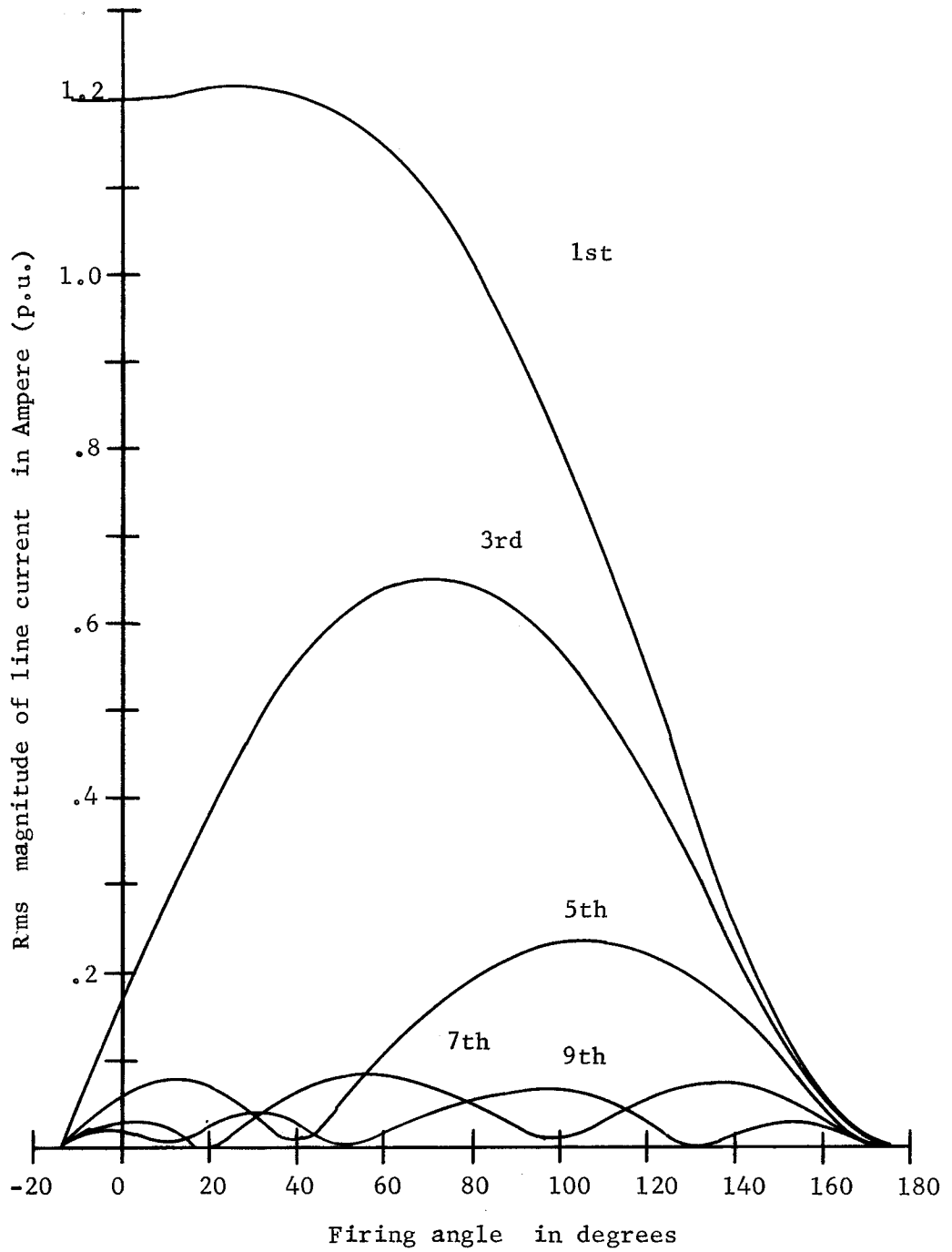for   Q = 1.0, X_L = .2   and   PF = 1.0

Fig. 42   Line current harmonics vs. firing angle
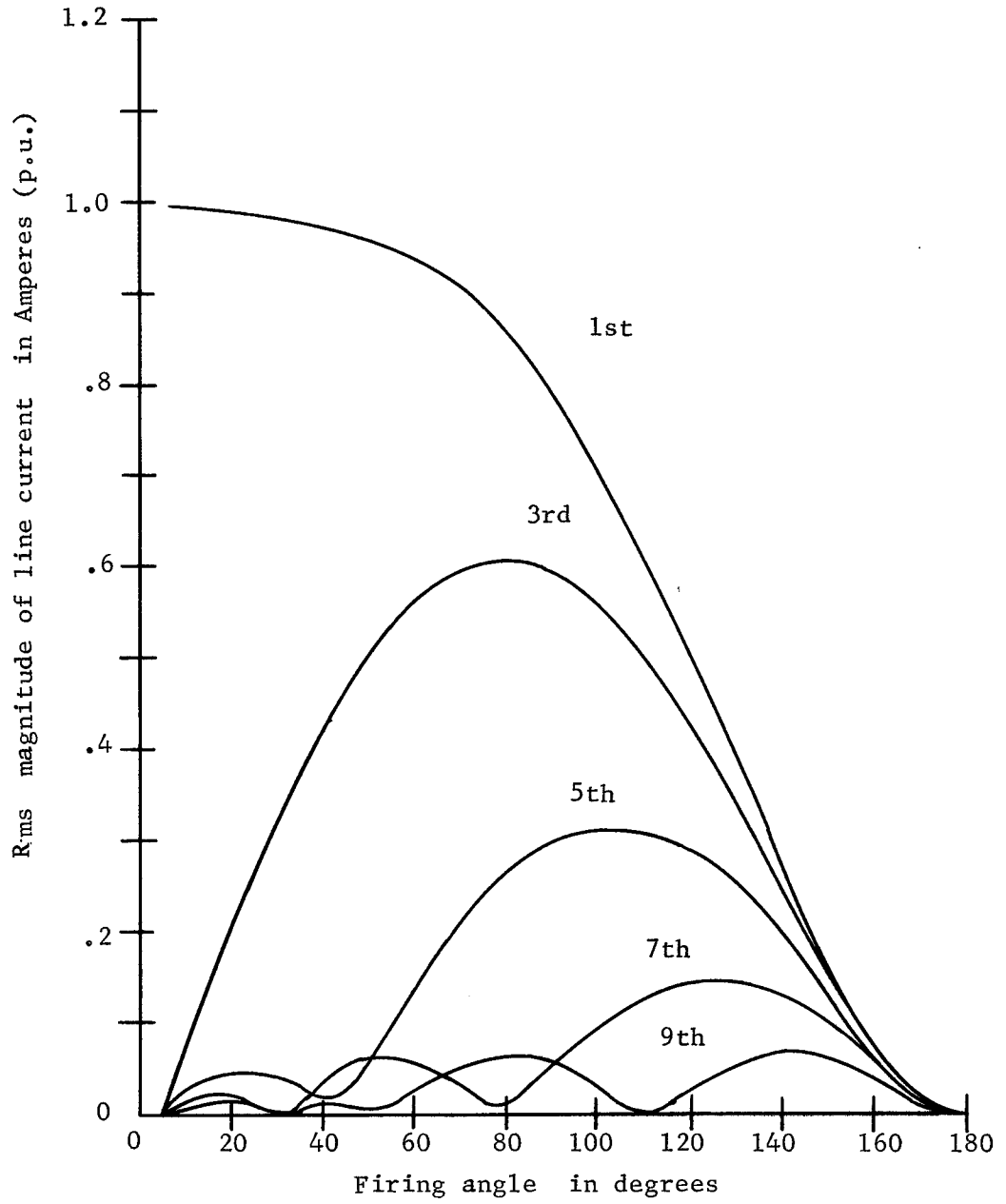for   Q = 1.0, X_L = .2   and   PF = .9

Fig.43   Line current harmonics vs. firing angle
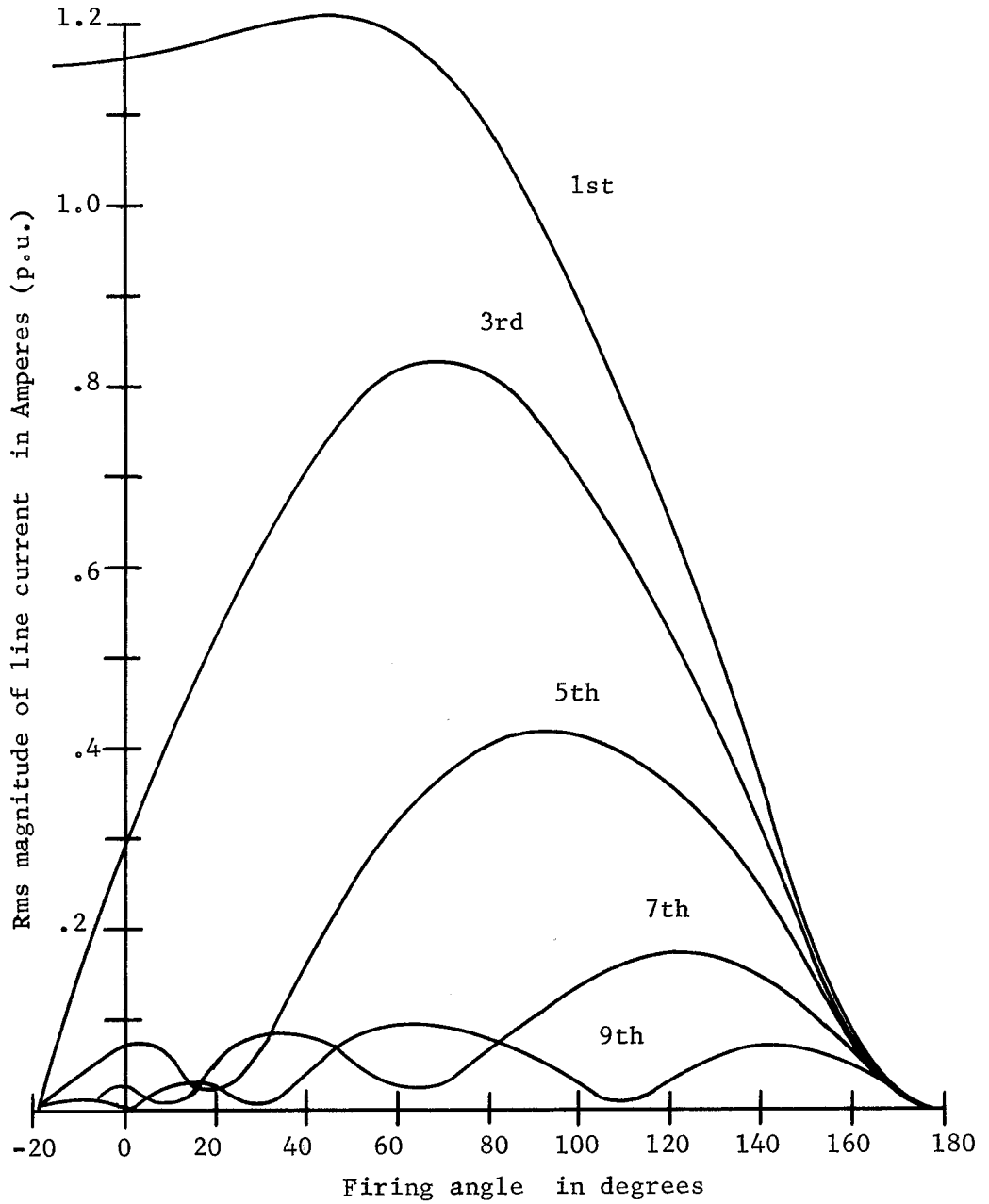   for   Q = 2.0, X_L = .1   and   PF = 1.0

Fig. 44   Line current harmonics vs. firing angle
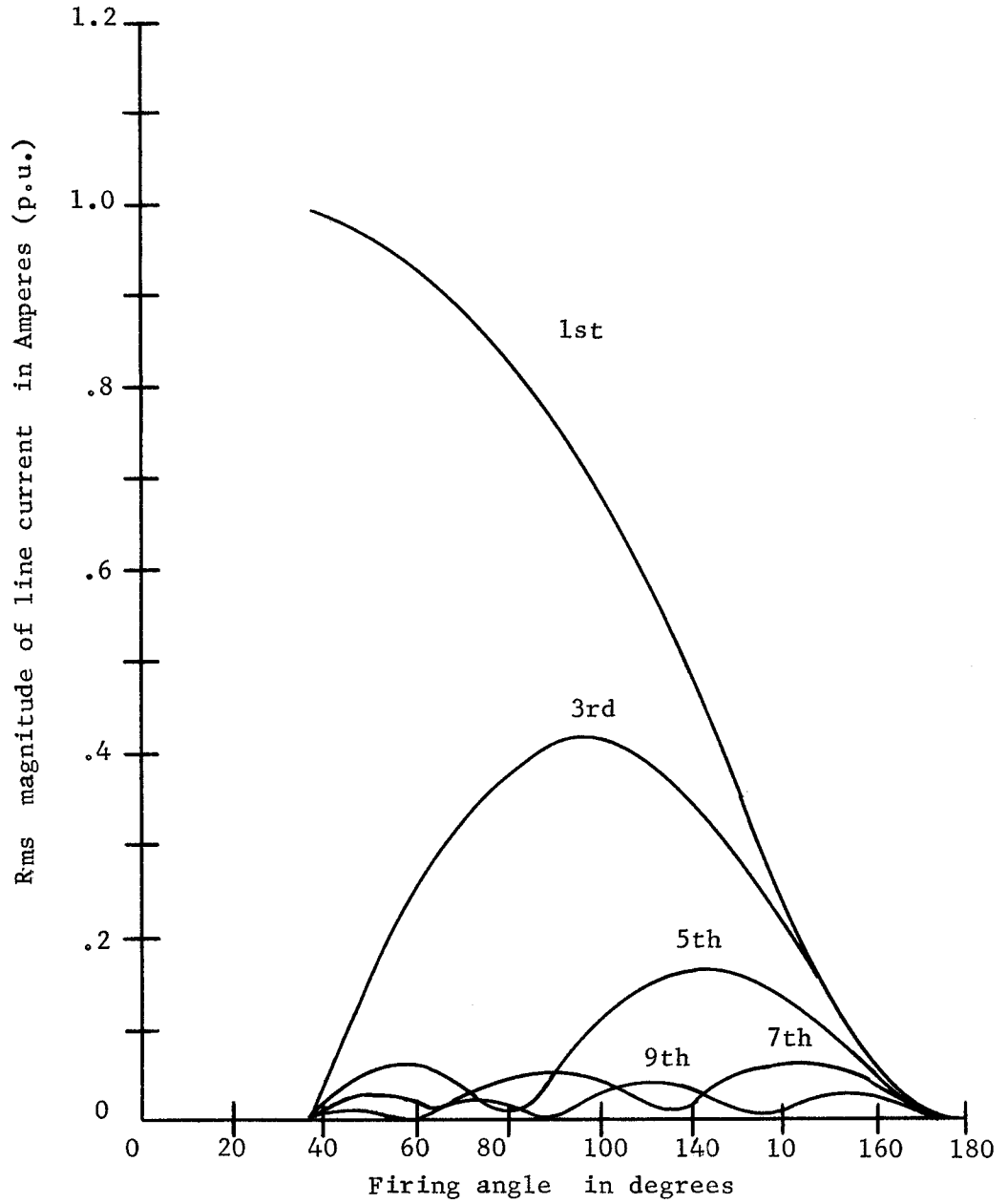for   Q = 2.0, X_L = .1   and   PF = .9

Fig. 45   Line current harmonics vs. firing angle
for   Q = 2.0, X_L = .2   and   PF = -.9
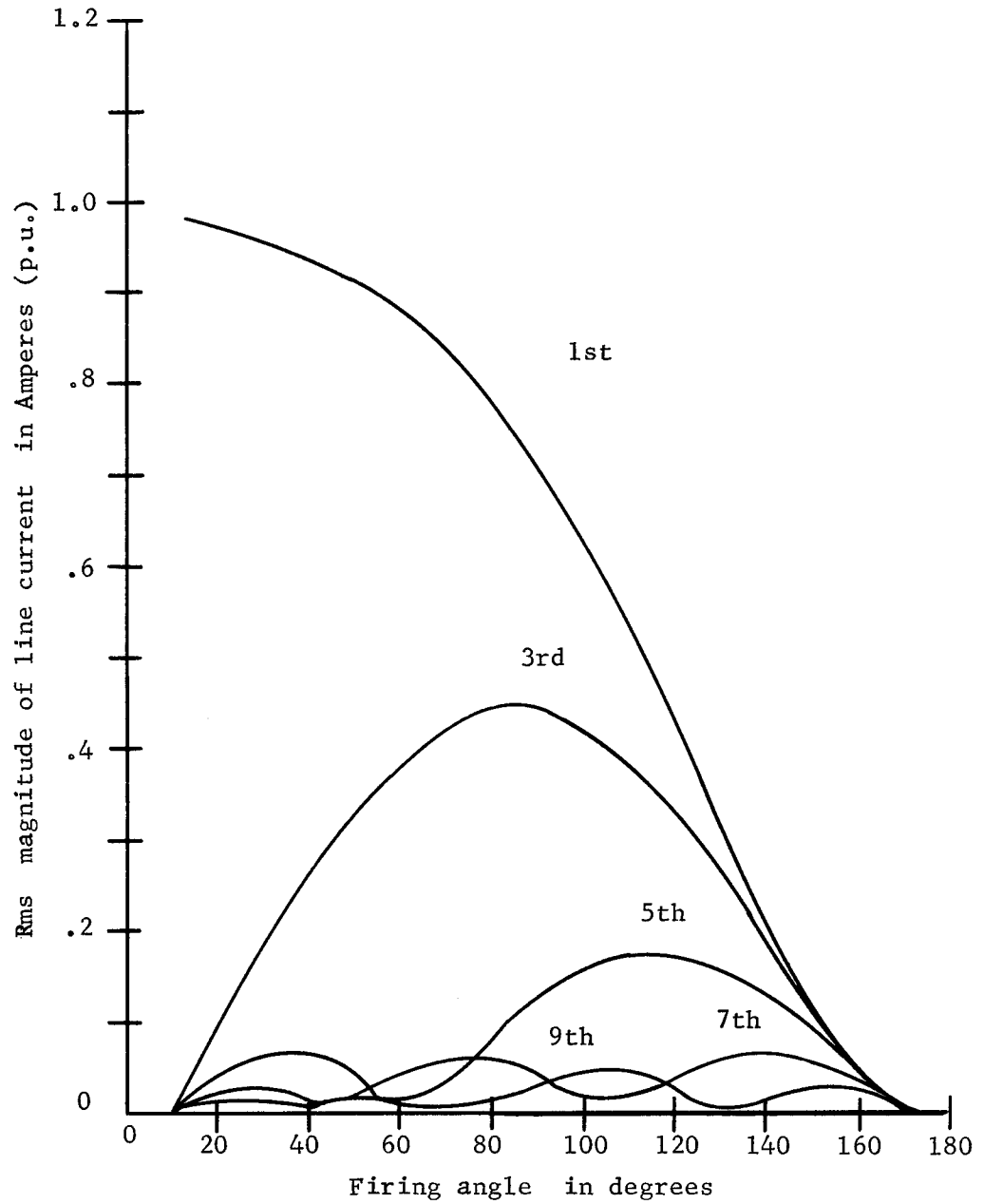
Fig. 46   Line current harmonics vs. firing angle
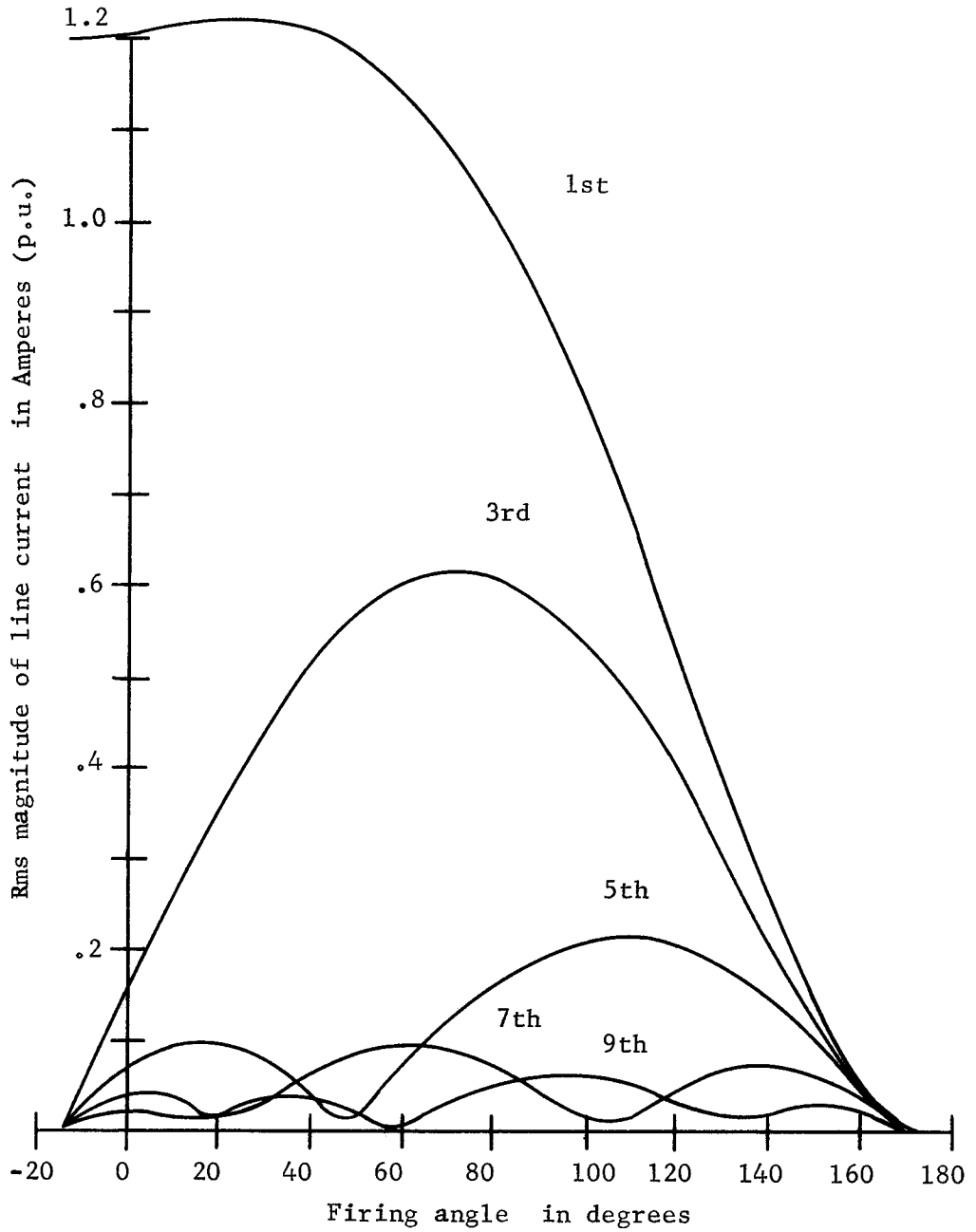for   Q = 2.0, X_L = .2   and   PF = 1.0

Fig. 47   Line current harmonics vs. firing angle
for Q = 2.0, X_L = .2 and PF = .9

Experimental Verification

The predicted results were verified for a number of load conditions. Figs. 48, 49 and 50 show calculated and experimental results for a stable load with $Q = 5$, $X_L = .2$ and $PF = -.9$, 1.0, .9 .

Fig.51 shows an unstable load condition and Fig.52 shows the jump phenomenon. Note the very good agreement of predicted and experimental values in Figs. 48 through 50. The inaccuracy in predicting the start of instability, as indicated in Fig. 51, is due to the fact that the value of the inductance in the experimental setup cannot be kept constant, as assumed in the calculation. In Fig.52, the jump phenomenon is verified. Very good accuracy was obtained on the return or increase side of the characteristic curve but on the decrease side there is a 22.6% difference between predicted and experimental values. It has been observed that in general better accuracies were obtained with higher Q loads.
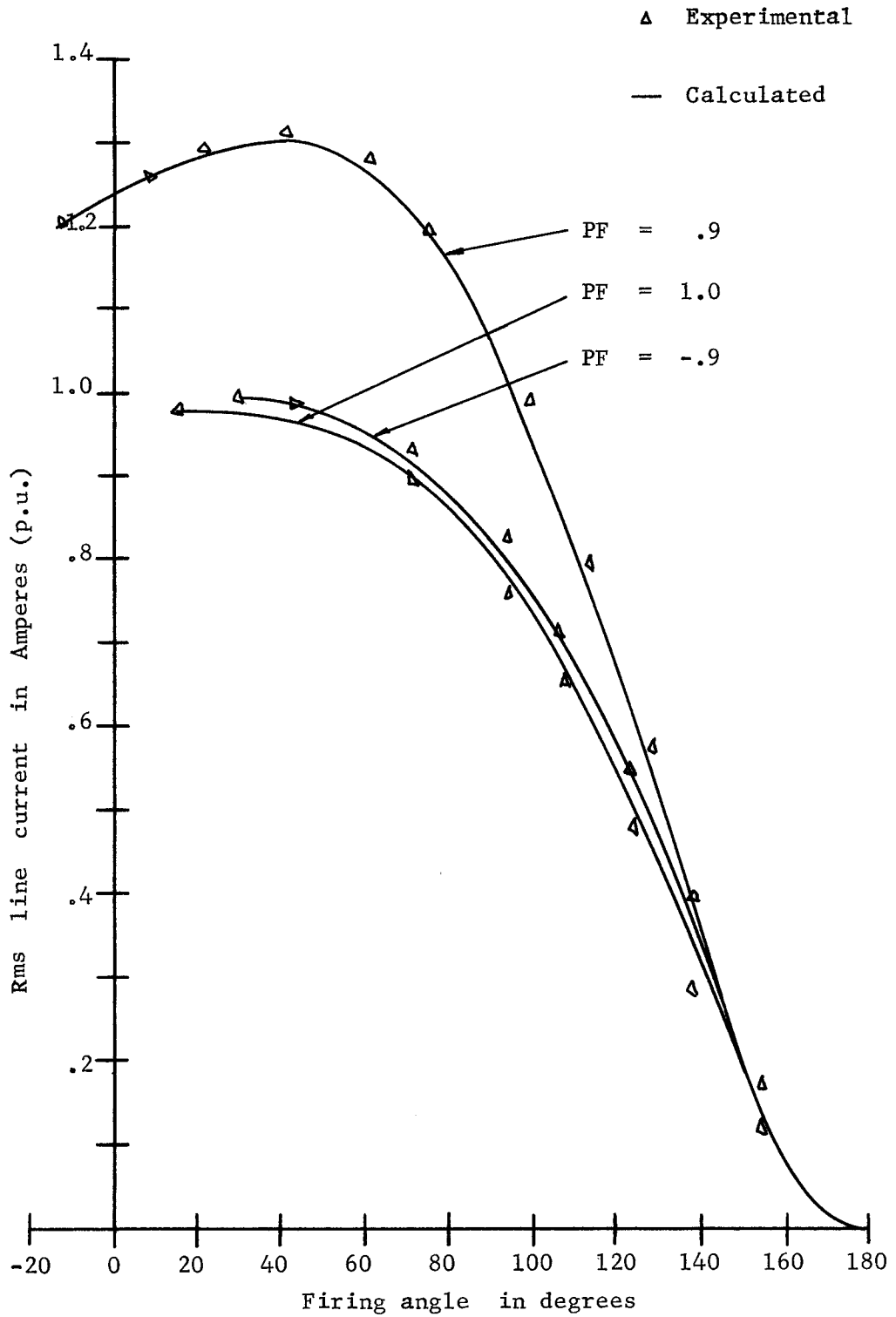
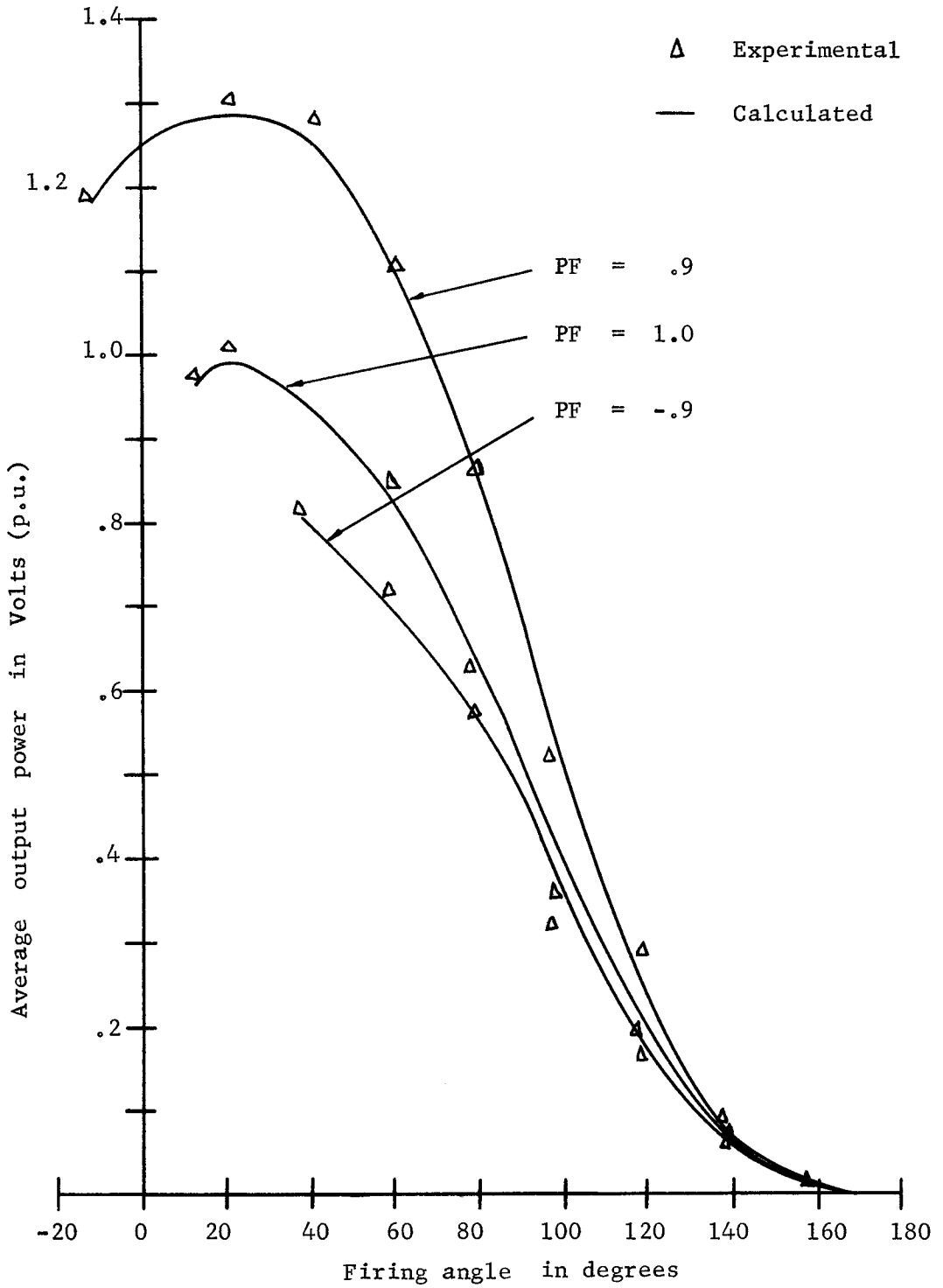Fig. 48   Rms line current vs. firing angle
for Q = 5.0   and X_L = .2

Fig. 49   Average output power vs. firing angle
for Q = 5.0 and X_L = .2
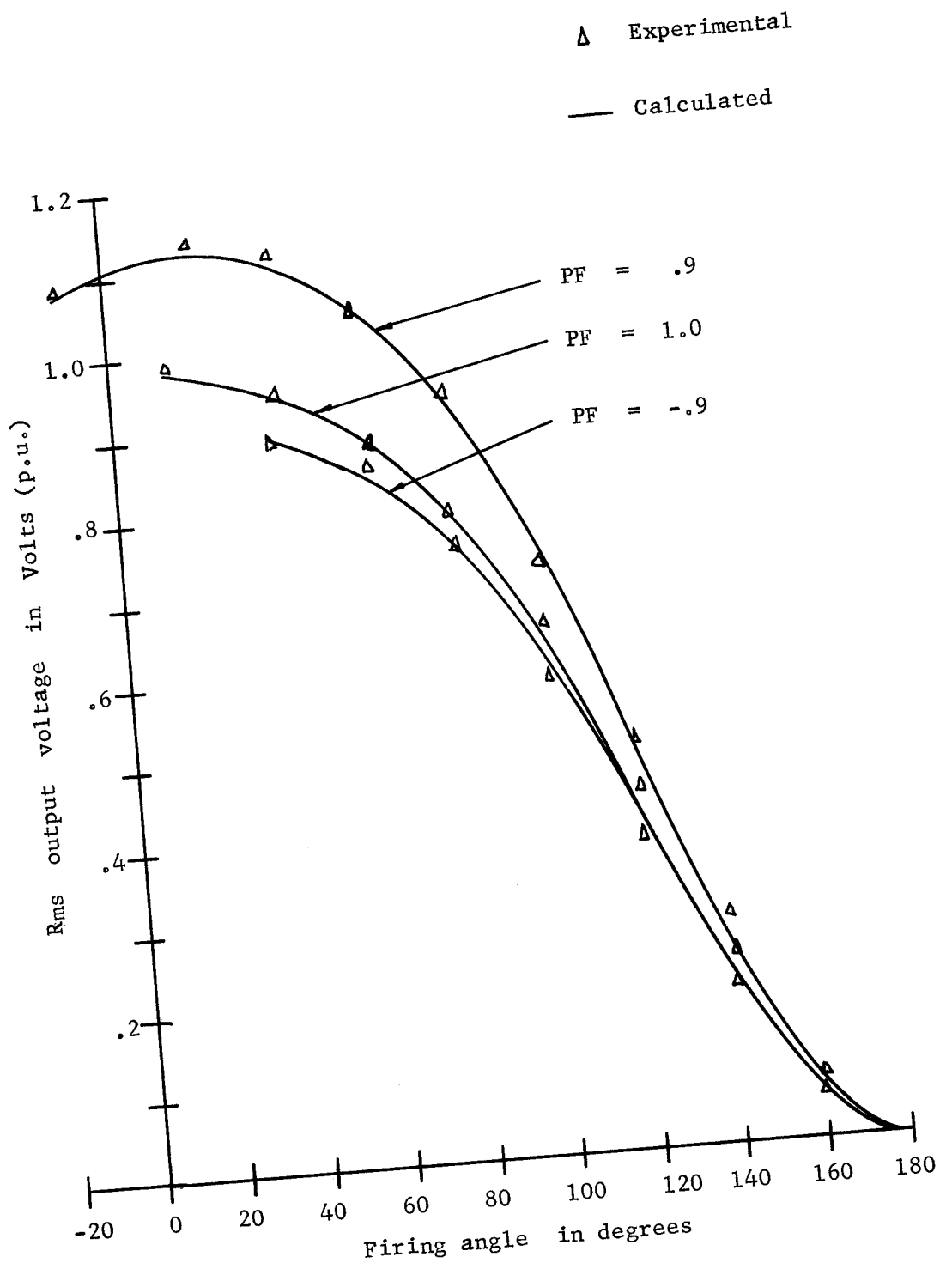
Fig. 50   Rms output voltage vs. firing angle
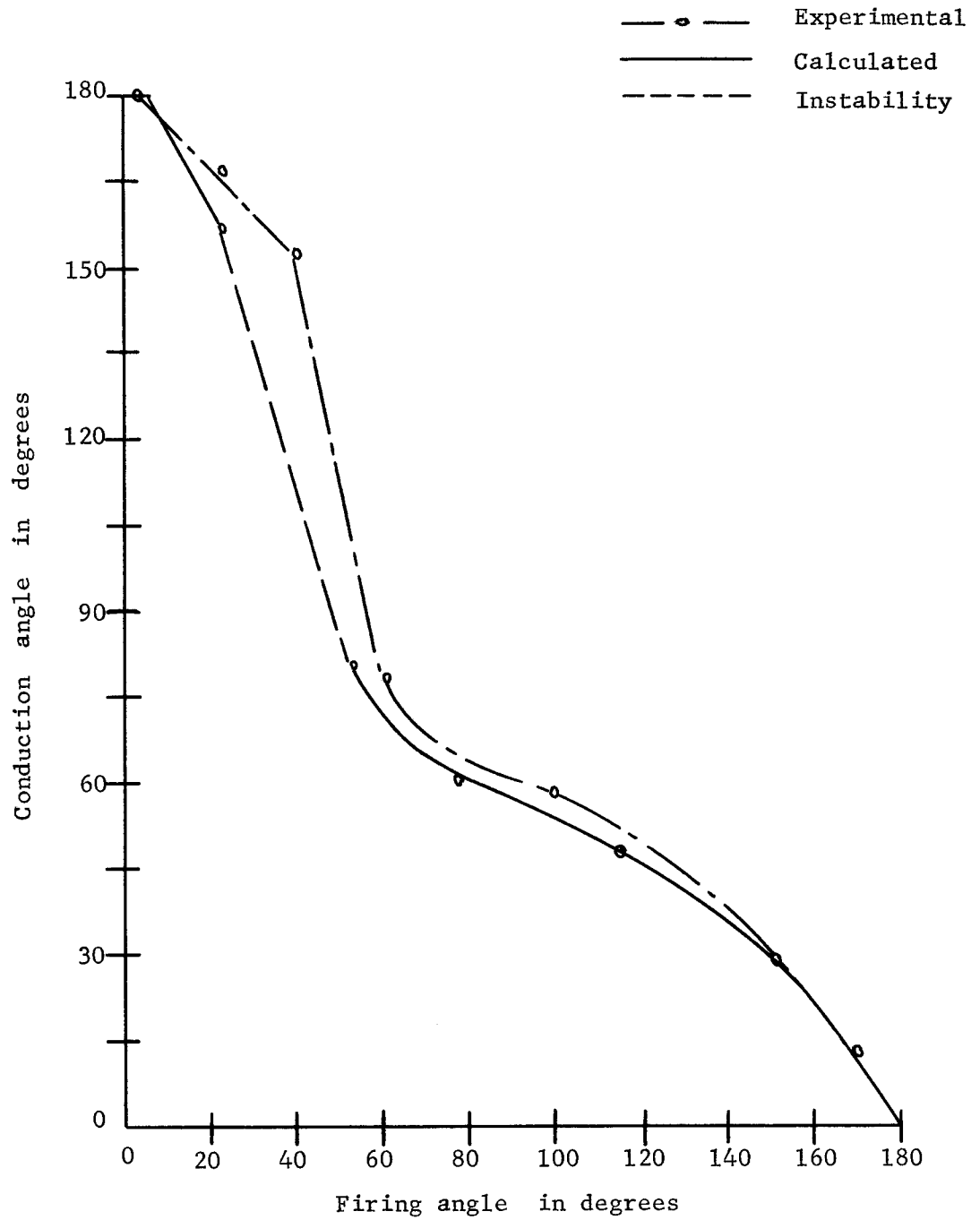for Q = 5.0 and X_L = .2

Fig. 51   Conduction angle vs. firing angle
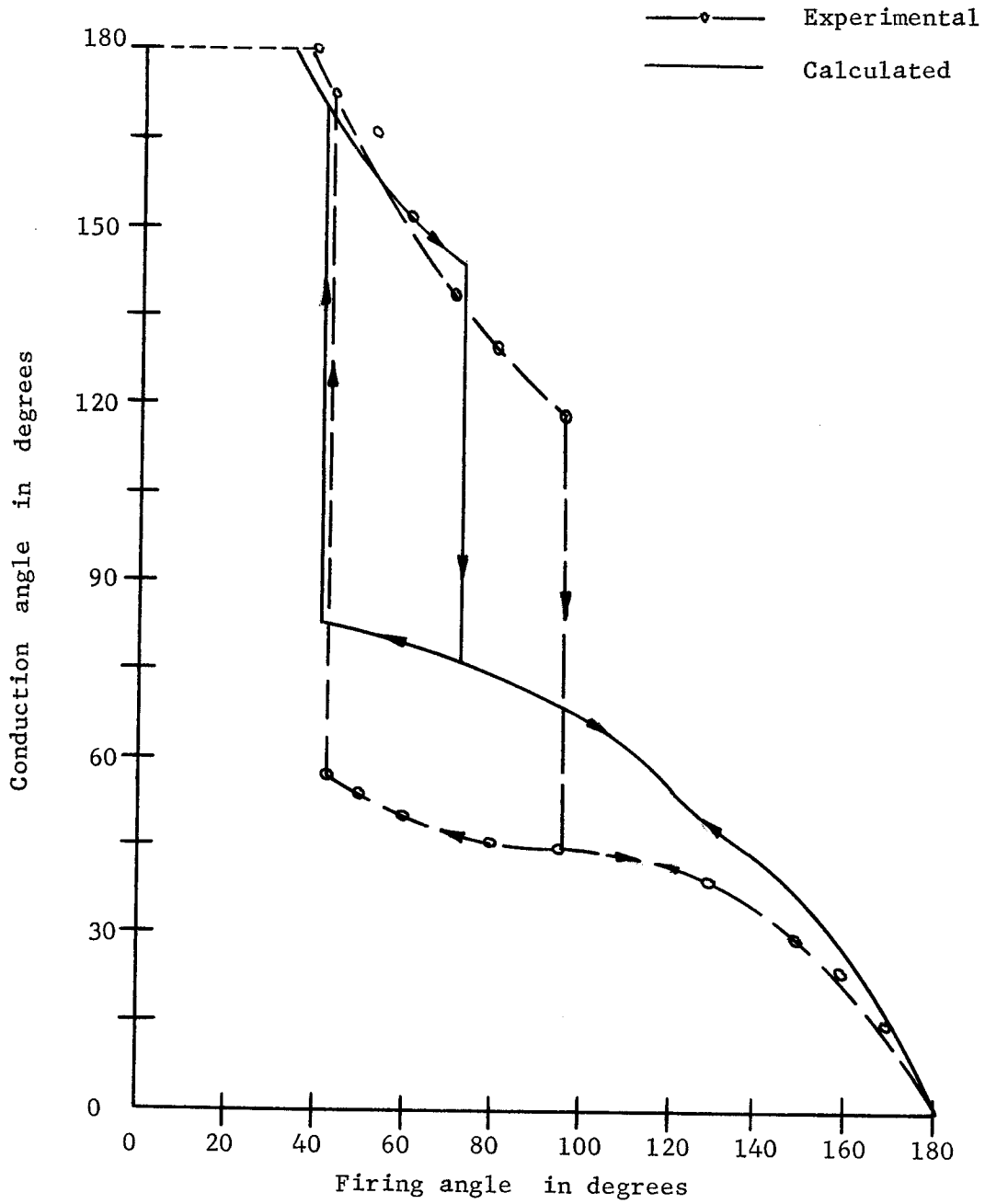for   Q = 1.0, X_L = .1   and PF = 1.0

Fig. 52   Conduction angle vs. firing angle
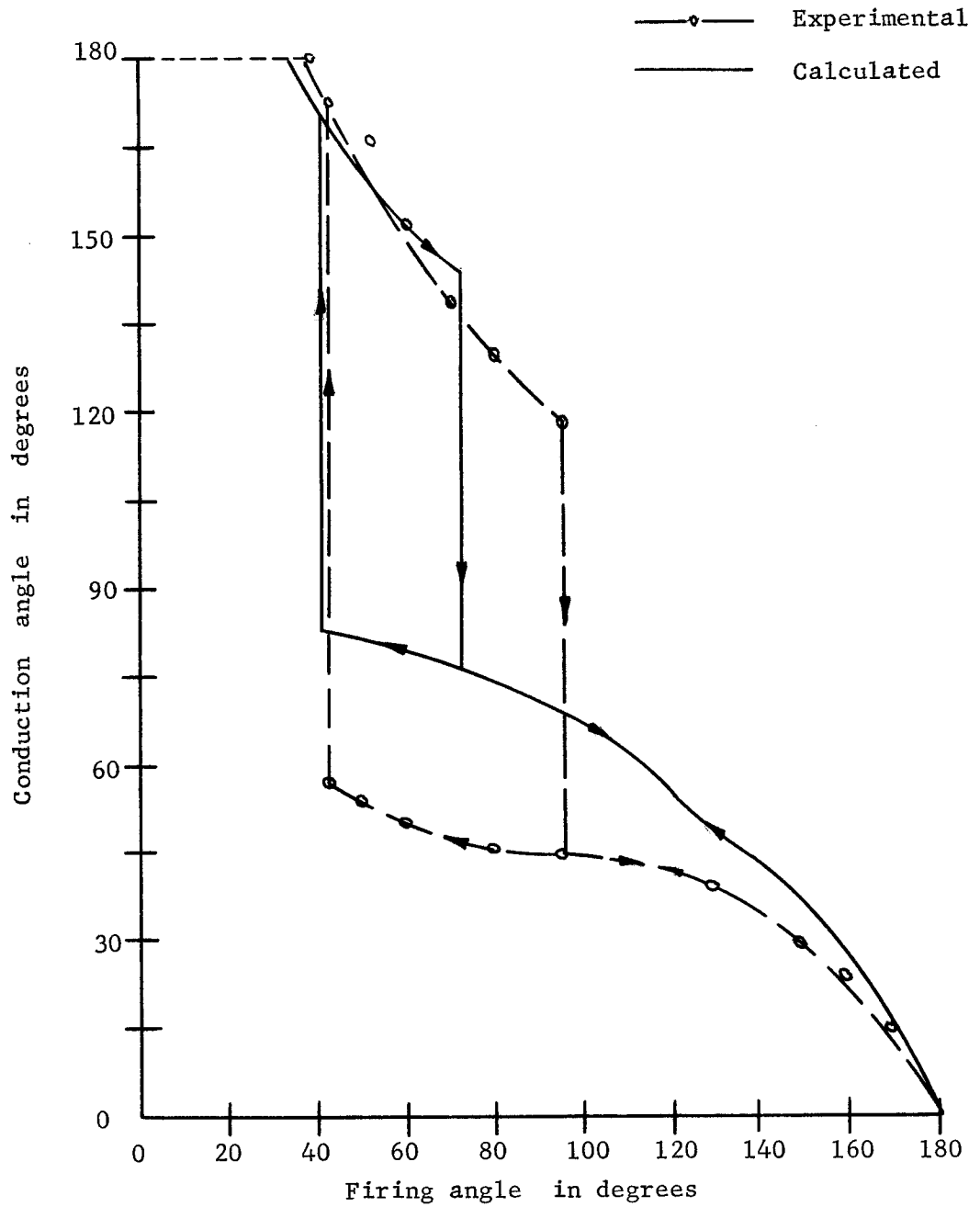for   Q = 1.0, X_L = .2 and PF = -.9

Fig. 52   Conduction angle vs. firing angle
for   Q = 1.0, X_L = .2 and PF = -.9

Comparison of Approximate
and Exact Theoretical Results

In developing the approximate analysis presented in Chapter III, two fundamental assumptions were made:

(a) The fundamental component of the line current i_L is the dominant component in predicting system performance.

(b) The fundamental component of the line current i_L decreases and becomes lagging with respect to the supply voltage as the firing angle ϕ is increased.

The accuracy of the system behavior predicted by the computer simulations has been demonstrated by Figs. 48 through 50. In Figs. 53 and 54, the average power and its fundamental component as a function of firing angle ϕ has been plotted for loads of $Q = 1$ and $Q = 10$, with PF = 1.0 and $X_L = .2$. Note that at $Q = 10$ the average power consists almost entirely of the fundamental component. That is, considering only the fundamental component of the average power would lead to negligible practical error.

Figs. 55 and 56 plot fundamental power as a function of firing angle ϕ as predicted by computer simulation. The close correspondence in both these figures is self-evident. The fundamental input power factor and the input KVA requirements can also be obtained easily from these curves.
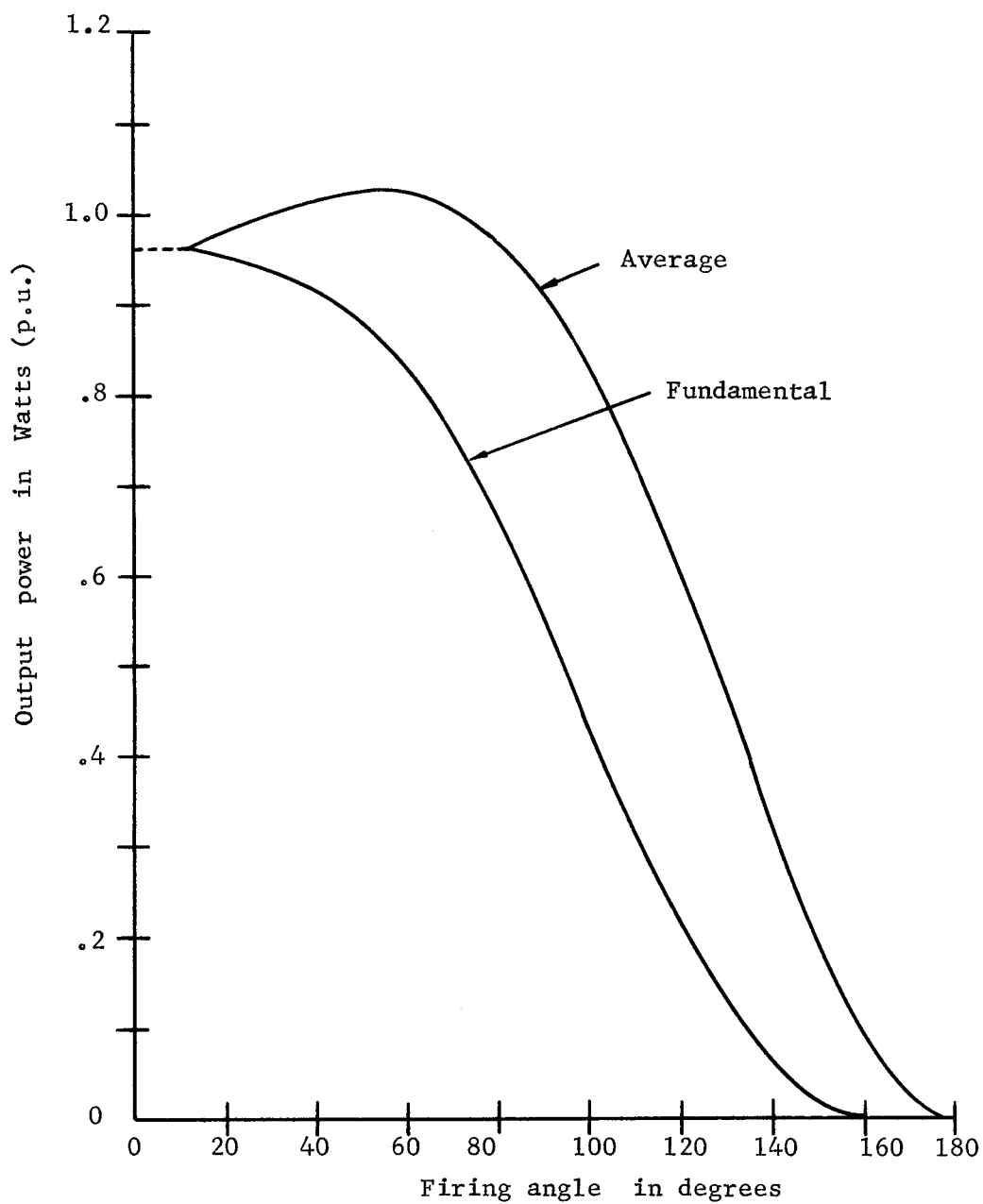
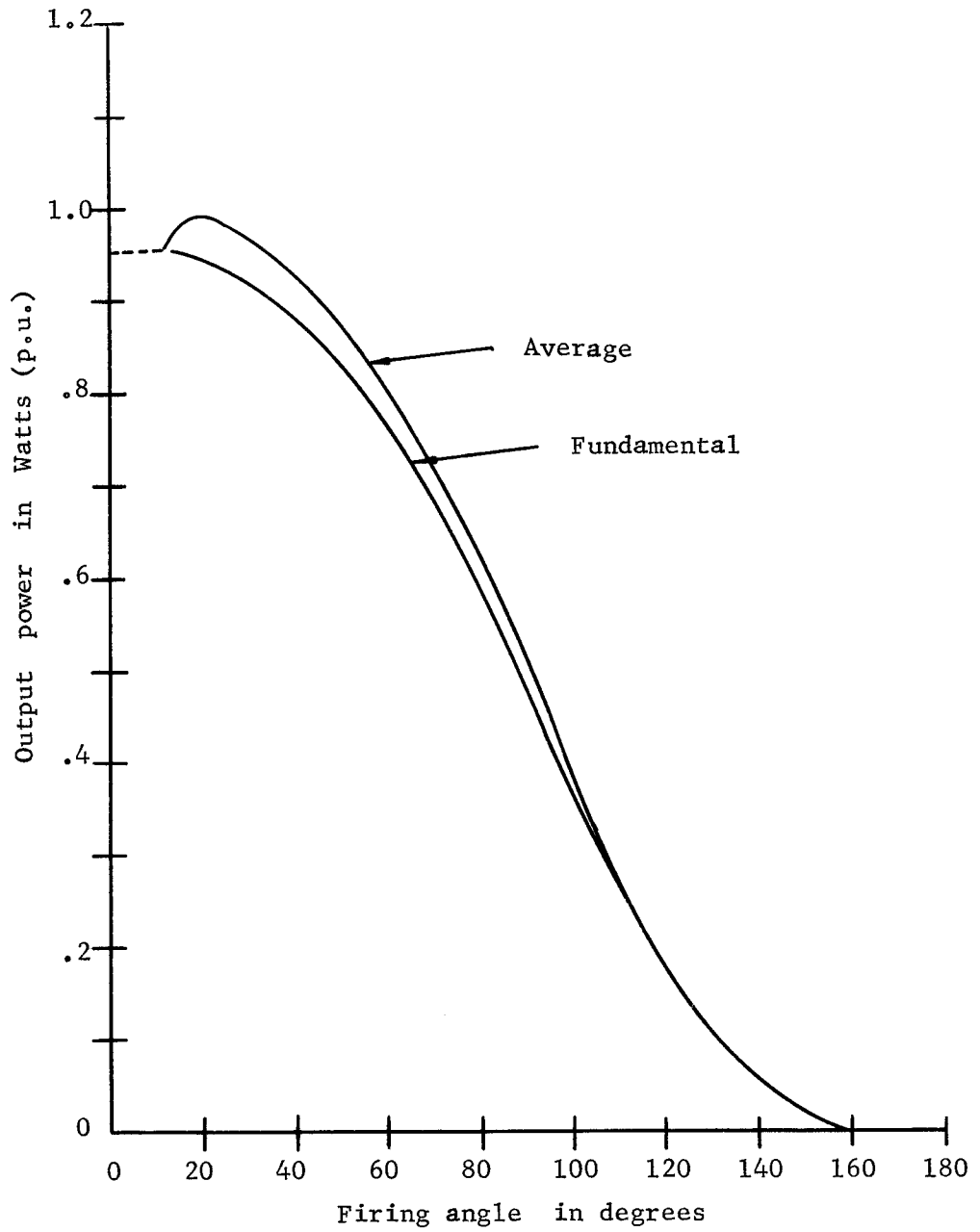Fig. 53 Output power vs. firing angle
for Q = 1.0, X_L = .2 and PF = 1.0

Fig. 54   Output power vs. firing angle
for Q = 10.0, X_L = .2 and PF = 1.0
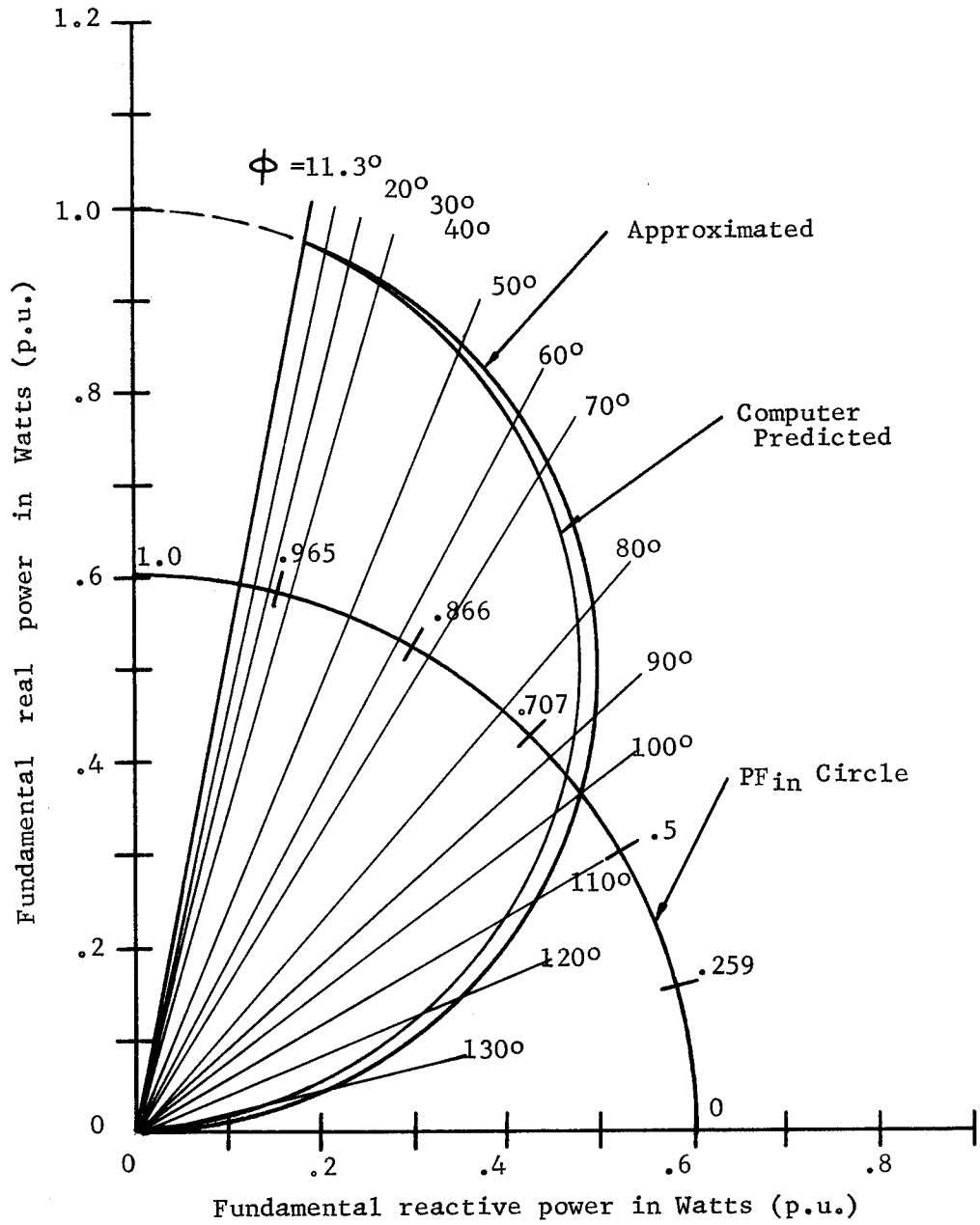
Fig.55 Real vs. reactive fundamental input power
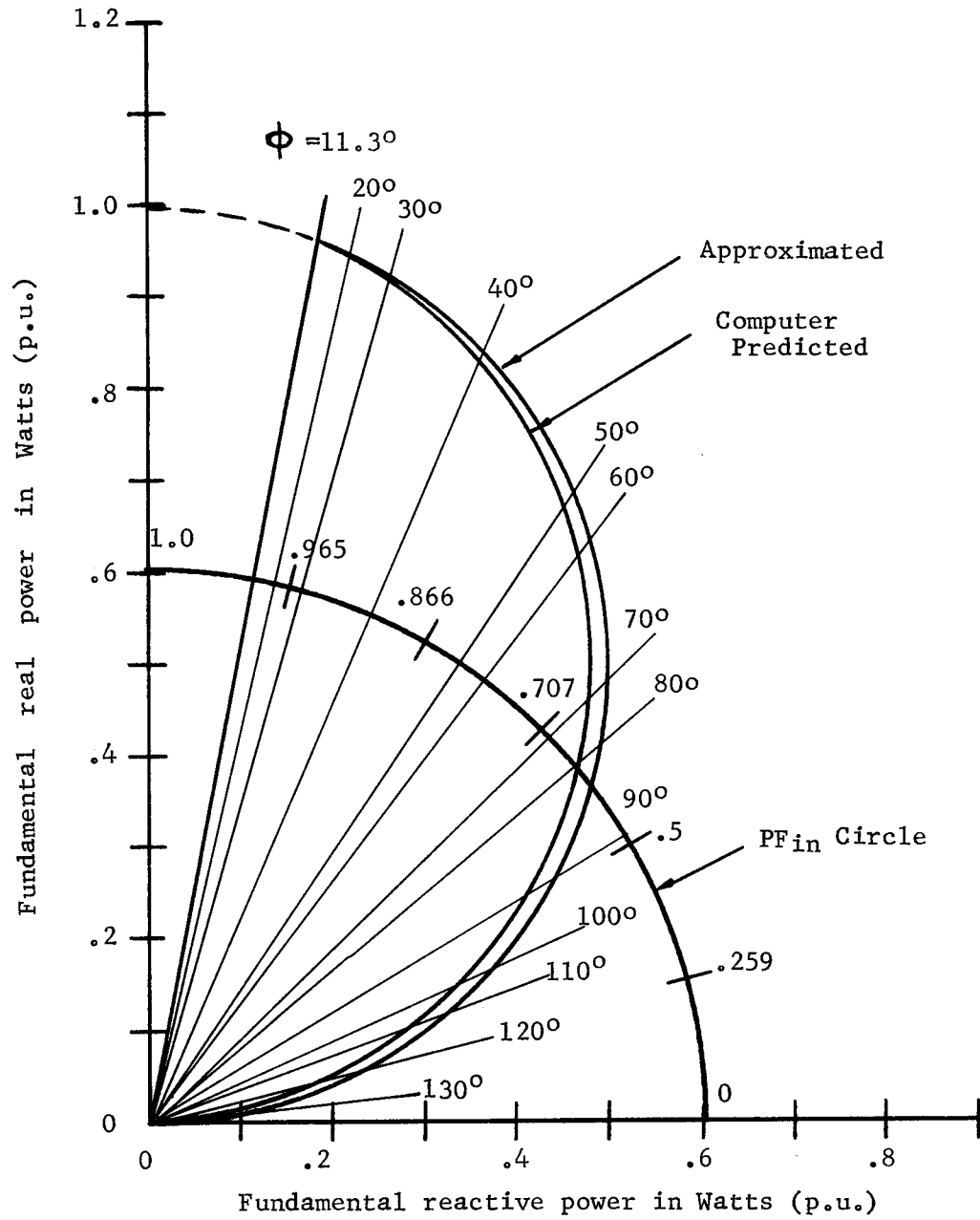for Q = 1.0, X_L = .2 and PF = 1.0

Fig. 56 Real vs. reactive fundamental input power
for Q = 10.0, X_L = .2 and PF = 1.0

Conclusions

In this chapter, an exact computer simulation of the controller has been developed. Stable and unstable operating conditions have been predicted and experimentally verified.

The following important observations were made:

1. The system is unstable for low Q's and low per-unit line reactance.

2. The system stability increases as the load Q and the per-unit line reactance is increased.

3. Loads with $Q \gtreqqless 2$ and $X_L \gtreqqless .2$ are stable within the investigated load power factor limits.

4. A jump phenomenon is present in this periodically interrupted circuit.

A short verification of the approximate method of analysis developed in Chapter III has also been given.

CHAPTER   V

CONCLUSIONS

The primary purpose of this thesis was to study the feasibility
and general behavior of the controller with an induction load.

An approximate and an exact method of system simulation were
developed. The system's behavior under various practical load condi-
tions was predicted and verified. System instabilities at low load Q's
and low values of per-unit line reactances and an interesting jump
phenomenon have also been predicted and verified. This phenomenon is
similar to that occurring in classical non-linear circuits with energy
storage elements. In this periodically interrupted circuit the anti-
parallel connected thyristor switches are the non-linear circuit
elements. They act as a harmonic generator similar to the way a
non-linearity acts in classical non-linear circuits.

From the design point of view, the system is stable and readily
controllable outside the indicated unstable region. The line harmonics
in the controlled region, with the third harmonic dominant, may be
objectionable from the power company's point of view.

For future investigations, various input filter configurations
could be considered to eliminate the harmonic currents from the supply
line. Also, an investigation with continuous gating may yield inter-
esting results. Some limited experimental work indicates the possibili-
ty of completely eliminating the instabilities.

REFERENCES

Books

Bedford, B.D. and Hoff, R.G. Principle of Inverter Circuits.
    New York: John Wiley and Sons, Inc., 1964.

Hoyt, W.H., Jr. and Kemmerley, J.E. Engineering Circuit Analysis.
    New York: McGraw-Hill Book Co., 1962.

Kuo, B.C. Linear Networks and Systems. New York: McGraw-Hill Book
    Co., 1967.

Lago, G.V. and Waidelich, D.L. Transients in Electric Circuits.
    New York: The Ronald Press Co., 1958.

Articles

Siman, Matthew. The Circle Diagram as a Teaching Tool. IEEE Trans-
    actions on Education, vol. E-11, No.1, March 1968, pp.50-56.